

SURFACE-BOUND NANOSTRUCTURES: MECHANICAL AND METROLOGICAL STUDIES

THÈSE N° 4042 (2008)

PRÉSENTÉE LE 4 AVRIL 2008

À LA FACULTÉ DES SCIENCES DE BASE

LABORATOIRE DE NANOSTRUCTURES ET NOUVEAUX MATÉRIAUX ÉLECTRONIQUES

PROGRAMME DOCTORAL EN PHYSIQUE

ÉCOLE POLYTECHNIQUE FÉDÉRALE DE LAUSANNE

POUR L'OBTENTION DU GRADE DE DOCTEUR ÈS SCIENCES

PAR

Kyumin LEE

B.Sc. in Physics, Seoul National University
et de nationalité sud-coréenne

acceptée sur proposition du jury:

Prof. G. Meylan, président du jury

Prof. L. Forro, directeur de thèse

Prof. H. Brune, rapporteur

Prof. O. Marti, rapporteur

Prof. E. Meyer, rapporteur



ÉCOLE POLYTECHNIQUE
FÉDÉRALE DE LAUSANNE

Suisse
2008

Surface-Bound Nanostructures: Mechanical and Metrological Studies

THÈSE N°4042 (2008)

PRÉSENTÉE LE 4 AVRIL 2008

À LA FACULTÉ SCIENCES DE BASE

LABORATOIRE DE NANOSTRUCTURES ET NOUVEAUX MATÉRIAUX
ÉLECTRONIQUES

PROGRAMME DOCTORAL EN PHYSIQUE

ÉCOLE POLYTECHNIQUE FÉDÉRALE DE LAUSANNE

POUR L'OBTENTION DU GRADE DE DOCTEUR ÈS SCIENCES

PAR

Kyumin Lee 이규민

B.Sc. in Physics, Seoul National University
et de nationalité sud-coréenne

acceptée sur proposition du jury:

Prof. G. Meylan, président du jury

Prof. L. Forro, directeur de thèse

Prof. H. Brune, rapporteur

Prof. O. Marti, rapporteur

Prof. E. Meyer, rapporteur



ÉCOLE POLYTECHNIQUE
FÉDÉRALE DE LAUSANNE

Lausanne, EPFL

2008

*To my wife Jisun Park
and our baby*

Version Abrégée

Cette thèse décrit l'étude des nanoparticules et des nanofilaments liés aux surfaces. Ce travail est motivé par l'importance de l'étude des propriétés mécaniques et métrologiques pour la fabrication de dispositifs électroniques à l'échelle nanométrique. Le microscope à force atomique (AFM) fut le principal instrument de caractérisation et de mesure.

Dans une première partie, l'évolution du module d'Young des nanotubes de carbone a été étudiée en fonction de leur diamètre externe. Celui-ci est directement proportionnel au diamètre de la particule de catalyseurs à partir de laquelle ils ont cru. Une technique efficace pour suspendre et positionner les nanotubes de carbone basée sur la dielectrophorèse a été développée. Aussi, la mesure de courbes de force par AFM a été mise en place pour l'étude de la rigidité des nanotubes de carbone. Les nanotubes de carbone ont été synthétisés dans des conditions identiques. Une dépendance importante du module d'Young des nanotubes de carbone par rapport à leur diamètre a été mise en évidence. Elle indique que de petites particules de catalyseur produisent une faible densité de défauts structuraux, alors que les particules larges produisent des tubes de moins bonne qualité. Les résultats expérimentaux de cette étude sont en accord avec le model de croissance à partir d'un catalyseur métastable pouvant être décrit comme une structure hybride d'une corps solide recouvert d'une couche liquide. Les cinétiques de croissance sont déterminées par l'épaisseur de cette couche, qui est plus stable pour de petites particules.

Dans une deuxième partie, des mesures précises de la taille de nanoparticules (dont leur propriétés catalytiques sont fortement tributaire) liées aux surfaces ont été effectuées à l'aide de l'AFM en mode dynamique. La taille mesurée est dépendante des paramètres de l'enregistrement de l'image. La modélisation théorique montre que les changements entre le mode non-contact et le mode contact intermittent induisent des différences reproductibles, comme le confirme les signaux expérimentaux de phase. Un décalage existe aussi entre les images stables de tout-non-contact et tout-contact-intermittent, et cette anomalie est expliquée par la déformation particule-substrat, et aussi par les forces capillaires. Les nanoparticules étaient déposées par l'ébullition de gouttes de solution colloïdale sur des surfaces préalablement chauffées, une nouvelle technique développée pour la dispersion uniforme de nanoparticules et de nanofilaments colloïdaux. Nos expériences suggèrent que le dépôt se fait par la récession lisse de microgouttes aux températures élevées. La méthode est applicable aux diverses surfaces et matériaux.

Enfin, une interface haptique pour l'AFM a été créée. Il est possible de mettre en oeuvre l'interface sur différents modèles de AFM avec peu d'effort. Le logiciel supporte le mode contact et aussi le mode dynamique. La manipulation des nanoparticules liées aux surfaces a été effectuée, et une stratégie pour les études tribologiques est proposée.

Mots de clé: nanostructures, nanotubes de carbone, nanoparticule métalliques, dépôt chimique en phase vapeur, microscope à force atomique, dynamique, contact intermittent, non-contact, dépôt par ébullition, haptique, nanomechanique, nanometrologie

Abstract

This thesis looks at *surface-bound* nanowires and nanoparticles, the mechanical and the metrological properties of which are of practical importance in the realization of nanometer-scale electronics. Atomic force microscope (AFM) was the main instrument of research.

By bending suspended carbon nanotube structures with the AFM, the Young's modulus of carbon nanotubes has been measured. An efficient new technique that involves an ac-dielectrophoresis preparation of carbon nanotubes on v-groove GaAs substrates and a force-curve measurement of the stiffness has been devised. The Young's modulus of a batch of multiwall carbon nanotubes grown by a single chemical vapor deposition (CVD) process shows a strong diameter dependence, indicating that the small catalyst particles produce crystalline tubes, while the thicker particles produce low-quality tubes with an abundance of structural defects. The experimental result is a strong evidence for the metastable-catalyst growth model of carbon nanotubes in CVD—the growth kinetics of carbon nanotubes is determined by the catalyst's liquid skin, which is more stable for smaller catalysts.

As the nanotube study highlighted the importance of the size of catalyst nanoparticles, the topic of accurate nanoparticle sizing by dynamic AFM was then investigated. The measured size of a surface-bound nanoparticle was found to vary with imaging parameters, and a theoretical modeling showed that the non-contact—intermittent-contact mode switching can lead to discrepancies. Experimental results confirmed that the mode switching indeed causes the largest error in size measurements. A discrepancy also exists between the all-non-contact-mode and all-intermittent-contact-mode cases, and this anomaly could be explained by the effects of particle–substrate deformation and capillary forces.

Nanoparticles were prepared on surfaces by boiling colloid drops on hot surfaces, a new technique developed for the uniformly dispersed deposition of colloidal nanoparticles and nanowires. Our experiments suggest that the actual deposition occurs through the smooth dewetting of liquid microdrops at elevated temperatures. The method is applicable on a wide range of surfaces and materials.

Finally, a general haptic interface for the AFM was realized. The interface can be implemented on different AFM models with little effort, and it supports both the contact- and dynamic-AFM operations. Manipulation of gold nanoparticles has been carried out by raster scanning at different dynamic AFM setpoints, a promising approach for

a quantitative study of the nanoparticle–substrate friction.

Keywords: nanomechanics, nanometrology, surface-bound nanostructures, carbon nanotubes, metal nanoparticles, chemical vapor deposition (CVD), dynamic, intermittent-contact (IC-AFM), tapping-mode, non-contact (NC-AFM), atomic force microscopy (AFM), haptic interface, nanomanipulation, boil deposition

Contents

List of Figures	xiii
List of Tables	xvii
List of Abbreviations	xix
List of Symbols	xxi
1 Introduction	1
2 Atomic Force Microscopy	5
2.1 Stylus Profilometer	5
2.2 Micro-fabricated Tip and Cantilever	6
2.2.1 Dynamic Calibration Methods	7
2.2.2 Reference Devices	7
2.3 Piezo-Driven Positioning Stages	7
2.3.1 Tube Scanners	7
2.3.2 Flexure-Guided Scanners	8
2.4 Data Presentation	9
2.5 Contact AFM	10
2.6 Force Curves	11
2.7 Contact AFM Force Sensitivity	13
2.8 Dynamic AFM	16
2.8.1 Non-Contact AFM	16
2.8.2 Intermittent-Contact AFM	18
2.8.3 Bistability of Oscillating Cantilever	18
2.8.4 Dynamic AFM Sensitivity	20
2.9 AFM Modifications	20
3 Preparation of Surface-Bound Nanostructures	21
3.1 Synthesis of Nanoparticles	21
3.1.1 Thin-Film Deposition	21
3.1.2 Spray Pyrolysis	21
3.1.3 Chemical Synthesis	22
3.2 Synthesis of Nanowires	23

3.2.1	High-Energy Synthesis	23
3.2.2	Vapor-Phase Synthesis Using Catalysts	23
3.2.3	Solution-Phase Synthesis	25
3.3	Conventional Methods for Dispersed Deposition	26
3.3.1	Depositing Nanoparticles	27
3.3.2	Depositing Nanowires	28
3.4	Boil Deposition	29
3.4.1	Experiment	29
3.4.2	Results	31
3.4.3	Discussion	34
3.5	Conclusions and Outlook	36
4	Mechanical Properties of Surface-Bound Nanowires	37
4.1	Carbon Nanotube Applications in Microelectronics	37
4.1.1	Recent Trends in Silicon Technology	37
4.1.2	Carbon Nanotube Interconnects	39
4.1.3	Carbon Nanotube Transistors	39
4.1.4	Mechanical Stresses in IC Fabrication and Operation	40
4.2	Measuring the Elastic Modulus of a Carbon Nanotube	42
4.2.1	Electron Microscopy Methods	42
4.2.2	Atomic Force Microscopy Methods	45
4.3	Previously Reported Mechanical Properties of Carbon Nanotubes	51
4.3.1	Exceptionally High Elastic Modulus of Arc-Discharge-Grown Carbon Nanotubes	51
4.3.2	Low Bending Modulus of Carbon Nanotube Bundles	51
4.3.3	Low Elastic Modulus of CVD-Grown Carbon Nanotubes	53
4.4	Diameter-Dependent Elastic Modulus of CVD-Grown Carbon Nanotubes	54
4.4.1	Experiment	54
4.4.2	Results and Discussion	55
4.5	Metastable-Catalyst Model of Carbon Nanotube Growth	60
4.5.1	Vapor–Liquid–Solid Model	60
4.5.2	Nanoparticle Melting Point Depression Effect	61
4.5.3	Partially Liquid Catalyst—Solid Core, Liquid Skin	62
4.5.4	Size-Dependent Structural Quality of Carbon Nanotubes	63
4.6	Conclusions and Outlook	65
5	Metrological Properties of Surface-Bound Nanoparticles	67
5.1	Size-Dependent Properties of Nanoparticles	67
5.1.1	Catalytic Properties	67
5.1.2	Optical Properties	67
5.2	Anomalies in Size Measurement by Dynamic AFM	69

5.2.1	Amplitude-Modulation AFM	70
5.2.2	Experiment	70
5.2.3	Dependence on the Initial Amplitude	71
5.2.4	Dependence on the Setpoint Amplitude	72
5.3	Experimental Amplitude–Phase–Distance (APD) Curves	74
5.3.1	Why are APD Curves Important?	74
5.3.2	Instrumentation	75
5.3.3	Results	76
5.4	Dynamic AFM Simulation	77
5.4.1	Mass–Spring Model	77
5.4.2	van der Waals Force	80
5.4.3	Contact Force and Adhesion Force	81
5.4.4	Algorithm and Software	81
5.4.5	Non-Contact Versus Intermittent Contact	83
5.5	Anomalies Explained	85
5.5.1	Height Measurement Error due to Mode Switching	85
5.5.2	Particle–Substrate Deformation	86
5.5.3	Capillary Force	89
5.6	Comparison with Other Reported Works	91
5.7	Conclusions and Outlook	93
6	Haptic Interface for the AFM and Nanomanipulation	95
6.1	Haptic Interface	95
6.1.1	Reported Works	95
6.1.2	Model-Independent Haptic Interface	97
6.2	Nanomanipulation	99
6.2.1	via Haptic Interface	99
6.2.2	via Programmable Interface	99
6.3	Conclusions and Outlook	102
7	General Conclusions	103
7.1	Carbon Nanotubes	103
7.2	Nanoparticle Metrology	103
7.3	Nanomanipulation and Nanotribology	104
7.4	Boil Deposition	104
A	Scanner Positioning Errors and Solutions	105
	Acknowledgments	123
	Curriculum Vitae	125

Contents

List of Figures

1.1	Consumer products claiming to be “nano”	1
1.2	Nanotube and nanoparticle transistors	2
2.1	Stylus profilometer	5
2.2	Cantilever and tip	6
2.3	Cantilever types	6
2.4	Scanning system designs	8
2.5	Flexure-guided scanners	8
2.6	Data presentation	9
2.7	Contact AFM	10
2.8	Force curve techniques	12
2.9	Cell–cell adhesion studied with force curves	12
2.10	Geometry of AFM optical lever	13
2.11	Non-contact AFM	16
2.12	Intermittent-contact versus non-contact AFM	19
3.1	Gold nanoparticle synthesis	22
3.2	Carbon nanotube synthesis by CVD	24
3.3	Multiwall carbon nanotubes	24
3.4	Aggregation in a drying colloid drop	26
3.5	Self-assembly and micelle-monolayer deposition techniques	27
3.6	AC dielectrophoresis of nanowires	28
3.7	Direct and indirect boil deposition	30
3.8	Boil-deposited nanoparticles	32
3.9	Boil-deposited nanowires	33
3.10	ZnO nanowires grown from boil-deposited gold nanoparticles	34
3.11	Microdrop deposits at different temperatures	35
3.12	Ink-jet lithography combined with boil deposition	36
4.1	Single-wall carbon nanotube	38
4.2	Metal-on-oxide field-effect transistor (MOSFET)	38
4.3	Carbon nanotube interconnects	40
4.4	Chemical–mechanical polishing (CMP)	41

List of Figures

4.5	Electron microscopy methods for mechanical measurements on carbon nanotubes	43
4.6	Lateral deflection measurement of carbon nanotubes	45
4.7	Normal deflection measurement of nanotube elastic modulus	46
4.8	Swiss-cheese method of measuring nanotube elastic modulus	47
4.9	Lithography process for preparing suspended nanotubes	48
4.10	Substrate preparation for ac electrophoresis	49
4.11	AC electrophoresis of carbon nanotubes for force curve analysis	49
4.12	Force curve analysis of suspended nanotubes	50
4.13	Bending of a bundled structure	51
4.14	Definition of Young’s and shear moduli	52
4.15	Bending modulus of nanotube bundles	53
4.16	Effect of thermal annealing on CVD-grown multiwall carbon nanotubes	54
4.17	Diameter-dependent elastic modulus of CVD-grown multiwall carbon nanotubes	56
4.18	$1/E_{tube}$ versus D^2/L_{tube}^2	57
4.19	Intratube stick-slip	59
4.20	Carbon nanotube synthesis	61
4.21	Calorimetry of nanoparticles	61
4.22	Multiwall carbon nanotube growth from solid core–liquid skin catalyst .	63
4.23	Influence of the catalyst shape on the nanotube quality	64
4.24	Dependence of the nanotube quality on the catalyst size	64
5.1	Different nanowires grown with gold nanoparticle catalysts	68
5.2	Surface plasmon of nanoparticles	68
5.3	Amplitude-modulation AFM (AM-AFM)	69
5.4	Nanoparticle samples used for the dynamic AFM study	70
5.5	Measuring the nanoparticle height	71
5.6	Height measurement anomalies of a Si-wafer-bound gold nanoparticle . .	72
5.7	Height measurement anomalies of a stainless-steel-bound gold nanoparticle	73
5.8	Height measurement anomalies of a GaAs-wafer-bound gold nanoparticle	73
5.9	Principles of nanoparticle height measurement by AFM	74
5.10	Custom instrumentation for amplitude–phase–distance (APD) curve acquisition	75
5.11	“AmplitudeCurve” software user interface	76
5.12	Sample APD curves	77
5.13	APD curves on different particle–substrate systems	78
5.14	The mass–spring model of the dynamic-AFM tip–sample system	79
5.15	Different tip–sample models for the van der Waals interaction	80
5.16	“Dynamic AFM Simulator” software	83

5.17 Simulated NC-AFM and IC-AFM oscillation cycles	84
5.18 Simulated APD curves	85
5.19 Height anomalies due to mode switching	86
5.20 Gold nanoparticle height anomalies on silicon wafer due to mode switching	87
5.21 Gold nanoparticle height anomalies on steel substrate due to mode switch- ing	87
5.22 Gold nanoparticle height anomalies on GaAs substrate due to mode switching	88
5.23 Mismatching IC-AFM branches on the substrate and the particle	88
5.24 Height measurement error due to the particle-substrate contact defor- mation	89
5.25 Model of the capillary force	90
5.26 Amplitude-distance curves simulated with the capillary force included .	91
5.27 Height distribution of CdSe nanocrystals on different surfaces	92
5.28 Height measurement anomalies of WO ₃ nanoparticle	92
5.29 Height measurement anomalies of mica-bound gold nanoparticles	93
6.1 General outline of a haptic interface for the AFM	96
6.2 The STM and AFM nanoManipulator systems from University of North Carolina	96
6.3 Schematic of AFM haptic interfaces at EPFL	98
6.4 Nanomanipulation via haptic interface	99
6.5 Nanomanipulation via programmable interface	100
6.6 Nanomanipulation of silicon-wafer-bound gold nanoparticles	101
6.7 Raster-scan-induced asymmetry of tip-particle work	101
A.1 Hysteresis and creep of piezoelectric actuators	106
A.2 Image distortion due to x-y scanner nonlinearity and hysteresis	106
A.3 Height measurement errors due to piezoelectric creep	107
A.4 Artifacts due to hysteresis and creep	107

List of Figures

List of Tables

2.1	Force resolution of commercial AFM cantilevers	15
3.1	Heater temperatures for different substrates and colloids.	31

List of Tables

List of Abbreviations

1D	One-Dimensional
2D	Two-Dimensional
3D	Three-Dimensional
AES	Auger Electron Spectroscopy
AFM	Atomic Force Microscopy or Atomic Force Microscope
AM-AFM	Amplitude-Modulation AFM
APD	Amplitude-Phase-Distance
CMOS	Complementary Metal-Oxide-Semiconductor
CMP	Chemical-Mechanical Polishing
CNT	Carbon NanoTube
CVD	Chemical Vapor Deposition
DMA	Differential Mobility Analyzer
DMT	Derjaguin-Müller-Toporov
EFM	Electrostatic Force Microscopy
EDM	Electrical Discharge Machining
EDX	Energy-Dispersive X-ray spectroscopy
FET	Field-Effect Transistor
FFM	Friction Force Microscopy
FM-AFM	Frequency-Modulation AFM
IC	Integrated Circuit
IC-AFM	Intermittent-Contact AFM
ILD	InterLayer Dielectric
LFM	Lateral Force Microscopy
MEMS	MicroElectroMechanical Systems
MFM	Magnetic Force Microscopy
MOSFET	Metal-Oxide-Semiconductor Field-Effect Transistor
MWCNT	MultiWall Carbon Nanotube
NC-AFM	Non-Contact AFM
PC	Personal Computer
PMD	Poly-Metal Dielectric
RC	Resistance \times Capacitance
SCE	Short Channel Effect
SDS	Sodium Dodecyl Sulfate

List of Abbreviations

SEM	Scanning Electron Microscopy or Scanning Electron Microscope
SOG	Spin-On Glass
SPM	Scanning Probe Microscopy or Scanning Probe Microscope
STM	Scanning Tunneling Microscopy
SWCNT	Single-Wall Carbon Nanotube
TEM	Transmission Electron Microscopy or Transmission Electron Microscope
VLS	Vapor–Liquid–Solid
VLSI	Very-Large-Scale Integration

List of Symbols

k_B	Boltzmann constant
RH	Relative humidity
T	Temperature
t	Time
α	Cantilever mounting angle with respect to the x-y (sample) plane
b	Cantilever thickness
I_k	Second moment of inertia of cantilever
L	Cantilever length
W	Cantilever width
β	Tip cone half-angle
δ_k	Tip-sample contact deformation
ν_t	Tip Poisson ratio
ν_s	Sample Poisson ratio
a_o	Equilibrium tip-sample interatomic spacing
E_k	Cantilever elastic modulus
E_t	Tip elastic modulus
E_s	Sample elastic modulus
H	Tip-sample Hamaker constant
K	Reduced tip-sample modulus
R	Reduced tip-sample radius
R_t	Tip radius
R_s	Sample radius
W	Work of adhesion
θ	Change in cantilever free-end angle corresponding to deflection z
ϕ	Phase difference between the cantilever driving and oscillation signals
τ	Normalized time of cantilever oscillation ($= f t$)
ω	Cantilever angular driving frequency
ω_o	Cantilever angular natural frequency
ω_R	Cantilever angular resonance frequency
A	Cantilever oscillation amplitude

List of Symbols

A_o	Cantilever free (initial) amplitude at zero tip-sample interaction
A_{set}	Setpoint amplitude for the AM-AFM operation
f	Cantilever driving (operation) frequency
f_o	Cantilever natural (fundamental) frequency
f_R	Cantilever resonance frequency
k	Cantilever spring constant
m^*	Cantilever effective mass
Q	Cantilever oscillation quality factor
s	Tip-sample separation. $s = z_c + z$
T_{osc}	Cantilever oscillation period
$V_d(t)$	Sinusoidal voltage signal driving the dither piezo for cantilever oscillation
V_o	Amplitude of $V_d(t)$
z	Cantilever deflection. Positive for upward deflection (away from the sample) and negative for downward deflection (towards the sample)
z_c	Tip-sample rest separation at zero oscillation amplitude
Z	Z scanner displacement
F_k	Force on the cantilever causing static deflection z
F_{ts}	Total tip-sample interaction force
F_{ct}	Tip-sample contact force
F_{ad}	Tip-sample adhesion force
F_{vdW}	Van der Waals force
F_{el}	Electrostatic force
F_{cap}	Capillary force
F_{chem}	Chemical force
$F_d(t)$	Sinusoidal cantilever driving force
F_o	Amplitude of $F_d(t)$
δF	Minimum resolvable force
$\delta\theta$	Angular resolution of the optical lever in an AFM
B	Bandwidth of AFM optical lever detection system
E_{gap}	Bandgap energy
γ_o	Carbon-to-carbon tight-binding overlap energy
a_{CC}	Nearest-neighbor carbon-to-carbon distance
D	Nanotube outer diameter
D_i	Nanotube inner diameter
E_{tube}	Bending modulus of a nanotube
A_{tube}	Cross-sectional area of a nanotube

L_{tube}	Suspended length of a suspended or cantilevered nanotube
I_{tube}	Second moment of inertia of a nanotube
W_n	Vibration energy of the n-th resonance mode for a cantilever beam
ω_n	Angular frequency of the n-th mode resonance
u_n	Instantaneous tip deflection of a cantilever beam due to the n-th mode resonance
c_n	Effective spring constant of a cantilever beam in the n-th mode resonance
β_n	N-th solution to $\cos \beta \cosh \beta = -1$
δ_{tube}	Deflection of a suspended nanotube
k_{tube}	Spring constant of a suspended nanotube
k_{eff}	Effective spring constant of a AFM cantilever–nanotube system
E_Y	Young’s modulus
G	Shear modulus
ν	Poisson ratio
f_s	Nanotube shape factor
T_m^{bulk}	Bulk melting point
T_m^{NP}	Nanoparticle melting point
V_M	Molar volume of a solid
γ^{SL}	Solid–liquid surface tension
ΔH_m	Melting molar enthalpy of a solid
D_{NP}	Nanoparticle diameter
	Nanoparticle height measured with
H_A	NC-AFM on both the particle and the substrate
H_B	NC-AFM on the particle and IC-AFM on the substrate
H_C	IC-AFM on the particle and NC-AFM on the substrate
H_D	IC-AFM on both the particle and the substrate
γ^{water}	Surface energy of water
h_t	Water layer thickness on the tip
h_s	Water layer thickness on the sample
s_{on}	Tip–sample separation at which water meniscus forms
s_{off}	Tip–sample separation at which water meniscus breaks
V_{men}	Volume of water meniscus

List of Symbols

1 Introduction

Nano is everywhere. From MP3 players to washing machines (Fig. 1.1), “nano” has become a household term. The overuse—and quite often *misuse*—of the prefix by the general public makes us wonder if “nanotechnology” and “nanoscience” are passing fashions, and if so, how long the waves will last. A friend of the author, while being interviewed for a faculty position, was asked “what do you see yourself doing in 5 years, after the ‘nano’ bubble pops?”

Even though most of the current “nano hype” is indeed based on little substance, the popularity of nanotechnology nonetheless represents the widespread acceptance that scientific and technological advances transform the society, and perhaps more importantly, that a science-derived technology can make money. One should remember that this now-common “invest-in-science-now-and-collect-money-later” business model is quite new. No one in the days of Heisenberg and Schrödinger would have guessed that the richest man in the world some half a century later would be the founder of a *software* company. Recalling the successes of condensed matter physics and microtechnology in creating the multi-billion-dollar semiconductor, display, computer and internet industries, we realize that nanotechnology has a high expectation to live up to.

For a physicist, the nanometer scale is interesting because many physical phenomena at this scale were off limits until the recent inventions and advances of electron

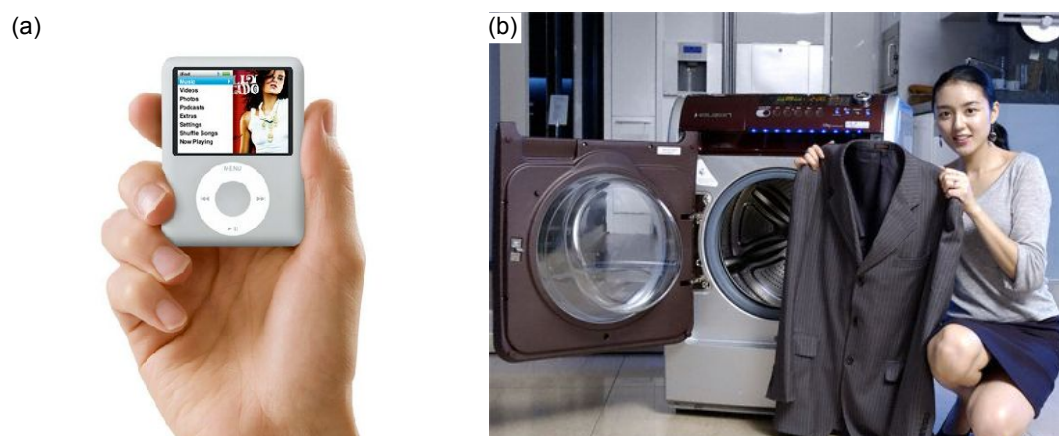


Figure 1.1: (a) Apple’s iPod nano MP3 player. (b) Samsung claims that its washing machines with incorporated “Silver Nano Technology” can kill 99.999% of bacteria (compared to 99.9% already possible with conventional washers).

1 Introduction

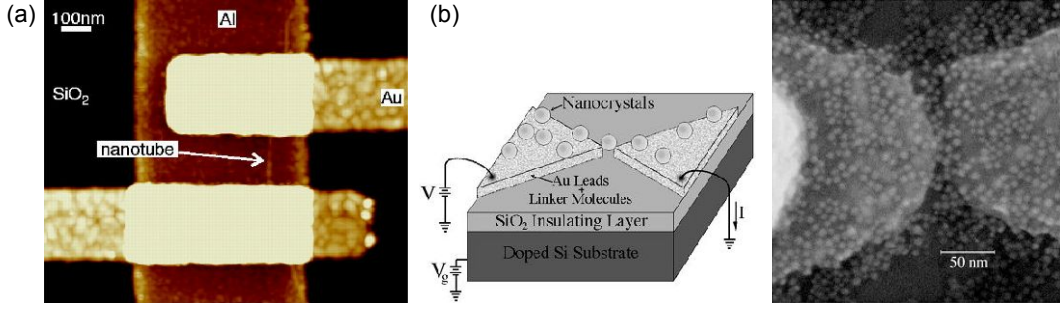


Figure 1.2: (a) A carbon nanotube field-effect transistor [7], and (b) a single-electron transistor made from a cadmium selenide nanocrystal [8]

microscopy [1], scanning probe microscopy [2, 3], and microfabrication techniques [4]. The timely discovery of nanometer-scale materials—such as fullerenes [5] and carbon nanotubes [6]—has also provided physicists new toys to play with. However, the generous funding into nano-related research is based on the aforementioned *business model*, and hence the scientist carries the burden to show that his or her research has economic, as well as scientific, significance.

This thesis is not an exception to this rule. At its core, this thesis concentrates on mechanics and surface metrology at the nanometer scale. It is enthralling to see that, in addition to simply toying with nanometer-scale structures and seeing their shapes, we can quantitatively analyze the mechanical bending processes, and discuss the uncertainties in measuring the structural dimensions at this scale. But an equivalent *a priori* effort has been put into ensure a practical significance of the research. *Surface-bound* nanostructures were chosen because the unique properties of nanowires and nanoparticles make them interesting electrical components, and because *nanoelectronics* implicitly assumes that the components are assembled on surfaces and interconnected (Fig. 1.2). A good understanding of the material properties and the structural dimensions is essential for a successful large-scale integration of electrical components and a fail-free operation of the produced device [4].

In Chapter 2, atomic force microscope (AFM), the main instrument used in this thesis, is introduced. In Chapter 3, the strategies and methods for preparing surface-bound nanostructures are described. Chapter 4 focuses on the mechanical properties of suspended carbon nanotubes. It will be shown that the material properties can shed light on the growth mechanism of carbon nanotubes, a subject of enormous interest. Chapter 5 is devoted to the size measurement of surface-bound metal nanoparticles, whose catalytic and optical properties are heavily size-dependent. It will be shown that a good understanding of the dynamic AFM is a prerequisite to identifying and studying the issues in nanoparticle metrology. Finally, the AFM manipulation of surface-bound structures is discussed, before general conclusions and the ideas for future research are given in Chapter 7.

It is the author's hope that this thesis is scientifically interesting, while at the same time carrying messages of practical importance.

2 Atomic Force Microscopy

An atomic force microscope (AFM) is a surface metrology instrument designed to study nanometer-scale features of very flat surfaces. For didactic and application purposes, it is useful to think of an AFM as a nanometer-scale stylus profilometer. Differences in the probe dimensions, the force loading mechanism, and the probe-sample-position control system allow AFM better vertical and lateral resolutions. Basic principles of contact atomic force microscopy (AFM), force curve technique, and dynamic AFM are explained, and the sensitivity of AFM is discussed.

2.1 Stylus Profilometer

A stylus profilometer is widely used in engineering sciences and industries to study the roughness and the shape of machined surfaces [9]. A diamond stylus connected to a cantilever arm is put into contact with a specimen surface (much like a phonograph), and the specimen is pulled laterally while the stylus stays in contact with the surface [Fig. 2.1(a)]. The vertical motion of the cantilever arm, recorded as a line trace, follows the topography of the scanned surface. Parallel line traces obtained at regular intervals can be combined to reconstruct the three-dimensional surface.

It is the stylus that determines the resolution and the accuracy of contact profilometry. A stylus typically has a conical shape with half-angle around 30° and tip radius around $2\text{ }\mu\text{m}$. Whether the trajectory of a stylus in contact is faithful to the surface topography or not depends on the relative geometry. Asperities sharper than the stylus will appear wider, and pits narrower than the stylus will appear shallower [Fig. 2.1(b)].

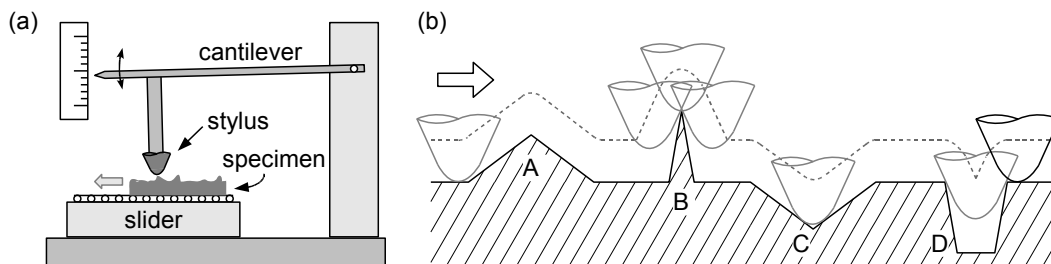


Figure 2.1: (a) Schematic of a stylus profilometer. (b) Dashed line is the line profile obtained from the stylus trajectory. While the stylus follows the shape of asperity A with a good accuracy, it overestimates the width of asperity B. Pit D appears shallower than pit C, in contradiction to the actual dimensions.

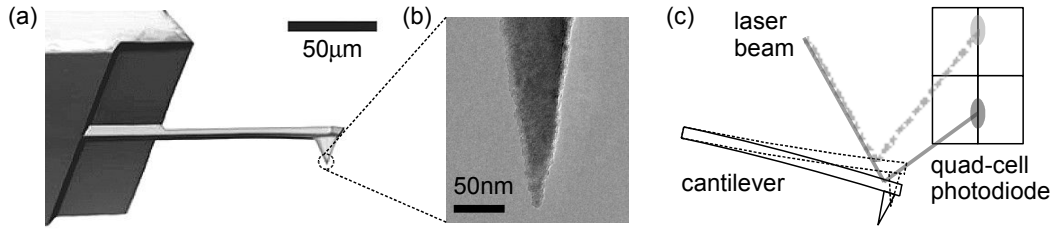


Figure 2.2: SEM images of (a) a silicon cantilever and (b) its tip. (c) The optical lever technique amplifies small cantilever deflections into large changes in the photodiode current signal.

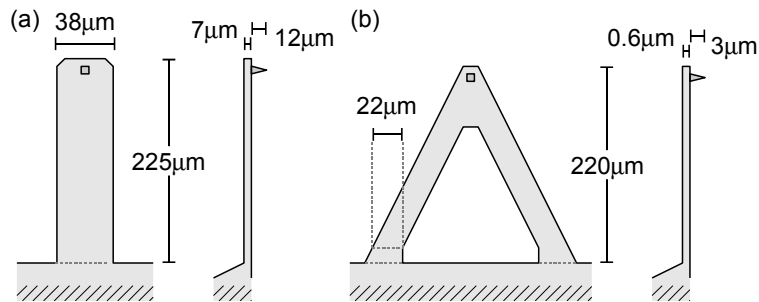


Figure 2.3: (a) Top and side views of a rectangular cantilever. Shown are the dimensions for NanoSensors NCL. (b) Top and side views of a triangular cantilever. Shown are the dimensions for Veeco Microlever D.

The measured height of an asperity, however, remains accurate as long as the mechanical deformation is negligible. These metrological characteristics extend into atomic force microscopy.

Using a sharper stylus brings immediate improvements to the accuracy and the lateral resolution. But a sharper stylus on the same loading mechanism (typical force $> 1 \mu\text{N}$) translates into increased contact pressure, making fracture and wear more likely for both the stylus and the specimen. The lateral resolution may become limited by the translation stage instead of the stylus, as a typical motor-driven stage is not ideal for nanometer-scale movements. A sharper tip must thus be accompanied by a more sensitive force control mechanism, as well as a positioning system of a higher resolution. These are the core differences between a stylus profilometer and an AFM.

2.2 Micro-fabricated Tip and Cantilever

Microfabricated silicon (Si) or silicon nitride (Si_3N_4) cantilevers [Fig. 2.2(a)] are the most common probes used in AFM. A micro-fabricated tip located at the end of such a cantilever [Fig. 2.2(b)] takes on the role of stylus in a stylus profilometer. The cantilever, whose deflection can be measured using the optical lever technique [Fig. 2.2(c)], acts as the force sensor. Rectangular [Fig. 2.3(a)] and triangular [Fig. 2.3(b)] designs are popular. Recently, metal AFM cantilevers have been realized [10]. These cantilevers,

designed for electrical measurements, promise a better performance than the doped-Si or the platinum-coated cantilevers.

2.2.1 Dynamic Calibration Methods

The calibration of cantilever spring constant is an issue that has spawned a large number of theoretical and experimental studies. In Sader and Cleveland methods, the cantilever is driven over a frequency range and its spring constant is calculated from the dynamic response (see Ref. [11] and the works cited therein). The Sader *unloaded-resonance* method uses the dynamic response along with the cantilever's plan-view dimensions (length and width), and has the advantage of being non-destructive while being limited to rectangular cantilevers. In the Cleveland *added-mass* method, one monitors the changes in the dynamic response after attaching an additional mass (usually tungsten beads). This method is applicable to cantilevers of all designs, but the calibration process can be time-consuming and destructive. Thermal fluctuations of the cantilever (with no external driving force) can also be used for the spring constant calibration, if a signal sampling rate well beyond the cantilever resonance frequency (10~500 kHz) is provided [12].

2.2.2 Reference Devices

Cumpson and co-workers have recently devised various MEMS (MicroElectroMechanical Systems) devices for the calibration of normal and torsional spring constants [13, 14, 15]. These devices allow a convenient and precise calibration, especially for triangular Si_3N_4 cantilevers. The *lateral electrical nanobalance* [15] is the first device designed for the calibration of the torsional spring constant, and hopefully it will provide a direct evidence for the susceptibility of triangular AFM cantilevers to lateral forces [16, 17].

2.3 Piezo-Driven Positioning Stages

Positioning stages driven by piezoelectric actuators are used for smooth and precise movements at the nanometer scale. These stages are called *scanners* in the AFM literature because images are obtained by raster scanning the tip or the sample.

2.3.1 Tube Scanners

Tubes made from PZT (lead zirconate titanate) were traditionally used as AFM scanners, and two different designs prevailed. In the sample-scanning design [Fig. 2.4(a)], the piezo tube controls the sample position in three dimensions. This design offers good AFM characteristics, but is limited to small samples. In the tip-scanning design [Fig. 2.4(b)], the tube controls the probe position in three dimensions. While the tip-scanning design permitted larger samples (silicon wafers, for example), a tip-scanning

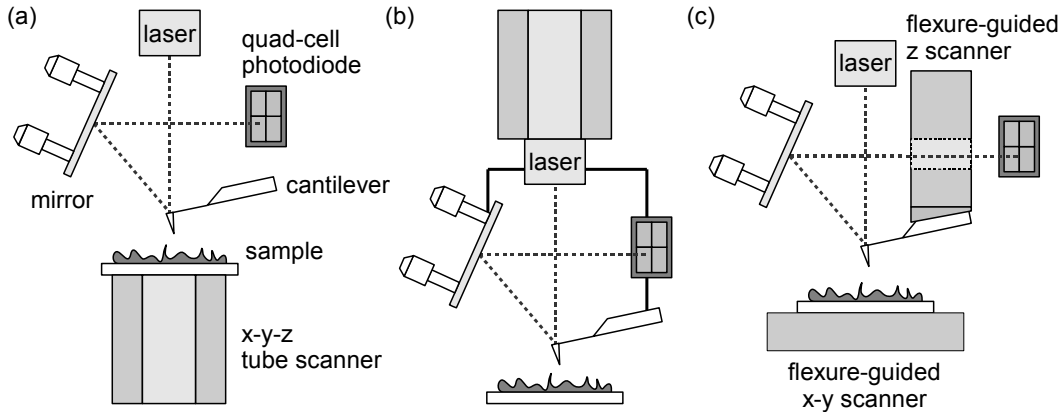


Figure 2.4: (a) A sample-scanning design using a tube scanner. (b) A tip-scanning design using a tube scanner. (c) The XETM (crosstalk-elimination) design from Park Systems. A 2-D flexure-guided scanner moves the sample in the x-y plane, and a 1-D flexure-guided scanner moves the tip along the z axis.

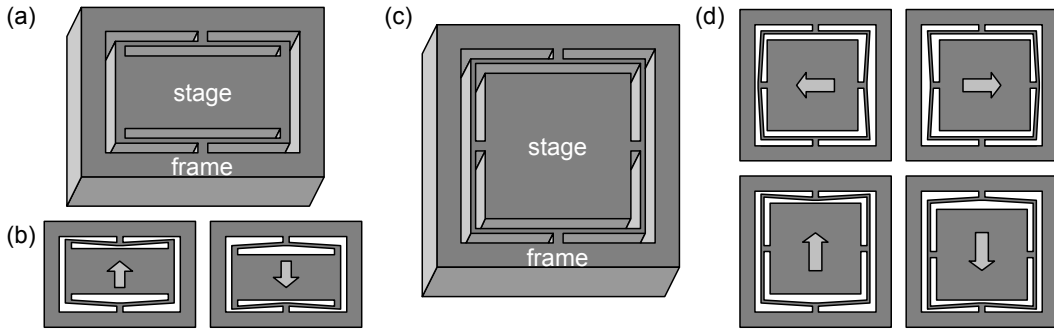


Figure 2.5: (a) The design and (b) the motion of a linear (1D) flexure-guided scanner. (c) The design and (d) the motion of a planar (2D) flexure-guided scanner.

AFM usually did not operate as well as a sample-scanning AFM, because the additional mass (laser, mirror, photodiode, and a frame for these components) carried by the piezo tube resulted in a degradation of the dynamic response.

2.3.2 Flexure-Guided Scanners

Flexure-guided structures are becoming increasingly popular¹ as they can be used to solve many problems inherent in the tube-scanner designs. A block of metal, onto which thin flexural hinges are created through the wire EDM (Electrical Discharge Machining), can be used as a one-dimensional (1D) or two-dimensional (2D) scanner (Fig. 2.5). The force needed to displace the inner stage is generated by multilayer piezo actuators installed inside the scanners (not drawn in Fig. 2.5).

¹Most of the commercial AFM models launched after 2002 employ flexure-guided scanners: Asylum Research MFP-3D series, Park Systems XE series and JPK NanoWizard, in the order of product launch dates. Veeco, the current market leader, has launched some new models using tube scanners, but these models inherit their designs from Veeco's former products.

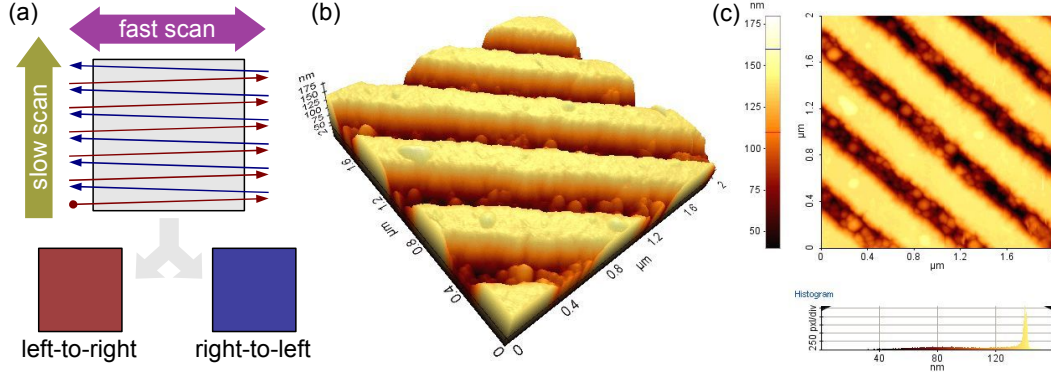


Figure 2.6: (a) AFM images are obtained by raster scanning. Two images are generated for each scan, one for each fast-scan direction. (b) 3D presentation of the AFM topography data on a GaAs sample with v grooves. (c) 2D presentation. Pixel color corresponds to the height data. A color map must accompany a 2D AFM image. A histogram of height data is useful for determining the sample roughness.

Flexure-guided scanners allow an elegant positioning scheme [Fig. 2.4(c)] that successfully addresses many important issues. The background curvature in AFM images caused by the bowing motion of the tube scanner is practically eliminated, and the compromise between the sample size and the scanner response is much less severe [18]. A flexure-guided scanning system allows a near-ideal control of the tip-sample displacement. However, as flexure-guided scanners are still driven by piezoelectric elements, issues of nonlinearity, hysteresis and creep remain, and they must be accounted for (see Appendix A).

2.4 Data Presentation

Topography data is acquired by raster-scanning the tip or the sample and continuously recording the height data [Fig. 2.6(a)]. A typical AFM image size is 256 pixels by 256 pixels (256×256). For a $10 \mu\text{m} \times 10 \mu\text{m}$ scan area, a pixel in a 256×256 image corresponds to an area of $39.1 \text{ nm} \times 39.1 \text{ nm}$. The height data is averaged over a pixel area to avoid aliasing effects.

As the gathered data is three-dimensional (3D) surface topography, it is natural to present the data in 3D [Fig. 2.6(b)]. However, it is often more practical to use a coloring scheme to present the height data with in 2D [Fig. 2.6(c)]. AFM data will be presented as 2D colored images throughout this thesis, unless stated otherwise.

AFM data acquisition is slow. Scan rate for the fast scan direction is typically below 5 Hz, which means that a 256×256 image takes more than 50 seconds to acquire. Because of the long acquisition time, ambient AFM data often contain noise related to thermal drifts. A flat surface may appear sloped or even curved in an AFM image

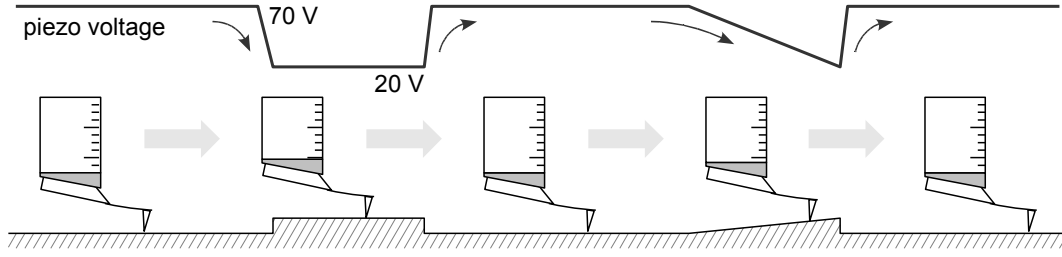


Figure 2.7: In contact AFM, the cantilever deflection is kept constant through a feedback loop. The z scanner voltage signal gives the inverted line profile of the scanned surface. The voltage values are arbitrary.

because of a thermal-expansion-related drift in the z scanner position. The thermal-drift noise can dominate the height data for very flat surfaces.

Another common issue in the AFM data presentation is the background sample slope. When the sample surface is not perfectly parallel to the x–y lateral-scan plane, the sample slope can dominate the height data and make small features invisible.

AFM data analysis software usually includes a range of *flattening* functions to correct the sample slope and the thermal-drift-related noise. These functions, however, must be used with care because they can distort the AFM image. Physical solutions, such as a tilting stage on top of the sample holder to eliminate the background slope [19], offer a better reliability.

2.5 Contact AFM

Contact AFM operation is similar to the operation of a stylus profilometer, with one key difference: instead of observing the cantilever deflection as the tip is scanned over the sample, the cantilever deflection is kept constant through a feedback loop controlling the z scanner position, and the surface topography is calculated from the output of the feedback loop, namely the voltage applied to the z scanner (Fig. 2.7).

There are two main reasons for this added complexity. First, the optical lever system is optimized for sensitivity, which comes at the cost of a reduced detection range (~ 100 nm deflection). As the z scanners in commercial AFMs can usually cover ranges as large as $10\text{ }\mu\text{m}$, by using the feedback control we can analyze samples with features taller than the optical lever’s detection range. Secondly, keeping a constant loading force between the tip and the sample is often necessary to control the tip–sample damage and wear.

The net force on the cantilever must be zero if the cantilever deflection stays constant at z (positive for an upward deflection and negative for a downward deflection) in contact with the sample. The total force on the cantilever is a sum of the restoring force F_k ,

$$F_k = -kz, \quad (2.1)$$

where k is the cantilever spring constant, and the tip-sample interaction force F_{ts} , which is in turn a sum of the tip-sample adhesion force F_{ad} and the tip-sample contact force F_{ct} .

$$F_k + F_{ts} = 0, \quad (2.2)$$

$$F_{ts} = F_{ad} + F_{ct}. \quad (2.3)$$

By keeping the cantilever deflection constant, we can keep F_k and thus F_{ts} constant, often to an absolute value less than 1 nN.

It is important to remember that F_{ct} , the contact force responsible for tip-sample damage and wear, is not directly proportional to F_k .

$$F_{ct} = -(F_k + F_{ad}). \quad (2.4)$$

Under ambient conditions, the adhesion force F_{ad} often outweighs F_k , resulting in a large F_{ct} . F_{ad} is a sum of the van der Waals force F_{vdW} , the electrostatic force F_{el} , the capillary force F_{cap} and the chemical force F_{chem} [20]:

$$F_{ad} = F_{vdW} + F_{el} + F_{cap} + F_{chem}. \quad (2.5)$$

F_{el} , F_{cap} and F_{chem} can be reduced to negligible values by controlling the environment, but F_{vdW} always remains, albeit being usually smaller than F_k . In ambient AFM with no humidity control, F_{cap} is often the dominant force.

Scanning the tip over the sample in contact generates a tip-sample friction due to F_{ct} . The lateral shear force from friction cause a torsional deflection of the cantilever, and subsequently appear in the lateral position of the laser beam spot on the quad-cell photodiode signals [for the design shown in Fig. 2.2(c)]. For solid samples, these changes can be used to estimate the tip-sample friction, or at least to compare different surfaces [21]. This application is called lateral force microscopy (LFM) or friction force microscopy (FFM). For soft samples such as biological specimens, the shear forces can cause a substantial sample deformation and make the imaging difficult.

2.6 Force Curves

An important application of the contact AFM is the force curve technique. The z scanner approaches the sample until the tip jumps into contact with the surface, and then, after reaching a predefined deflection limit, the scanner retracts until the tip jumps off contact (Fig. 2.8). The slope of a force-displacement curve in the contact range, and the force required to pull the tip off contact are the two main quantities that characterize the cantilever-tip-sample-environment system [22].

By using chemically or biologically modified tips, we can use the force curve technique

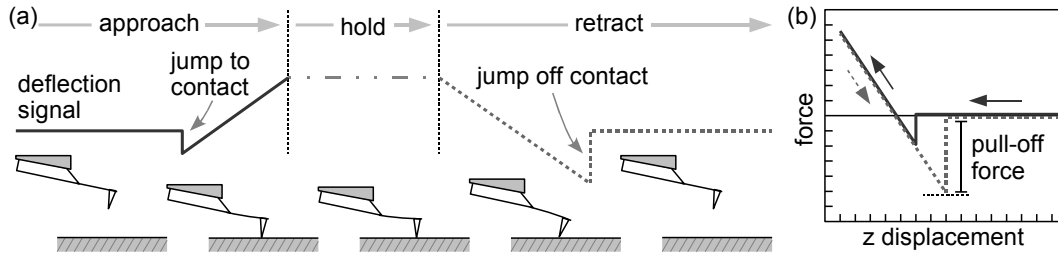


Figure 2.8: (a) In the force curve technique, the tip slowly into contact with the surface and then comes off contact. (b) The cantilever deflection and the z position data during the approach and the retraction are plotted in the form of a force–displacement curve.

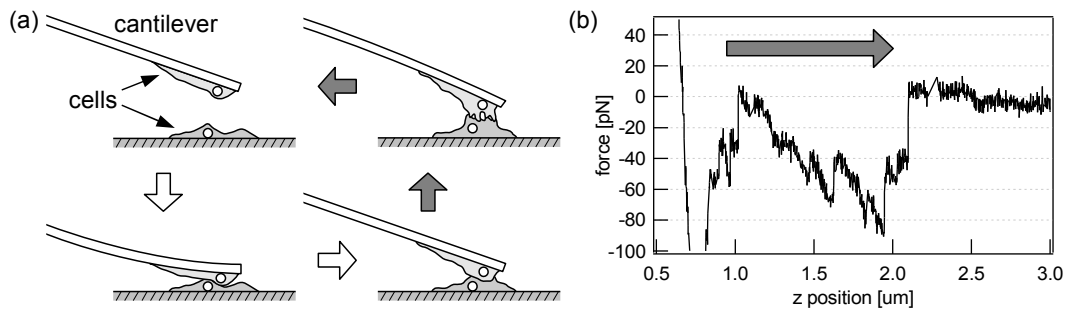


Figure 2.9: Cell–cell adhesion can be studied by pushing two cells into contact and then pulling them apart. (a) A cell is mounted on a tipless AFM cantilever, and the force curves are acquired on top of another cell. (b) The retraction curve contains many discrete jumps, which in this case of fibroblast–fibroblast cell adhesion correspond to the ruptures of single cadherin–cadherin bonds [23].

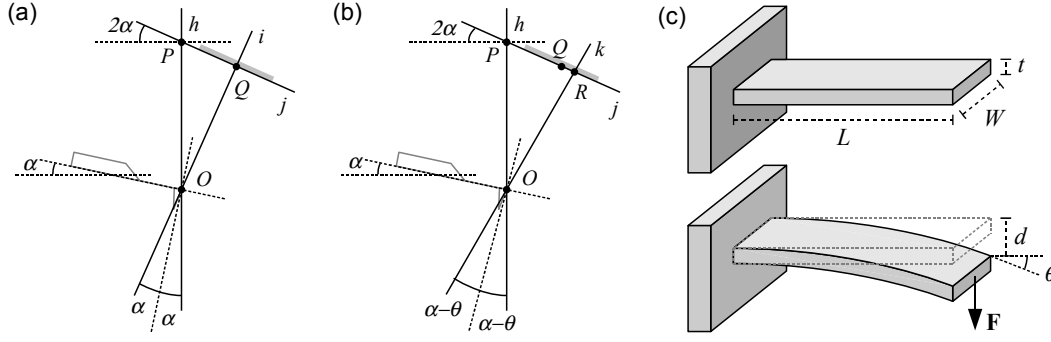


Figure 2.10: (a) Geometry of optical lever before deflection. α : cantilever mounting angle; h : incident laser beam; i : reflected laser beam; Q : laser spot on the photodiode. (b) Geometry of optical lever after cantilever deflection by angle θ . For a downward deflection, θ is negative. R : new position for the laser spot on the photodiode. (c) Deflection of a clamped rectangular beam.

to study the rupture of single covalent or specific biological bonds (antibody–antigen binding, for example) [20]. Even the cell–cell adhesion can be studied, by using a cell glued onto a tipless cantilever as the probe. A study of cell adhesion between fibroblast cells [23] is depicted in Fig. 2.9.

The popularity of the force curve technique (also called *force spectroscopy* by biologists who vary the loading rate, the contact time, the temperature, and other parameters) is due to the excellent force sensitivity of the AFM. The minimum resolvable force δF_k is a product of $\delta\theta$, the angular resolution of an AFM system, and $\delta F_k/\delta\theta$, the force resolution of an AFM cantilever. $\delta\theta$ is an instrument-dependent value that should be provided by the AFM manufacturer, and $\delta F_k/\delta\theta$ is a cantilever property that is calculated by

$$\frac{\delta F_k}{\delta\theta} = \frac{2}{3} k L, \quad (2.6)$$

where L is the cantilever length. Nominal k and L values are available in a cantilever datasheet. Si_3N_4 cantilevers generally offer a better force sensitivity than silicon cantilevers. Eq. 2.6 is derived in the next section.

2.7 Contact AFM Force Sensitivity

The force sensitivity of the contact AFM depends on a number of factors: the photodiode sensitivity, the optical lever geometry, the cantilever geometry, and the cantilever spring constant. It is important to remember that the optical lever technique detects the cantilever deflection angle. Figure 2.10(a) shows the geometry of an optical lever before a cantilever deflection. The cantilever is by default mounted at a non-zero angle α , 12° in our case. The laser beam falls from point P to point O on the cantilever, and reflects off to arrive at point Q on the photodiode. α , P , and j are fixed by the

2 Atomic Force Microscopy

AFM design. As the position change of O due to the cantilever deflection is usually very small compared to the lengths OP and OQ , the point O can be considered to be fixed, making the length OP a constant. Taking O as the origin and h as the y axis of a Cartesian plane, the coordinates of Q are given by

$$Q : (\frac{OP}{\tan 2\alpha + \cot 2\alpha} , \frac{OP \cot 2\alpha}{\tan 2\alpha + \cot 2\alpha}) \quad (2.7)$$

Now consider the case where the cantilever has deflected slightly, so that the cantilever deflection angle at O changed by θ [Fig. 2.10(b)]. The new laser beam spot on the photodiode is the point R , whose coordinates are

$$R : (\frac{OP}{\tan 2\alpha + \cot 2(\alpha - \theta)} , \frac{OP \cot 2(\alpha - \theta)}{\tan 2\alpha + \cot 2(\alpha - \theta)}) \quad (2.8)$$

The distance QR , which is the signal that the quad-cell photodiode measures, is then

$$QR = OP \cos 2\alpha \tan 2\theta = OP \cos 2\alpha \frac{2 \tan \theta}{1 - \tan^2 \theta} \quad (2.9)$$

If θ is small, a condition that is usually satisfied in AFM, QR can be approximated as

$$QR \approx 2 OP \cos 2\alpha \theta \quad (2.10)$$

OP and α are system parameters (fixed by the AFM design), and θ is the cantilever deflection caused by the tip-sample interaction. For small values of θ , QR is proportional to θ .

The sensitivity of an AFM system can be characterized by the smallest resolvable angle $\delta\theta$, which depends on the AFM design parameter OP and the photodiode resolution δQR by the following equation:

$$\delta\theta = \frac{\delta QR}{2 OP \cos 2\alpha} \quad (2.11)$$

AFM manufacturers should specify $\delta\theta$ of their systems.

Now the question is how much force a given angular resolution $\delta\theta$ corresponds to. It is the cantilever that determines this value. Let us consider a rectangular cantilever with the dimensions shown in Fig. 2.10(c). Under the tip-sample force F_k , the cantilever will deflect by z . The deflection z and angle θ are given by

$$z = \frac{L^3}{3 E_k I_k} F_k \quad (2.12)$$

$$\theta \approx \tan \theta = \frac{L^2}{2 E_k I_k} F_k \quad (2.13)$$

where E_k is the elastic modulus of the cantilever material, and I_k is the second moment of inertia. I_k for a rectangular cantilever is $W b^3/12$, where W is the cantilever

2.7 Contact AFM Force Sensitivity

Material	Manufacturer	Model		k [N/m]	L [μm]	$\delta F_k/\delta\theta$ [pN/0.001°]
Si ₃ N ₄	NanoSensors	PNP-DB	Short	0.48	100	560
			Long	0.06	200	140
	Olympus	Biolever	Short	0.03	60	21
			Long	0.006	100	7.0
	Veeco	Microlever	A	0.05	180	100
			B	0.02	200	47
			C	0.01	320	37
			D	0.03	220	77
			E	0.1	140	160
			F	0.5	85	490
		NP	A	0.58	115	780
			B	0.12	196	270
			C	0.32	115	430
			D	0.06	196	140
	BudgetSensors	SiNi	Short	0.27	100	310
			Long	0.06	200	140
Si	NanoSensors	CONT		0.2	450	1000
	Veeco	CONT10		0.1	450	520
		CONT20		0.9	450	4700
	MikroMasch	Series 17		0.15	460	800
		Series 19		0.6	125	870
		Series 37	A	0.35	300	1200
			B	0.3	350	1200
			C	0.65	250	1900
		Series 38	A	0.05	300	170
			B	0.03	350	120
			C	0.08	250	230
	BudgetSensors	Contact		0.2	450	1000

Table 2.1: Force resolution of commercial AFM cantilevers. Cantilevers with a force resolution better than 100 pN/0.001° are noted in boldface.

width and b is the cantilever thickness. The spring constant k of the cantilever is thus $3 E_k I_k / L^3$. The minimum resolvable force δF_k is then

$$\delta F_k = \frac{2}{3} k L \cos \alpha \delta \theta \quad (2.14)$$

It is now clear that the spring constant alone does not determine the force resolution. Cantilever length is just as important. The force resolution $\delta F_k/\delta\theta$ values of some commercial AFM cantilevers are listed in Table 2.1. Si₃N₄ cantilevers in general offer better force sensitivity than Si cantilevers.

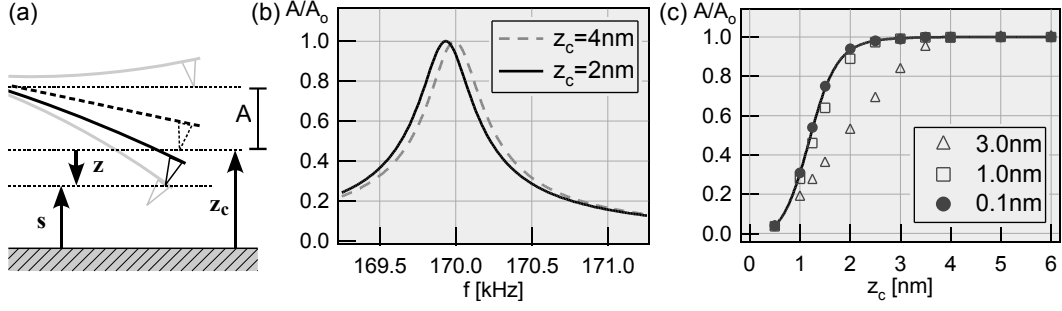


Figure 2.11: (a) In the non-contact AFM, the tip feels only the attractive van der Waals force. z_c : the tip-sample rest separation; z : the tip deflection from its rest position; s : the instantaneous tip-sample separation. $z_c + z = s$. (b) The surface force gradient changes the cantilever's effective spring constant, and consequently its effective resonance frequency. Shown are the frequency response curves (analytical solutions) at different rest separations. (c) Equation 2.20 is valid only for small amplitudes. The difference between an analytical approximation using Eq. 2.20 (solid curve) and a numerical solution for the 3.0 nm initial amplitude A_o case (triangles) is substantial. The difference is smaller for the 1 nm A_o case (squares), and negligible for the 0.1 nm A_o case (circles). Conditions: $H = 40 \text{ zJ}$; $R = 15 \text{ nm}$; $f_R = f = 170 \text{ kHz}$; $Q = 500$.

2.8 Dynamic AFM

In the dynamic AFM, the cantilever is excited externally (usually through a separate *dither* piezo that drives the cantilever base), and changes in the cantilever's dynamic response in the vicinity of the sample surface are monitored to obtain the topography image. Two different approaches to the dynamic AFM prevailed until the late 1990s: non-contact and intermittent-contact.

2.8.1 Non-Contact AFM

Initiated by the work of Martin et al. [24], the non-contact AFM (NC-AFM) uses an oscillating cantilever to detect the van der Waals force gradient. For an AFM tip near a flat surface, the equation

$$F_{vdW}(s) = -\frac{H R_t}{6 s^2} \quad (2.15)$$

serves as a good approximation for the attractive van der Waals force F_{vdW} . H is the tip-sample Hamaker constant, R_t is the tip radius, and s is the tip-sample separation. The force gradient is then

$$\frac{dF_{vdW}}{ds} = \frac{H R_t}{3 s^3}. \quad (2.16)$$

The equation of motion for a harmonic oscillator driven in this attractive field is

$$m^* \ddot{z} + \frac{m^* \omega_R}{Q} \dot{z} + k z = F_o \cos \omega t + F_{vdW}(z_c + z), \quad (2.17)$$

where z and z_c are the instantaneous cantilever deflection and the tip-surface rest separation, respectively, as depicted in Fig. 2.11(a). F_o is the amplitude of a sinusoidal driving force, ω ($=2\pi f$) is the driving frequency, and t is the time. k is the spring constant, Q is the quality factor, ω_R ($=2\pi f_R$) is the resonance frequency, and m^* is the effective mass ω_o^2/k , where ω_o is the natural frequency calculated as $\omega_R/\sqrt{1-Q^2/2}$.

For small cantilever oscillations, the attractive force may be expanded to

$$F_{vdW}(z_c + z) = F_{vdW}(z_c) + \left. \frac{dF_{vdW}}{ds} \right|_{s=z_c} z, \quad (2.18)$$

so that Eq. 2.17 is rewritten as

$$m^* \ddot{z} + \frac{m^* \omega_R}{Q} \dot{z} + \left(k - \left. \frac{dF_{vdW}}{ds} \right|_{s=z_c} \right) z = F_o \cos \omega t + F_{vdW}(z_c). \quad (2.19)$$

Hence the surface force gradient changes the effective spring constant of the cantilever.

If the cantilever is driven at a fixed frequency, the amplitude and the phase of the cantilever oscillation changes with the tip-surface separation [Fig. 2.11(b)]:

$$A(z_c) = \frac{F_o/m^*}{\sqrt{(\omega'_o(z_c)^2 - \omega^2)^2 + (\omega'_o(z_c)\omega/Q)^2}}, \quad (2.20)$$

$$\tan \theta(z_c) = \frac{\omega'_o(z_c)\omega/Q}{\omega'_o(z_c)^2 - \omega^2}, \quad (2.21)$$

$$\omega'_o(z_c) = \sqrt{\left(k - \left. \frac{dF_{ts}}{ds} \right|_{s=z_c} \right) / m^*}. \quad (2.22)$$

A small free amplitude (A_o) below 1 nm is necessary for these approximations to be accurate [Fig. 2.11(c)], but nonetheless smooth amplitude and phase changes can be detected even for larger free amplitudes. The amplitude and the phase signals can be used as inputs of a z scanner feedback loop to obtain the equigradient surface. Amplitude-modulation AFM (AM-AFM), the most common implementation of the dynamic AFM, keeps the amplitude change constant. Alternatively, the cantilever can be excited into resonance, so that the resonance frequency signal is used as the feedback input. Frequency-modulation AFM (FM-AFM) operates by keeping the resonance frequency change constant [25].

Despite the apparent simplicity, the NC-AFM did not become popular with the general AFM community. It was partly due to the noise issues with the first-generation commercial AFM systems that prevented a stable small-amplitude oscillation, and partly due to the marketing efforts by a market-leading AFM manufacturer Veeco to promote *Tapping-Mode*TM over the non-contact operation. Non-contact AFM remained a niche application for researchers with home-built AFMs.

2.8.2 Intermittent-Contact AFM

*Tapping-Mode*TM, or the intermittent-contact AFM (IC-AFM) was more popular with the general community. The IC-AFM uses large oscillations (20–500 nm), so that the tip goes in and out of contact in every oscillation cycle. As large amplitudes are used, the amplitude detection and the feedback control is less challenging. Contact forces generated during these intermittent contacts limit oscillation amplitude. The main advantage of the IC-AFM is that the shear forces inherent in the contact AFM can be avoided [26]. Signals from high-order harmonics can also be used, which is useful for imaging in liquids [27].

However, as the theoretical understanding of IC-AFM matured, criticisms surfaced against the advertised notion that the IC-AFM is ideal for all applications. Stiff cantilevers are often used at high frequencies, and the contact pressure generated during a cycle can be large enough to cause an irreversible and substantial tip and sample damage (especially for stiff samples) [28]. Many researchers have used IC-AFM phase images to represent their samples—because it often gave the best contrast—without understanding the significance of the IC-AFM phase signal. Contrast in the phase images (and sometimes even the topography images) was found to depend on numerous geometrical and material properties that could not be distinguished in a quantitative manner [29].

2.8.3 Bistability of Oscillating Cantilever

The bistability of a cantilever oscillating near a surface had been reported earlier [30], but breakthroughs in the understanding of dynamic AFM came in the late 1990s with pioneering works by Cleveland et al. [31] and Garcia et al. [32]. Their contribution was to explain important phenomena such as the bistability and the hysteresis in amplitude–phase–distance (APD) curves² by introducing a realistic contact force into the equation of motion (Eq. 2.17).³ It was shown that the cantilever can oscillate in either the attractive non-contact regime (NC-AFM) or the repulsive intermittent-contact regime (IC-AFM), the probability of each regime depending on the rest separation, the initial conditions, and the tip–sample interaction parameters. The IC-AFM is more likely for large amplitude oscillations on surfaces with low van der Waals forces (low Hamaker constant), while the NC-AFM is more probable for small-amplitude oscillations on high-

²Similar to the force curve, but the oscillation amplitude and phase signals are collected in place of the dc deflection.

³A previous work on IC-AFM numerical simulation by Burnham et al. [28] had taken an even more rigorous approach, but issues in the subject focus and the data presentation prevented the work from having a similar impact. Data was not presented as APD curves, but as instantaneous deflection–position graphs. While useful for visualizing the cantilever motion, the deflection–position graphs were difficult to compare with experimental data that often came in the form of APD curves. Also, the deflection–position visualization made it difficult to compare the approach and the retraction curves, which may explain why the authors did not pay attention to the bistable and hysteretic behavior of the oscillating cantilever.

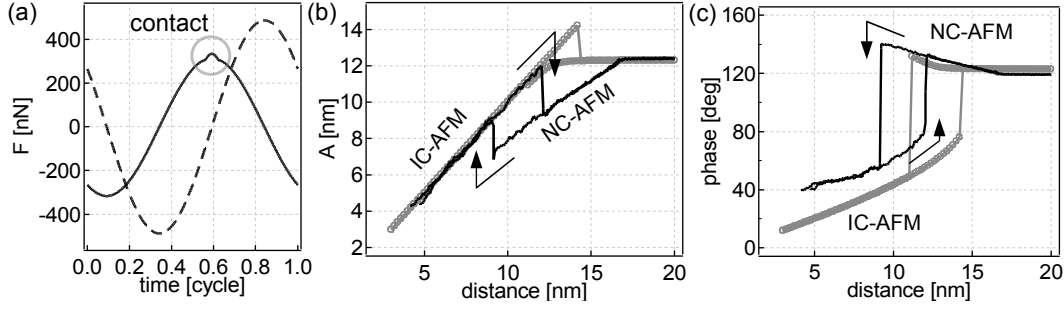


Figure 2.12: (a) Numerical solutions for the total force on an oscillating cantilever at $z_c = 15$ nm (dashed curve) and $z_c = 8$ nm (solid curve). The bump on the solid curve is the force generated by contact (~ 30 nN). (b) Experimental (solid red line) and simulated (blue circles) amplitude-distance curve for the approach and the retraction of an oscillating silicon tip on a gold surface. (c) Phase-distance curves. Parameters: $k = 32$ N/m; $f_R = 167.16$ kHz; $Q = 600$; $f = 167.25$ kHz; $A_o = 12.3$ nm; $A_o = 12.3$ nm.

Hamaker-constant surfaces. Phase signals can be used to tell whether the operation is NC-AFM or IC-AFM.

When the contact force is included, the equation of motion becomes

$$m^* \ddot{z} + \frac{m^* \omega_R}{Q} \dot{z} + kz = F_o \cos \omega t + F_{ts}(z_c + z), \quad (2.23)$$

$$F_{ts}(s) = \begin{cases} F_{vdW}(s) & \text{if } s > a_o, \\ F_{vdW}(a_o) + F_{ct}(s) & \text{if } s \leq a_o, \end{cases} \quad (2.24)$$

where F_{ts} is the tip-sample interaction force whose expression depends on the tip-sample separation, $F_{ct}(s)$ is the force generated by contact, and a_o is the interatomic spacing (typical value: 0.165 nm) that prevents F_{vdW} from diverging. The expression for $F_{ct}(s)$ depends on the contact model [22], and for DMT (Derjaguin-Müller-Toporov) contact mechanics,

$$F_{ct}(s) = K \sqrt{R} (a_o - s)^{\frac{3}{2}}, \quad (2.25)$$

$$\frac{1}{K} = \frac{3}{4} \left(\frac{1 - \nu_t^2}{E_t} + \frac{1 - \nu_s^2}{E_s} \right), \quad (2.26)$$

where E_t and E_s are the elastic moduli of the tip and the sample, respectively, ν_t and ν_s are the Poisson ratios of the tip and the sample, respectively, and K is the reduced tip-sample elastic modulus.

Equation 2.23 can be solved through a numerical simulation (see Section 5.4). By finding numerical solutions at different tip-sample rest separation values [Fig. 2.12(a)], we can simulate the APD curves. The simulated APD curves show bistability at certain separations, depending on whether the separation was reached during approach or retraction [Fig. 2.12(b) and (c)]. While the simulated curves correspond qualitatively

with the experimental data, there are two important differences: (a) the experimental NC-AFM and IC-AFM branches are farther apart than the simulated graph, and (b) the experimental NC-AFM branch appears much more linear. These differences are discussed in detail in Chapter [5].

2.8.4 Dynamic AFM Sensitivity

In the NC-AFM, fluctuations in the oscillation amplitude due to the thermal energy determines the smallest detectable van der Waals force gradient $\delta(dF_{vdW}/ds)$

$$\delta\left(\frac{dF}{ds}\right) = \sqrt{\frac{2k k_B T B}{\omega_o Q \langle z^2 \rangle}} \quad (2.27)$$

obtained at $\omega = \omega_o (1 \pm 1/\sqrt{8}Q)$. k_B is the Boltzmann constant, T is the temperature, and B is the bandwidth of the detection system, and $\langle z^2 \rangle$ is the time average of the square of cantilever deflection.

The IC-AFM detects the tip-sample contact force, and thus the IC-AFM sensitivity can also be described by Eq. 2.6 derived for the contact AFM.

2.9 AFM Modifications

XE-100 from Park Systems is the AFM used for this thesis work. XE-100 uses flexure-guided scanners for the sample movement in the x-y plane and the tip movement along the z axis [Fig. 2.4(c)] [18]. A detailed description of XE-100 is available on the Park Systems' website <http://www.parkafm.com>.

System modifications were necessary to carry out experiments described in this thesis. The main modifications are as follows.

Low-humidity chamber An air-tight plexiglass enclosure with gas flow has been designed to replace the original enclosure. Low humidity ($< 5\%$ relative humidity) can be achieved by blowing in dry nitrogen gas.

Scanner control through external signal Electronics of the controller and the signal access module has been modified so that the x-y and z scanners can be controlled through external analog signals. This modification was necessary to implement the APD curve acquisition and the haptic interface.

Lock-in reference signal output Reference signals for the internal lock-in amplifier have been wired to extra BNC connectors at the controller back panel. This modification facilitates the acquisition of APD curves using an external lock-in amplifier.

3 Preparation of Surface-Bound Nanostructures

Numerous methods exist for the synthesis of nanoparticles and nanowires, the two main strategies being the vapor-phase and the solution-phase syntheses. Nanostructures are often produced and stored in the colloidal form, and a dispersed deposition is necessary to study the individual properties of surface-bound nanostructures. A novel technique for the uniformly dispersed deposition, named “boil deposition”, was developed during the course of this thesis [33]. Boil deposition is more flexible and efficient than conventional methods such as self-assembly and spin coating.

3.1 Synthesis of Nanoparticles

3.1.1 Thin-Film Deposition

Metal nanoparticles can be created by depositing a thin film of metal atoms on a substrate and then allowing the atoms to coalesce under controlled conditions [34]. Widely available thin-film techniques such as evaporation, sputtering, or laser ablation are often used to deposit the source atoms. The main advantage is that the nanoparticles can be produced directly on desired substrates, made of any vacuum-compatible material. The components needed for the thin-film deposition can be built into reaction or measurement chambers, which is useful for experiments that need to avoid the oxidation or contamination of nanoparticles at intermediate stages [35]. The broad size distribution of the produced nanoparticles is, however, a major drawback.

3.1.2 Spray Pyrolysis

In spray pyrolysis, nanoparticles are produced from liquid drops of a precursor solution. For metal nanoparticles, metal salt (often chloride, nitrate, or acetate) solutions are used as precursors [36]. Micrometer-sized drops (microdrops) created by spraying are guided into a furnace, where pyrolysis takes place midair. Each microdrop becomes a single metal nanoparticle (or a metal oxide nanoparticle, depending on the precursor and the pyrolysis conditions). The nanoparticles are then collected on a substrate.

Size selection is possible by employing the nanometer differential mobility analyzer (nano-DMA) [37]. Nanoparticles produced by spray pyrolysis are charged negatively (through electron bombardment, for example), so that the particles of a narrow size

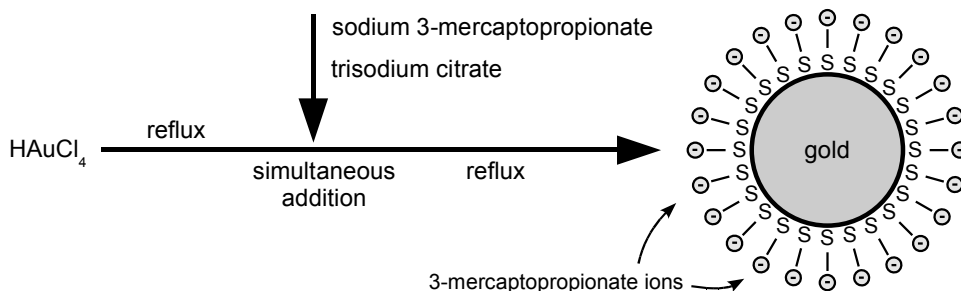


Figure 3.1: One-step synthesis of ligand-stabilized gold nanoparticles [43]

window can be filtered out using the difference in electrical mobility. The spray pyrolysis and the nano-DMA modules can also be built onto reaction or measurement chambers to serve as a source of monodisperse (narrow size distribution) nanoparticles [38].

3.1.3 Chemical Synthesis

Chemical synthesis is the most widespread method of producing metal and semiconductor nanoparticles [34]. Nanoparticles of various size, composition, and shape can be created through the chemical synthesis [39, 40]. The general strategy is to reduce metal salts or metal complexes in solution by adding reducing agents. After electrostatic or steric stabilization, the nanoparticles stay suspended in solvents in the colloidal form. Gold nanoparticle synthesis will be described as an example.

Gold Nanoparticle Synthesis by Citrate Reduction

The method reported by Turkevich et al. [41] in 1951 is widely used to prepare aqueous solutions of gold nanoparticles. Hydrogen tetrachloroaurate (HAuCl_4) solution is brought to boil, and at which point sodium citrate ($\text{Na}_3\text{C}_6\text{H}_5\text{O}_7$) solution is added. Citrate ions reduce Au^{3+} ions, producing gold atoms and other oxidation products (e.g. acetone dicarboxylate) [34]. Upon reaching the supersaturation limit, the gold atoms precipitate out as gold nanoparticles. Chloride (Cl^-) ions and the remaining citrate ions adsorb on the gold nanoparticle surface, making the nanoparticles negatively charged. Average gold nanoparticle size can be controlled from 5 nm to 100 nm by varying the sodium citrate–gold ratio [42].

Stabilization

Gold nanoparticle colloid prepared by the Turkevich method is generally stable. An electrical double layer forms around a nanoparticle due to the adsorbed chloride and citrate ions, and the Coulombic repulsion between the electrical double layers is strong enough to prevent agglomeration [34]. For a long-term stability, we can further cap the

nanoparticles with ligand molecules (e.g. 3-mercaptopropionate ions) [Fig. 3.1]. Stable nanoparticle colloids can be stored up to a few months.

While the chemical route allows a facile and cost-effective synthesis of monodisperse nanoparticles, the physicist, who is interested in the properties of individual particles, faces the practical problem of particle deposition. The liquid-suspended particles must be transferred onto a suitable support without aggregation. As it will be shown in Section 3.3, this is not a trivial problem.

3.2 Synthesis of Nanowires

3.2.1 High-Energy Synthesis

Crystalline nanotubes and nanowires can be created by “brute force”, by providing the high activation energy necessary for a natural synthesis. Carbon nanotubes can be created by passing a high current between two graphite electrodes separated by a small gap. The electrical arc discharge vaporizes the carbon atoms at the interface, and as the atoms condense, a small fraction crystallize in the form of nanotubes [6]. Vaporizing the carbon atoms by laser can also produce high-quality carbon nanotubes [44]. The high-energy synthesis is a general method, applicable also for inorganic nanowires [45, 46].

While the arc-discharge evaporation and the laser ablation can produce carbon nanotubes of perfect structure, most of the produced soot is made of graphite and other carbonaceous materials, and hence an extensive and time-consuming purification is inevitable. This is a serious drawback that makes the high-energy synthesis unsuitable for large-scale productions. The researchers are now concentrating their efforts on finding low-energy and high-yield routes for the nanotube/nanowire synthesis, as will be shown in the following subsections.

3.2.2 Vapor-Phase Synthesis Using Catalysts

Vapor-phase synthesis using catalytic chemical vapor deposition (CVD) has been actively studied for the growth of one-dimensional (1D) nanostructures (whiskers, rods, wires, belts, and tubes) [47]. Successful methods often employ the vapor–liquid–solid (VLS) mechanism, in which the precursor atoms or molecules in the *vapor* form dissolve into *liquid* metal nanoparticles and precipitate out as *solid* 1D nanostructures. Carbon nanotube (CNT) growth and zinc oxide (ZnO) nanowire growth will be described as examples.

Carbon Nanotube Growth by CVD

To grow carbon nanotubes by CVD, metal nanoparticles (usually iron, nickel, cobalt, or their alloys) are prepared on a support and exposed to a carbon-containing precursor gas such as acetylene (C_2H_2) vapor at a temperature in the range of 500–1000 °C. The

3 Preparation of Surface-Bound Nanostructures

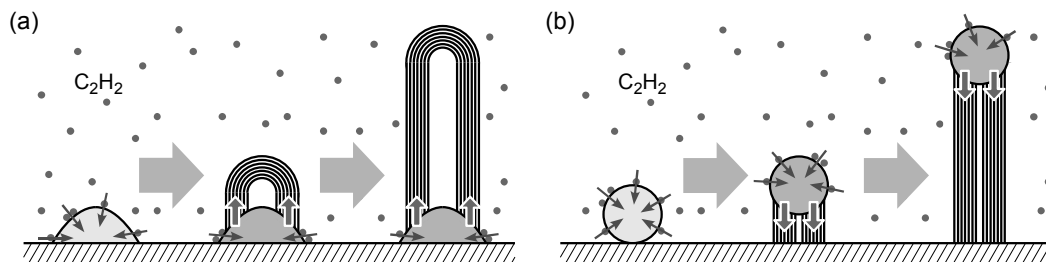


Figure 3.2: In the CVD synthesis of carbon nanotubes, carbon atoms from precursor molecules first dissolve into the catalyst and then precipitate out as the nanotube crystal. Both (a) the base growth and (b) the tip growth have been observed.

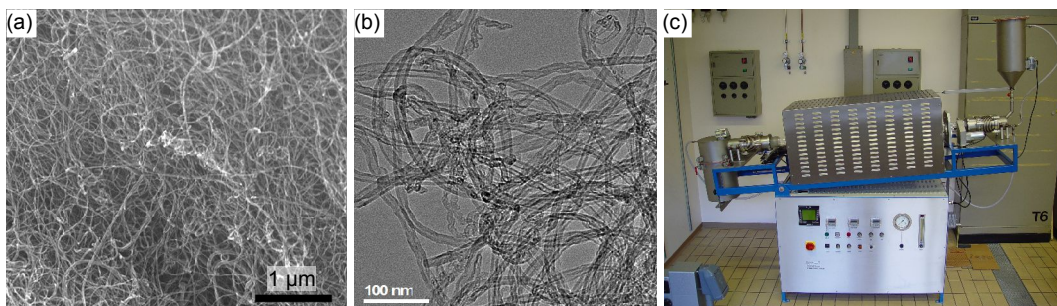


Figure 3.3: (a) SEM and (b) TEM images of multiwall carbon nanotubes grown by CVD, using cobalt ferrite (Fe_2Co) nanoparticles as the catalyst, magnesium oxide (MgO) as the support, and acetylene (C_2H_2) as the precursor. (c) Rotary tube furnace used for the synthesis.

precursor gas molecules dissociate on the metal nanoparticle surface, and the resulting carbon atoms dissolve into the nanoparticle. On surpassing the supersaturation limit, the carbon atoms precipitate out as a nanotube (Fig. 3.2). As the metal nanoparticle catalyzes the precursor dissociation as well as the carbon nanotube nucleation, the nanoparticle is called the *catalyst*. The typical product is a multiwall carbon nanotube (MWCNT) having a diameter in the range of 5–20 nm (Fig. 3.3) [48].

CVD is currently the most widespread method of producing carbon nanotubes.¹ Its popularity is mainly due to the large-scale production feasible with appropriate facilities [49, 50, 51] and the possibilities of controlling the length, the diameter, the orientation, and the growth sites [52].

The catalytic carbon nanotube growth is, however, still not clearly understood, and

¹Queries at the Web of Science (<http://www.isiknowledge.com>) showed that the following numbers of articles have been published on the topic of “‘chemical vapo*r deposition’ AND ‘carbon nanotube*’”, in the publication years given in parentheses: 275 (2002), 398 (2003), 440 (2004), 489 (2005), and 608 (2006). The topics “‘arc discharge’ AND ‘carbon nanotube*’” and “‘laser ablation’ AND ‘carbon nanotube*’” returned 360 and 199 publications, respectively, for the whole 5-year period. The majority of the counted publications are concerned with aspects other than the growth process, but the numbers are arguably good reflections of the availability and the popularity of CVD-grown CNTs.

the exact role of the catalyst is a topic of intensive study [53]. CVD-grown carbon nanotubes are in general structurally inferior to those made by arc-discharge evaporation or laser ablation, and a better understanding of the growth mechanism is needed to improve the material quality.

Zinc Oxide Nanowire Growth by CVD

Wurtzite zinc oxide nanowires can be grown by exposing gold nanoparticles to zinc vapor at high (900–1000 °C) temperatures [54]. Zinc vapor is provided by carbothermal or hydrogen reduction of zinc oxide powder. Zinc atoms dissolve into the liquid gold nanoparticle, and upon supersaturation precipitate out in the form of zinc oxide, due to the reaction with carbon monoxide (CO) gas and water (H₂O) vapor.

Dispersion in Liquid

Nanotubes or nanowires bound to a support can be used as grown, but they are often suspended in liquid and treated for the removal of catalyst particles and other byproducts (amorphous carbon, in the case of carbon nanotubes), and the separation of bundles into individual nanowires. Sonication, either by an ultrasonic bath or by an ultrasonic finger, is usually necessary when one wants to avoid the use of surfactants. As in the case of colloidal nanoparticles, the problem of surface deposition needs to be solved when preparing to study the individual properties of nanowires.

3.2.3 Solution-Phase Synthesis

Solution-phase synthesis of nanowires is becoming popular due to its scalability and the ability to produce metallic nanowires [47]. The general strategy is similar to that used to produce colloidal nanoparticles: precipitation of constituent atoms by the chemical reduction of precursor molecules in solution. In the case of nanowire synthesis, anisotropic growth can be obtained by adding molecular capping agents that adsorb preferentially to specific crystal faces. The capping agents inhibit the growth of the crystal faces to which they adsorb, thereby promoting the growth of crystal in specific directions.

Vanadium Oxide Nanotube Growth

When a primary amine $C_nH_{2n+1}NH_2$ and water are added to a suspension of vanadium pentoxide (V₂O₅) in ethanol and stirred, vanadium oxide–amine complexes form in solution. After supersaturation, vanadium oxide molecules precipitate out as interconnected pyramids, and the ordering of adsorbed amine molecules organize the pyramids into planes. The planes eventually wrap up to minimize surface energy and become open-ended tubes. Further precipitation elongates these tubes to lengths up to a few tens of micrometers [55].

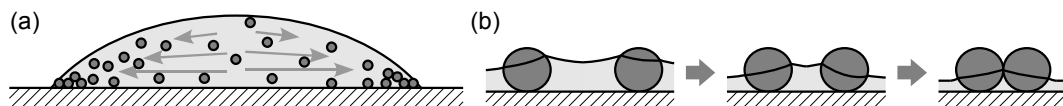


Figure 3.4: (a) Laminar outward flow in a drying drop causes the migration of solute particles towards the contact boundary. (b) Capillary forces pull the deposited particles together at the final drying stage and cause close-packing.

Zinc Oxide Nanowire Growth

Wurtzite zinc oxide nanowires can be grown via the hydrolysis of zinc salts—zinc nitrate $[\text{Zn}(\text{NO}_3)_2]$, for example—in the presence of amines [56]. Amine molecules, hexamethylenetetramine in this case, selectively cap the non-polar crystallographic planes of the zinc oxide crystal, inducing the growth along the wurtzite c axis [57]. Cobalt-doped zinc oxide nanowires have been produced by adding cobalt salts (cobalt acetate) to the process [58].

3.3 Conventional Methods for Dispersed Deposition

To study the properties of single nanoparticles and nanowires, we need place them on solid substrates, with a spacing large enough to resolve individual objects. The acceptable spacing thus depends on the probing method. TEM can resolve very small particles (< 5 nm) even when they are close-packed. In the case of SEM, the lower electron energy and the finite volume of interaction limit the resolution to 1–20 nm. Chemical analysis methods using SEM such as Auger electron spectroscopy (AES) and energy-dispersive X-ray spectroscopy (EDX) also have similar lateral resolutions.

For the AFM, the lateral resolution is mostly determined by the tip size, and it usually falls between 10–50 nm.² AFM derivatives such as electrostatic force microscopy (EFM) and magnetic force microscopy (MFM) typically have lateral resolution above 50 nm. Uniform deposition is another requirement for scanning probe microscopy methods, because the limited image acquisition rate makes it difficult to search for areas of optimal deposition. Hence a uniform deposition of well-separated nanostructures, or the *uniformly dispersed deposition*, is necessary.

But the uniformly dispersed deposition usually cannot be achieved by simply drying a colloid drop on a substrate. Surface asperities and solute particles pin down the contact line, creating a radial outward flow when the solvent evaporates [Fig. 3.4(a)] [59]. The laminar flow drags solute particles outwards and forms a ringlike deposit. And when the solvent layer becomes thinner than the particles, capillary forces pull the deposited particles into a close-packed arrangement [Fig. 3.4(b)] [60]. Different strategies have

²The resolution can be improved by using probes with extremely sharp tips such as the SuperSharpSiliconTM series from NanoSensors, but in most cases it is more cost-efficient and practical to adjust the nanostructure spacing.

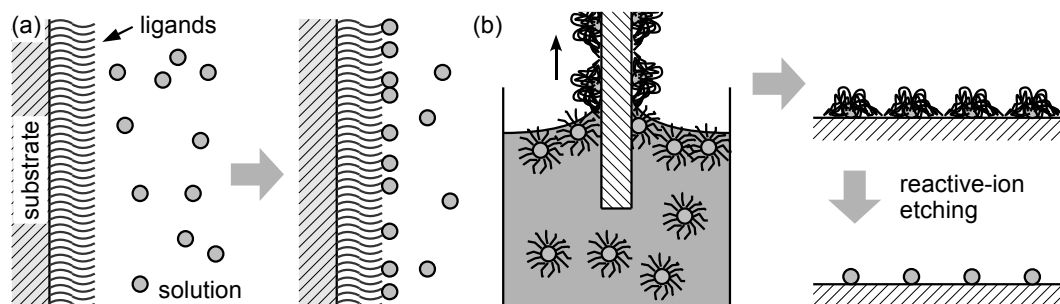


Figure 3.5: (a) A sub-monolayer of nanoparticles can be prepared via self-assembly. (b) A close-packed monolayer of metal-core micelles can be treated to obtain an array of metal nanoparticles.

been proposed to overcome or circumvent these phenomena.

3.3.1 Depositing Nanoparticles

Self-Assembly

Self-assembly is a widely used technique that relies on silanization or dendrimer modification of the sample surface [61]. For particle deposition, the modified substrate is immersed in a colloidal solution for a few hours or days [Fig. 3.5(a)], after which the substrate is taken out and dried. The deposited particles are bound strongly to the modified surface and do not aggregate upon drying. Lithography is possible with various techniques that limit the surface modification to predefined areas [62]. A very uniform deposition with practically no aggregation is possible with stable colloids, but the surface preparation requires a lot of practice, and the method needs to be tailored differently for different substrates and colloids.

Spin Coating

Dispersed deposition through spin coating has been demonstrated for metal nanoparticles [63, 64]. A colloid drop thins down quickly on a spinning sample, so that the solute particles rapidly make contact with the surface and that the solvent evaporates quickly. Once deposited, the particles have a reduced mobility and cannot migrate to the substrate edge before the solvent dries up. As a spin coater is a standard instrument in the semiconductor fab, spin-coating metal catalysts may become a standard step in the industrial CVD growth of nanowires [65]. The results however depend heavily on the solvent viscosity and the surface wettability, parameters that are not always tunable.

Micelle Monolayer Formation and Shell Removal

An ordered array of metal nanoparticles can be obtained by first forming a close-packed monolayer of metal-core block-copolymer micelles on a surface, and then removing the

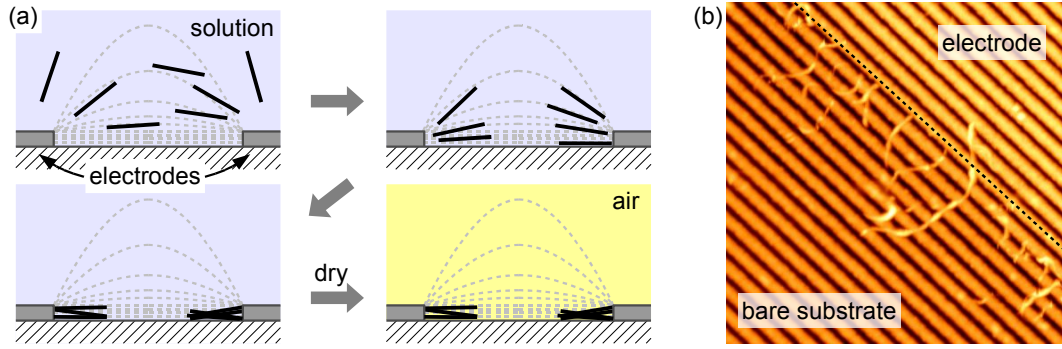


Figure 3.6: (a) Nanowire deposition by ac dielectrophoresis. (b) AFM image of CVD-grown carbon nanotubes deposited by ac dielectrophoresis on a v-groove GaAs substrate.

micelle shells by reactive-ion etching [Fig. 3.5(b)] [66]. A very regular array of nanoparticles can be obtained, and the average spacing can be predetermined by using block copolymers of different molecular weights. Patterning is possible through electron-beam lithography [67]. But the choice of material is limited, as the metal core synthesis is linked with the micelle formation.

Pattern-Guided Dewetting

Dewetting nanoparticles on patterned surfaces has given promising results [68]. Micro-fabricated pits and grooves act as “traps” for nanoparticles and prevent aggregation. This method is well-suited for integrating nanoparticles into the conventional micro-fabrication technology. The cost of micro-fabrication, however, makes the method less suitable for the general scientific research.

3.3.2 Depositing Nanowires

Filtering

Porous substrates can be used to filter out nanowires from suspensions. For example, polished alumina membranes have been used to filter out carbon nanotubes from ethanol suspensions [69]. Sucking the solvent through a membrane with sub-micrometer pores (1) forces the nanotubes to make stable contacts with the substrate, and (2) accelerates the solvent evaporation rate. This technique is especially effective when only a dilute suspension can be prepared. But polishing the porous substrates to a sub-nanometer roughness requires professional expertise.

AC Dielectrophoresis

Alternating-current (ac) dielectrophoresis is another effective method for depositing nanowires from dilute suspensions. If an ac voltage is applied between two electrodes

prepared on a substrate, the nonlinear ac electric field attracts nanowires to the electrodes (Fig. 3.6) [70]. It is the intrinsic or/and the induced dipole moment of nanowires or nanowire-ion complexes in solution that interact with the electric field. An insulating substrate and an insulating solvent are necessary for this technique to be successful.

3.4 Boil Deposition

In the course of this thesis, a novel technique was developed for the uniformly dispersed deposition of colloidal nanoparticles and nanowires [33]. The development was motivated by our dissatisfaction with conventional techniques for the nanoparticle deposition. Self-assembly required too much attention and expertise, as well as limiting the application to only a few kinds of substrates. Spin coating generally did not yield acceptable results. A new technique was invented by reconsidering the basic issues related the drying colloid drop.

As explained in the beginning of Section 3.3, simple dry deposition cannot be used for the nanoparticle and nanowire colloids. The laminar flow and the capillary forces developing inside a drying colloid drop lead to aggregation. *But what if the colloid drop boils on the surface?* Turbulence from nucleate or transient boiling would destroy any continuous laminar flow. The solvent may evaporate away rapidly before the particles aggregate, as the particle mobility after deposition is limited by friction. Intuitively, boiling appeared to be a possible route to the dispersed deposition. The feasibility of “boil deposition” was tested by boiling colloid drops of various nanoparticles and nanowires on different substrates.

3.4.1 Experiment

Nanoparticles

Gold (40 and 50 nm) and silver (20 nm) colloids from British Biocell International, and polystyrene (110 nm) nanoparticle colloid from Bang Labs were diluted 10–1000 times in ultra-pure water from Millipore Simplicity 185 or ethanol (99.9%; Merck).

Nanowires

Vanadium oxide (VO_x) nanotubes were synthesized by a solution-phase process [55] and diluted in cyclohexane. Potassium niobate (KNbO_3) nanowires, also prepared by a solution-phase process [71], were first dried and then sonicated in ethanol. Zinc oxide (ZnO) nanowires were grown by CVD [54] and suspended in ethanol by sonication. Carbon nanotubes were produced by arc-discharge evaporation and sonicated in water using sodium dodecyl sulfate (SDS) as the surfactant [72].

3 Preparation of Surface-Bound Nanostructures

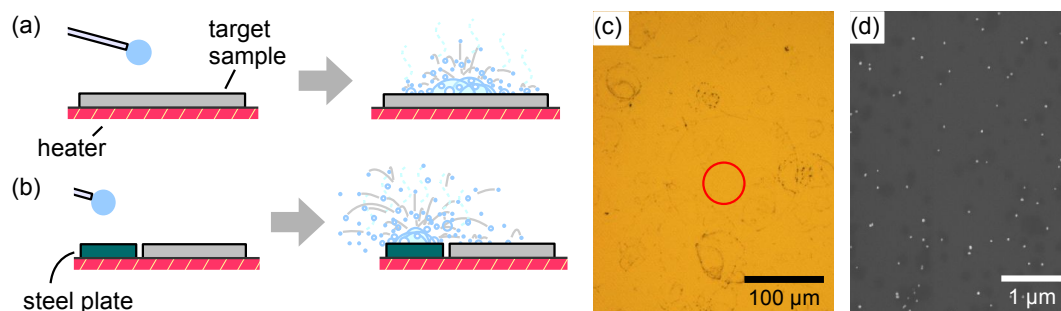


Figure 3.7: (a) Colloid drops were normally boiled directly on the substrate. (b) For a substrate of low thermal conductivity, colloid drops were boiled on an adjacent steel plate. (c) Optical microscopy showed complex patterns on a surface, related to the microdrops created by boiling. Optically “clean” areas, such as the region inside the red circle, revealed dispersed deposits when studied with SEM and AFM.

Substrates

Cut or cleaved pieces (typically $1\text{ cm} \times 1\text{ cm}$) of silicon wafer (with native oxide layer, $1\text{ }\mu\text{m}$ silicon nitride layer, or 50 nm gold layer), gallium arsenide (GaAs) wafer, soda-lime glass coverslip, and muscovite mica were used as substrates. Mirror-polished steel disks (5 mm wide and 3 mm thick) were also used. All substrates except for the mica were cleaned by 10 minutes of ultrasonic bath in deionized water, 10 minutes of ultrasonic bath in ethanol, and 10 minutes of plasma cleaning (Harrick Plasma) using air at 0.5 mbar .

Apparatus

A hot plate with a closed-loop temperature control (PMC Dataplate 730) was used as the heating stage. Substrates were fixed on the stage using a spring clip. To deposit colloid drops, syringes with metal needles were used.³

Procedures

After mounting a substrate, the temperature was raised to $100\text{--}300\text{ }^{\circ}\text{C}$. The optimum temperature varied with the substrate and the colloid solvent (Table 3.1). Once the temperature stabilized, a few $2\text{--}3\text{ mm}$ ($4\text{--}15\text{ }\mu\text{L}$) drops of colloid were placed directly on the heated substrate and left to boil. On substrates with low thermal conductivity such as GaAs, glass and mica, boiling often ceased mid-way due to the limited heat transfer rate. *Indirect* boiling was carried out on these substrates. Colloid drops were boiled on a metal plate placed adjacent to the substrate, and the deposition was achieved through microdrops ($20\text{--}100\text{ }\mu\text{m}$; $4\text{--}500\text{ pl}$) ejected from the main boiling drop. Both the direct and the indirect methods are illustrated in Fig. 3.7(a) and (b).

³Micropipettes could not be used because their plastic tips melted upon approaching a hot surface.

Table 3.1: Heater temperatures for different substrates and colloids.

<i>Substrates</i>	<i>Boiling Method</i>	<i>Colloid in Water</i>	<i>Colloid in Ethanol</i>
Si wafer	Direct	150–200 °C	100–160 °C
GaAs wafer	Indirect	140–190 °C	90–150 °C
Mica	Indirect		150–250 °C
Polished steel	Direct	140–190 °C	90–150 °C

3.4.2 Results

The surfaces were then studied by optical microscopy, atomic force microscopy, and scanning electron microscopy. Under an optical microscope, partial contact-line deposits from microdrops were visible [Fig. 3.7(c)]. Regions that looked “clean” showed dispersed deposition of nanoparticles and nanowires when studied with AFM and SEM. AFM images of dispersed gold nanoparticles on 3 different substrates, silver nanoparticles on cleaved mica, and polystyrene beads on gold layer are shown in Fig. 3.8. The deposition was generally uniform throughout a substrate, and its density depended on the concentration and the volume of colloid used. Occasionally, aggregates of two or several particles were present, but the majority were single particles. For particles larger than 20 nm, single particles were easily distinguishable from aggregates with AFM and SEM.

Deposits of vanadium oxide nanotubes, potassium niobate nanowires, carbon nanotubes, and zinc oxide nanowires are shown in Fig. 3.9. Obtaining a high-quality deposition was more difficult with nanowires mainly due to two reasons: (1) various byproducts of the nanowire syntheses were deposited along with the nanowires, and (2) the nanowire colloids were often not stable enough to reach suitably high concentrations. For the vanadium oxide nanotubes, amine micelles were co-deposited and posed problems for the AFM and SEM imaging. Amine could be removed by rinsing the sample with hydrochloric (HCl) acid, but as vanadium oxide nanotubes themselves use amine molecules in the structure, acid treatment led to a partial dissolution and unwrapping of the nanotubes. Nonetheless, the deposition itself was uniform and well-dispersed [Figs. 3.9(a) and (b)]. Potassium niobate nanowires agglomerated quickly after sonication due to their large intrinsic dipole moments, and the deposition consequently suffered from a high number of aggregates [Figure 3.9(c)]. But a good number of individual wires are also present. For carbon nanotubes, which were invisible under SEM, SDS micelles and films caused serious problems for AFM imaging. An error-signal image is shown instead of a topography image [Fig. 3.9(d)]. Zinc oxide nanowires gave the best results [Figure 3.9(d)].

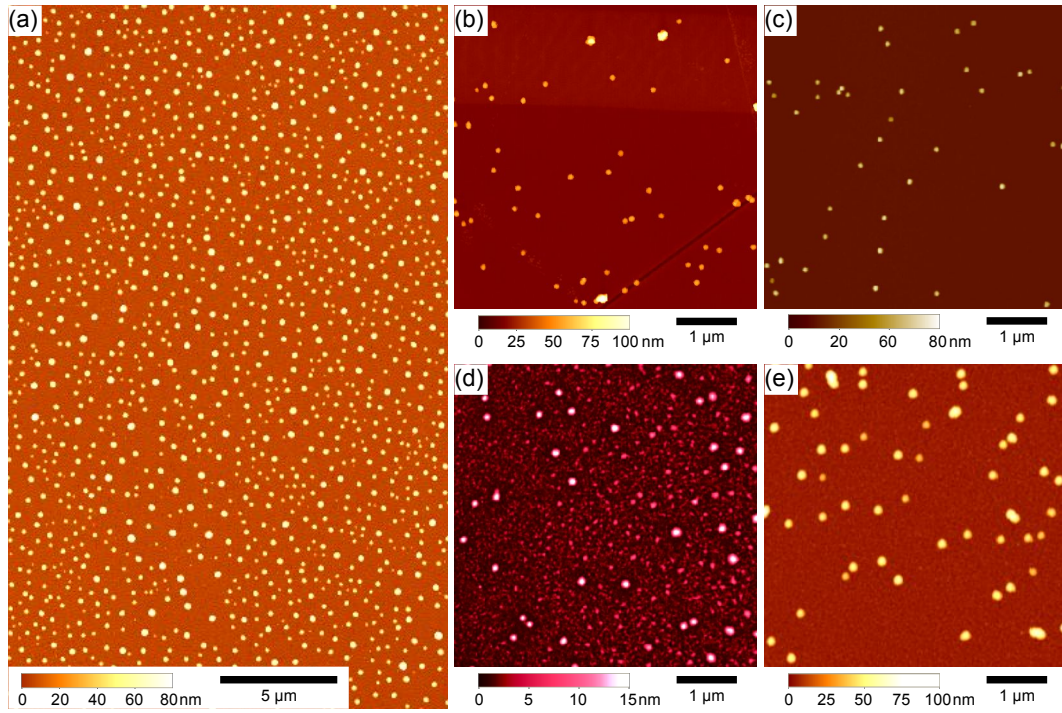


Figure 3.8: AFM images of (a) 40 nm gold nanoparticles on Si (water as solvent; direct boiling; heater at 180 °C), (b) 50 nm gold nanoparticles on polished steel (water; direct; 190 °C), (c) 50 nm gold nanoparticles on GaAs (water; indirect; 170 °C), (d) 20 nm silver nanoparticles on mica (ethanol; indirect; 160 °C), and (e) 110 nm polystyrene nanoparticles on gold layer (ethanol; direct; 120 °C)

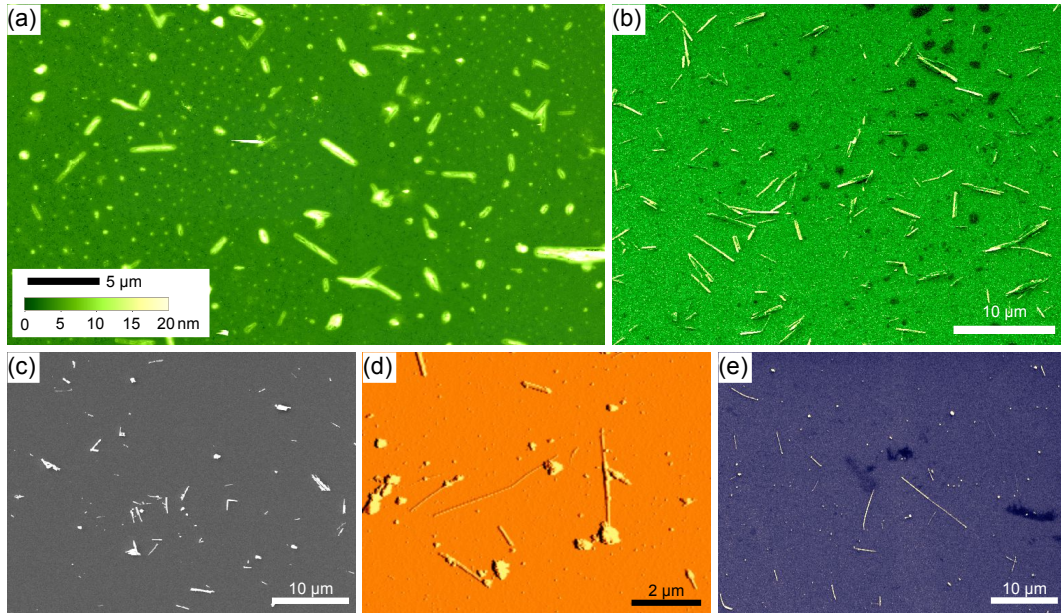


Figure 3.9: (a) AFM image of VO_x nanotubes on Au layer on Si wafer (cyclohexane; direct; 230°C). The sample was cleaned with HCl acid prior to AFM imaging. (b) SEM image of the same sample before the acid treatment. (c) SEM image of KNbO_3 nanowires on Si wafer (ethanol; direct; 140°C). (d) AFM error-signal image of CNTs on Si wafer (ethanol; direct; 90°C). The CNTs were $\sim 10\text{ nm}$ thick. (e) SEM image of ZnO nanowires on Si wafer (ethanol; direct; 140°C).

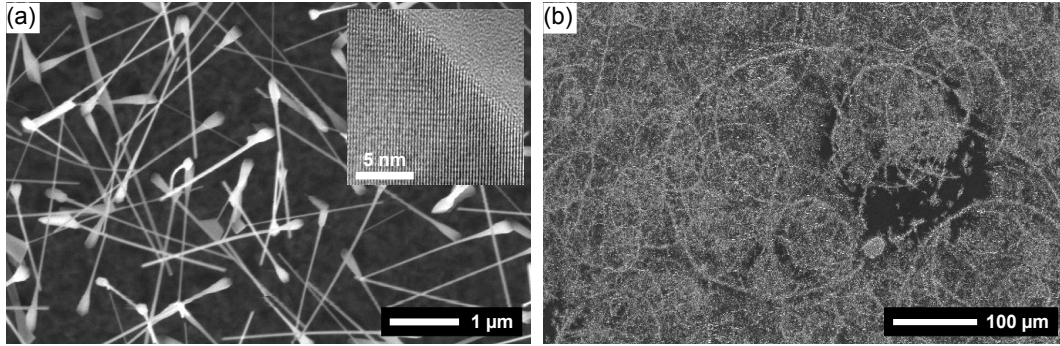


Figure 3.10: ZnO nanowires could be grown from 50 nm gold nanoparticles boil-deposited on a Si wafer. (a) A high-magnification SEM image shows nanowires originating from individual nanoparticles. As the representative TEM image (inset) shows, the nanowires were single crystalline. (b) A low-magnification SEM image of ZnO nanowires gives an enhanced view of the gold nanoparticle deposit patterns.

3.4.3 Discussion

Mechanism

The optimum temperatures for successful deposition could be found easily, but the complexity of liquid-drop dynamics on a hot surface [73, 74] made it difficult to understand the deposition mechanism. But SEM images of zinc oxide nanowires grown by CVD from boil-deposited gold nanoparticles offered a valuable insight. As can be seen in the high-magnification SEM image [Fig. 3.10(a)], single-crystalline nanowires originated from individual gold nanoparticles. As-grown zinc oxide nanowires gave high-contrast SEM images even at low magnifications, as opposed to the gold nanoparticles that were practically invisible at such scales. The low-magnification zinc oxide-nanowire images highlighted various patterns in the gold-nanoparticle deposit, and showed it to be a superposition of microdrop deposits [Fig. 3.10(b)]. Hence we were led to consider if the actual deposition occurred through microdrops.

The microdrop deposition model was supported by additional observations. A nucleate-boiling drop that ejected and dissociated into microdrops was necessary for a successful deposition. Deposition was unsuccessful with rapidly drying or film-boiling (buoying on its own vapor) drops that did not eject microdrops. Upon monitoring the process with an optical microscope, we also learned that the microdrops must wet the surface. If a substrate was so hot that the microdrops slid off without wetting (Leidenfrost effect [75]), dispersed deposition did not occur. As microdrops drying at the room temperature were known to leave behind ringlike deposits like larger drops [76], questions remained as to how they behave on hot surfaces.

Using an ink-jet printing system (Microdrop MD-K-130), individual 20 pL (30–40 μm) microdrops of 50 nm gold colloid were deposited on silicon wafer at different temper-

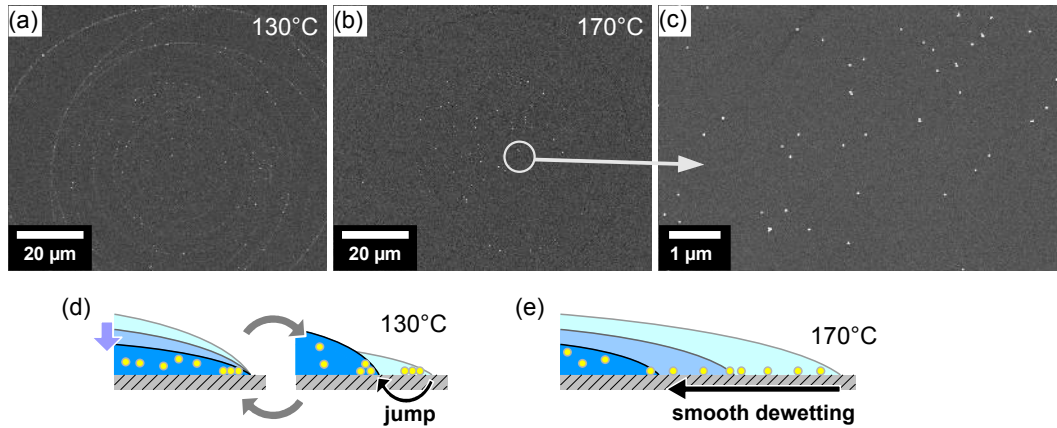


Figure 3.11: SEM images of (a) the deposit from a 20 pL gold colloid microdrop on a Si wafer when heater was at 130 °C, and (b) the deposit from a similar drop when the heater was at 170 °C. (c) The 170 °C deposit showed a dispersed deposition. A microdrop may evaporate through either (d) a series of contact-line jumps or (e) smooth dewetting, depending on the substrate temperature.

atures (110–170 °C). At these temperatures, a microdrop does not boil because the evaporation time is too short [73]. Concentric ringlike deposits were left by single microdrops evaporating at low temperatures (110–130 °C) [Fig. 3.11(a)], but uniformly dispersed deposits were obtained for higher temperatures (150–170 °C) [Fig. 3.11(b) and (c)]. A competition between self-pinning and dewetting is known to cause the contact line to jump [77], and a microdrop in such a state would leave behind concentric deposits [Fig. 3.11(d)]. But at sufficiently high temperatures, a microdrop seems to dewet smoothly, possibly because of heating-related contact-line perturbations that prevent self-pinning [Fig. 3.11(e)]. These results support a two-step mechanism for the boil deposition: (1) a millimeter-sized drop ejects and finally dissociates into microdrops, and (2) the microdrops dewet smoothly when evaporating, resulting in the dispersed deposition of solute particles.

Advantages

Boil deposition proved to be more convenient and efficient than conventional methods such as self-assembly and spin-coating. In self-assembly, surface functionalization is a crucial step that requires scrupulous cleaning and handling of substrates, and the procedures vary significantly for different materials [61]. In boil deposition, bare substrates can be used, and basic cleaning procedures are often sufficient. The method can be applied to different substrates and colloids with little or no change in the details. And while self-assembly typically takes a few hours to a few days, boil deposition can be carried out in a few minutes. For the zinc oxide nanowire growth by CVD, our group had previously relied on a self-assembly method, but now we only use the boil

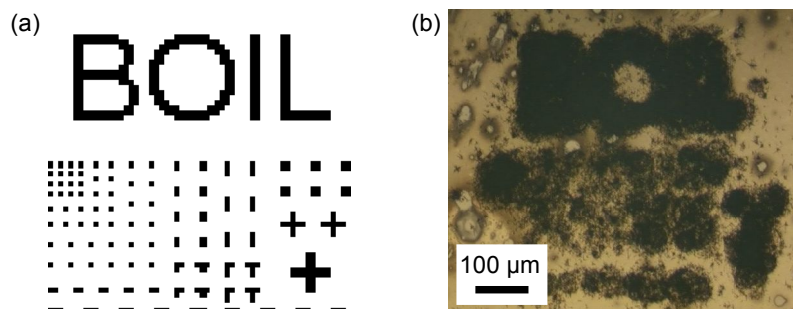


Figure 3.12: (a) Designated pattern for ink-jet boil deposition. (b) Optical image of ZnO nanowires grown on boil-deposited gold nanoparticles.

deposition technique. Boil deposition allows a faster preparation with significantly less effort. Compared to spin coating, we found boil deposition to give better results with fewer aggregates, and the results were less sensitive to the solvent viscosity.

3.5 Conclusions and Outlook

We have reviewed the general strategies for synthesizing various nanostructures, and summarized the techniques that are used to prepare dispersed surface depositions. A novel technique named “boil deposition” was invented in the course of this thesis, and the method as well as the deposition mechanism have been explained in detail.

Boiling leads to the uniformly dispersed deposition of colloidal nanoparticles and nanowires. The method is simple and efficient, and it can be applied to a wide range of colloids and surfaces. The deposition seems to occur through microdrops (created during the boiling of millimeter-sized drops) that dewet smoothly at elevated temperatures and leave behind uniformly surface-dispersed solute particles. The mechanism should be studied in greater detail in future by using a high-speed imaging system customized for observing microdrops, such as the one reported by Kim et al. [74].

Preliminary experiments, where “boil lithography” was performed by ink-jet printing on hot substrates, gave promising results. The substrate was displaced by a stepper motor x-y stage. A 50 μm pattern-width could be achieved, and a dense array of zinc oxide nanowires could be grown by CVD on the patterned substrate (Fig. 3.12). A 20 μm pattern-width should be possible by optimizing the microdrop size and the deposition temperature.

4 Mechanical Properties of Surface-Bound Nanowires

Surface-bound carbon nanotubes and semiconductor nanowires are promising components in the bottom-up approach to the nanometer-scale electronics. Mechanical stresses and the related failures are becoming increasingly important in the fabrication and operation of electronic devices, as the integrated circuits are being scaled down to the physical limit. A good understanding of the mechanical properties is therefore a prerequisite to the realization of nanowire electronics. Different approaches to measuring the elastic modulus of nanotubes are introduced, and the existing data on carbon nanotubes are summarized. A novel phenomenon, the diameter-dependent Young's modulus of CVD-grown multiwall carbon nanotubes, is reported [78]. The diameter dependence is a strong evidence for the metastable-catalyst model of carbon nanotube growth by CVD.

4.1 Carbon Nanotube Applications in Microelectronics

After the discovery of single-wall carbon nanotubes (SWCNTs) [6], it was shown that a SWCNT can be either conducting, semiconducting, or insulating depending on its chirality (Fig. 4.1) [79]. A semiconducting or conducting carbon nanotube exhibits ballistic transport along its length, and an extremely high current density (10^9 A/cm²) is possible. Such novel properties have led scientists to investigate if carbon nanotubes can be employed to realize nanometer-scale electronics [80].

4.1.1 Recent Trends in Silicon Technology

The crucial component of modern-day electronics is the microchip, which is an integrated circuit (IC) of miniaturized electrical components such as transistors, diodes, resistors, and capacitors fabricated directly on a substrate using the VLSI (Very-large-scale integration) silicon technology [4]. The strategy is to first create the components—most notably transistors [Fig. 4.2(a)]—directly on the silicon wafer (*device fabrication*), and then to build a circuit by forming metal interconnects on top [*metallization*; Fig. 4.3(a)].

For the past 50 years, the microelectronics industry has followed Moore's law faithfully, doubling the number of transistors per chip every two years. But simple scaling is becoming less and less probable, and new materials are now necessary to increase both

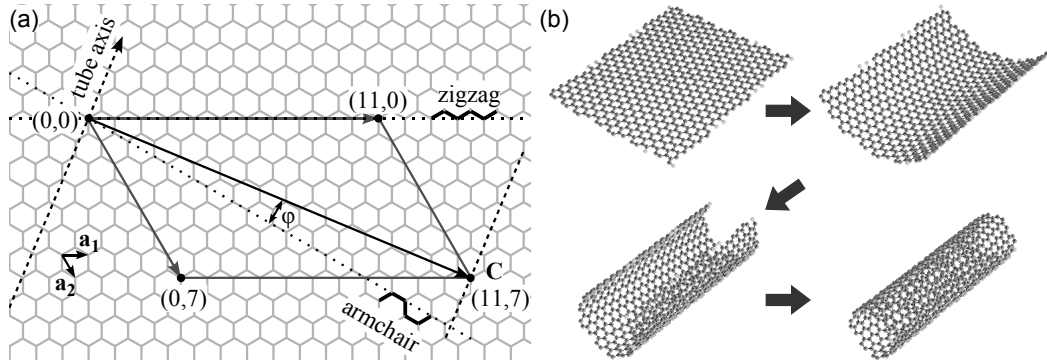


Figure 4.1: Relation between the hexagonal graphite lattice and the chirality of a single-wall carbon nanotube. (a) By rolling up a single graphene sheet along the wrapping vector C , a nanotube indicated by the indices $(11,7)$ is formed. The wrapping angle ϕ is defined with respect to the armchair direction. (b) Computer-generated animation of a $(11,7)$ nanotube wrapping. The animation helps to explain the structure of a carbon nanotube, but it is not a depiction of the actual growth process.

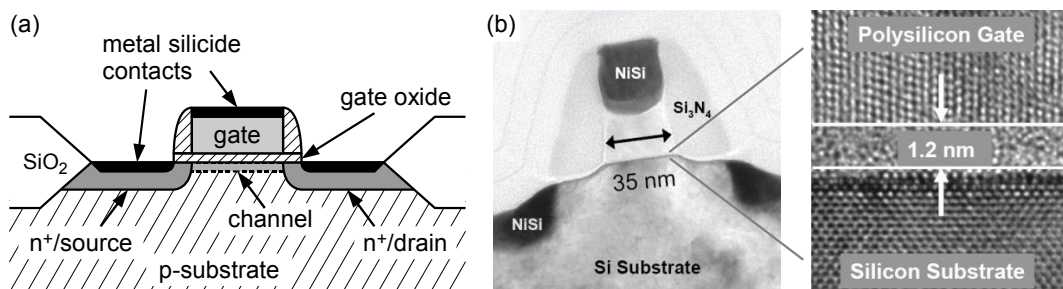


Figure 4.2: (a) Simplified schematic of a n-type metal-oxide-semiconductor field-effect transistor (MOSFET). (b) Cross section of a MOSFET produced by Intel's 65 nm process. The source and drain contacts are 65 nm apart, the gate 35 nm wide, and the gate oxide 1.2 nm thick.

the device density and performance [81]. For example, Intel's 65 nm process produces a 65 nm-source-drain-gap MOSFET with polysilicon gate and silicon dioxide (SiO_2) gate oxide [Fig. 4.2(b)]. When scaling down the source-drain gap to 45 nm, Intel switched to metal gate and hafnium-based high-dielectric-constant (high- κ) gate oxide, in order to address the issues of depletion effect at the gate-gate oxide interface and gate-channel leakage current[82].

Similar progresses have been made in the metallization process. The industry is increasingly moving away from the well-established Al/ SiO_2 process—aluminum interconnects separated by silicon dioxide interlayer dielectric (ILD; dielectric layer between metal layers)—toward the Cu/low- κ process—copper interconnects separated by ILD of lower dielectric constant [83]. The higher electrical conductivity of copper and the lower ILD dielectric constant allow thinner interconnects to be placed closer together, with a tolerable RC (resistance \times capacitance) delay. The minimum line width of interconnects is limited by the effect of electromigration. With a thin metal interconnect, high current density can cause the migration of atoms along the direction of current flow.¹ Excessive migration of atoms result in void formation, eventually leading to device failure [83].

4.1.2 Carbon Nanotube Interconnects

A proposed solution for achieving higher interconnect density without sacrificing reliability is to use carbon nanotubes as the wiring material [84]. As multiwall carbon nanotubes can be grown vertically using a chemical vapor deposition (CVD) process, a number of semiconductor companies—among whom Fujitsu has been the most active in disclosing the progress [86, 87, 84, 85]—are investigating if nanotubes can be used as vias between metal layers [Fig. 4.3(b)]. Initial efforts reported high electrical resistance due to poor metal–nanotube contact and low nanotube density, but the latest damascene process depicted in Fig. 4.3(c) gives $0.05\ \Omega$ electrical resistance for 60 nm-high and $2.8\ \mu\text{m}$ -wide vias [85]. This value is still higher than what is achievable with copper vias, but it is lower than the resistance of tungsten vias used in the Al/ SiO_2 process. Further reduction in contact resistance would become possible with a better understanding of the carbon nanotube growth mechanism in CVD. As the carbon nanotube vias can withstand higher current density and suffer less from electromigration, they may soon replace copper vias in applications where the interconnect density is critical.

4.1.3 Carbon Nanotube Transistors

In the current planar CMOS transistor design [Fig. 4.2(a)], reducing the gate length also reduces the barrier height at the source, leading to a large leakage current in the off

¹The current density in a thin metal film line $0.5\ \mu\text{m}$ wide and $0.2\ \mu\text{m}$ thick carrying 1 mA will be $10^6\ \text{A}/\text{cm}^2$.

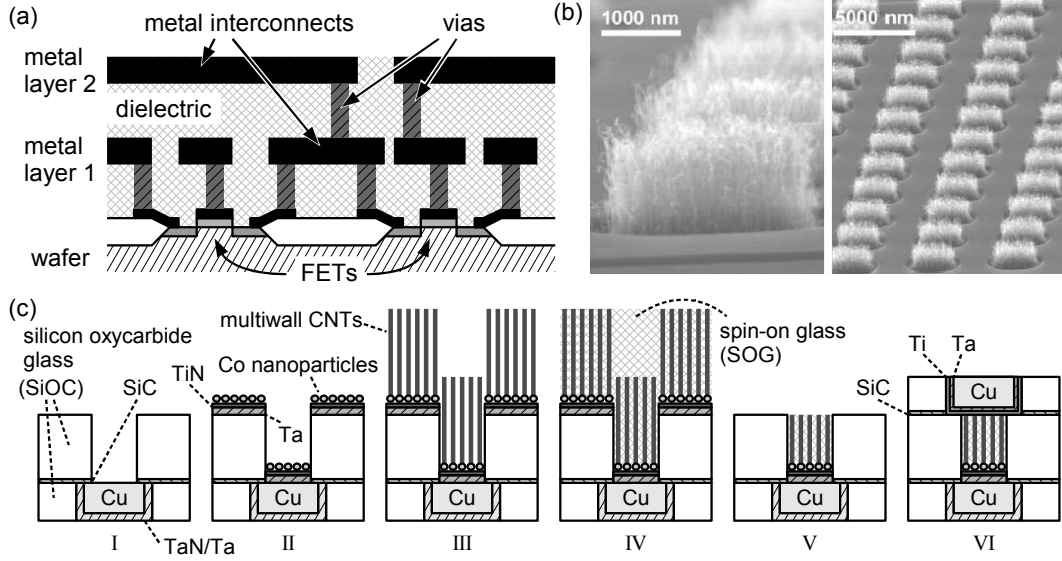


Figure 4.3: (a) A circuit of FETs created by double-layer metallization. (b) SEM images of carbon nanotube via array [84]. (c) CNT damascene process using Co catalyst nanoparticles that gives the lowest reported electrical resistance [85]. I: via hole formation on bottom Cu wire; II: TaN/Ta barrier layer, TiN contact layer, and Co catalyst nanoparticle formation; III: multiwall CNT growth all over the substrate; IV: SOG coating; V: CMP planarization; VI: top Cu wire formation.

state [81]. Due to this *degraded short channel effect (SCE)*, the practical gate length is limited to ~ 20 nm. To overcome this limit in scaling, researchers are testing alternative technologies, and there are efforts to replace the source–drain–channel structure with a carbon nanotube [88]. The bandgap of a semiconducting nanotube is given by $E_{gap} = 2\gamma_o a_{cc}/D$, where E_{gap} is the bandgap, γ_o is the carbon-to-carbon tight-binding overlap energy, a_{cc} is the nearest-neighbor carbon-to-carbon distance (0.142 nm), and D is the nanotube diameter.

At the moment carbon nanotube transistors suffer from serious problems such as the high metal–nanotube contact resistance, the inability to control nanotube chirality, and the difficulty in large-scale assembly or growth [80]. But progresses are being made consistently. For example, a recent work demonstrated that single-walled carbon nanotubes of specific chirality can be separated out using fluorene-based polymers that exhibit selective wrapping properties [89].

4.1.4 Mechanical Stresses in IC Fabrication and Operation

IC fabrication processes that involve material deposition, heating/cooling, polishing, and wire bonding can introduce significant mechanical stresses to the IC structure [90]. Electromigration can generate additional stresses at IC operation. These stresses may cause local damages in material, degrading the circuit performance. In severe cases,

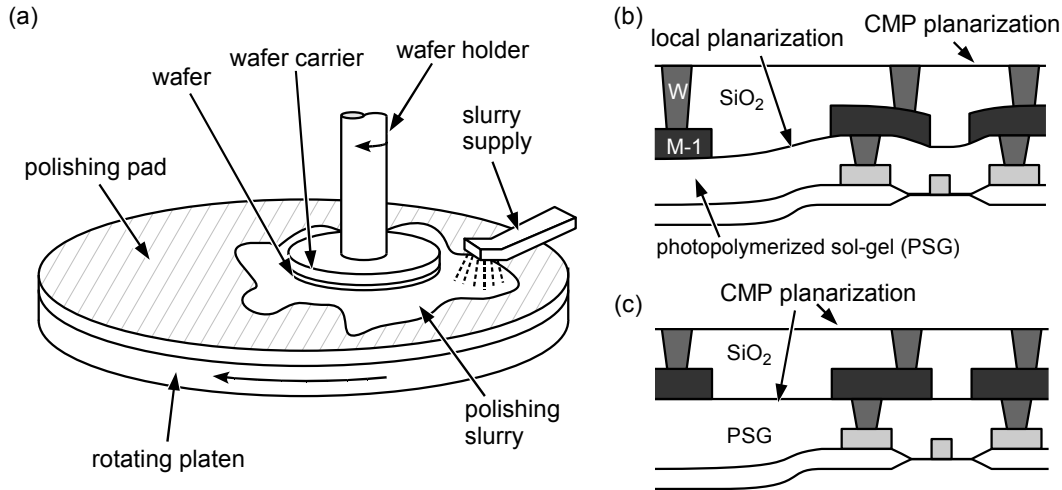


Figure 4.4: (a) Schematic of a chemical–mechanical polisher. Different planarization approaches lead to differences in via depth: (b) Interlayer dielectric (ILD) vias can have different depths if local planarization precedes CMP planarization; (c) ILD vias have similar depths when CMP is used twice.

the mechanical stresses may cause cracks or drive preexisting cracks to grow, leading to a circuit failure.

Shear Stresses in Chemical–Mechanical Polishing

Chemical–mechanical polishing (CMP) is used for the global polishing (or *planarization*) of the silicon wafer at various stages of the IC fabrication [4]. The wafer is polished against a polishing pad using a slurry, usually colloidal silica suspended in a potassium hydroxide (KOH) solution [Fig. 4.4(a)]. Both the polishing pad platen and the wafer holder rotates, resulting in a uniform polishing of the wafer.

As the number of metal layers increases,² it becomes important to perform global planarization on all layers including the poly–metal dielectric (PMD; dielectric covering the device layer) [Fig. 4.4(b) and (c)]. CMP processes must be optimized for each surface material—the PMD and the ILDs have different chemical and mechanical characteristics, and the vias have a different polishing rate [4]. In addition, the parameters such as CMP pressure and slurry material must be chosen carefully as to preserve the structural integrity of the underlying structure as well as its constituent elements. The shear stress generated during a CMP process can be destructive. It has been observed that the mechanical polishing of carbon nanotube vias can damage the nanotubes [87]. Structural damage in carbon nanotubes will inevitably cause a higher electrical resistance.

An integrated circuit is a heterogeneous material structure made of thin and small

²Intel’s 45 nm process for making the latest Core 2 microprocessors uses 9 copper interconnect layers. In contrast, the 0.8 μm BiCMOS process for the first Pentium CPUs involved 2 aluminum interconnect layers.

components. The material properties of constituent elements are becoming increasingly important, as the IC is becoming more and more delicate. Correspondingly, a good understanding of the mechanical properties of carbon nanotubes and other semiconductor nanowires is necessary if these surface-bound nanowires are to be incorporated into the integrated circuit.

4.2 Measuring the Elastic Modulus of a Carbon Nanotube

When characterizing a carbon nanotube mechanically, the nanotube is modeled as a tube or a cylinder of homogeneous and isotropic material. Its Young's modulus is the *effective* value that will give the model structure the same stiffness as the nanotube. Young's modulus is calculated by dividing the tensile stress σ by the tensile strain ϵ . When a tube of length L_{tube} and cross-sectional area A_{tube} elongates by ΔL_{tube} under a tensile load F , the Young's modulus E_{tube} is given by [91]

$$E_{tube} = \frac{\sigma}{\epsilon} = \frac{F/A_{tube}}{\Delta L_{tube}/L_{tube}} = \frac{F L_{tube}}{A_{tube} \Delta L_{tube}}. \quad (4.1)$$

While several researchers have succeeded in performing tensile tests with carbon nanotubes [92, 93], the tensile tests showed a very low throughput due to the difficulty in manipulating carbon nanotubes. Better throughput, which would be necessary for quality control in industrial applications, has been achieved by *bending* tests. Cantilever or clamped-beam structures are prepared with carbon nanotubes, and bending tests are performed by transmission electron microscopy (TEM), field-emission electron microscopy (FEM), or atomic force microscopy (AFM).

4.2.1 Electron Microscopy Methods

Thermal Vibration

Treacy, Ebbesen, and Gibson [94] were the first to measure the mechanical properties of individual carbon nanotubes. Using a transmission electron microscope with a sample heater, they measured the thermal vibration of carbon nanotube cantilevers over a wide temperature range [Fig. 4.5(a) and (b)]. A carbon nanotube cantilever was modeled as a circular beam of isotropic material clamped at one end. For the vibration of n -th resonance mode in the plane of view, the time average of vibration energy W_n (elastic + kinetic) is

$$\langle W_n \rangle = c_n \langle u_n^2 \rangle, \quad (4.2)$$

where u_n is the instantaneous tip deflection due to the n -th mode, and c_n is the effective spring constant given by

$$c_n = \frac{\pi \beta_n^4 E_{tube} (D^4 - D_i^4)}{256 L_{tube}^3}. \quad (4.3)$$

4.2 Measuring the Elastic Modulus of a Carbon Nanotube

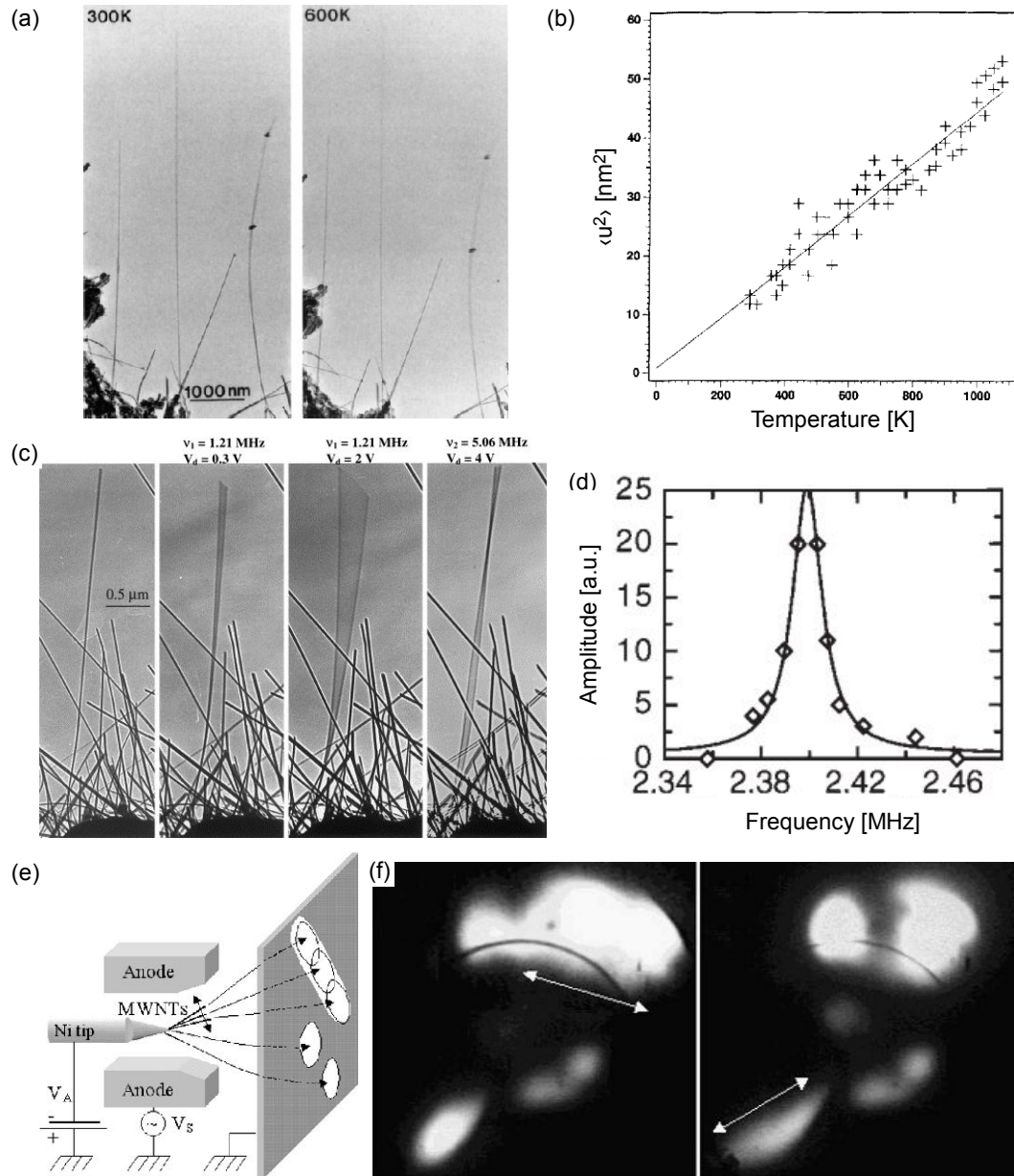


Figure 4.5: In the method reported by Treacy et al. [94], (a) the vibration of a carbon nanotube cantilever is observed by TEM, and (b) the temperature is varied. Poncharal et al. [95] (c) excited the nanotube cantilever using an ac external field, and (d) observed the dynamic response by sweeping the frequency. Purcell et al. [96] (e) used the field emission of electrons, (f) observing the patterns on the detection screen to find the resonance frequencies.

β_n is the n -th solution to $\cos \beta \cosh \beta = -1$ ($\beta_o \approx 1.8751$), E_{tube} is the nanotube's elastic modulus, D and D_i are its outer and inner diameters, respectively, and L_{tube} is the cantilever length.

As there are two degrees of freedom for each vibrational mode, the time average of W_n at temperature T is given by

$$\langle W_n \rangle = k_B T, \quad (4.4)$$

where k_B is the Boltzmann constant. Each mode of a stochastically-driven oscillator has a Gaussian vibration probability profile, with its variance σ_n^2 ($= \langle u_n^2 \rangle$) given by

$$\sigma_n^2 = \frac{k_B T}{c_n} \quad (4.5)$$

The sum of Gaussian-profile vibrational modes also has a Gaussian distribution, with its variance σ^2 equal to the sum of variances of the vibrational modes. By definition, the time average of the square of cantilever deflection $\langle u^2 \rangle$ is equal to σ^2 , and therefore

$$\langle u^2 \rangle = k_B T \sum \frac{1}{c_n} = \frac{256 L_{tube}^3 k_B T}{\pi E_{tube} (D^4 - D_i^4)} \sum \frac{1}{\beta_n^4} \approx 0.02652 \frac{L_{tube}^3 k_B T}{E_{tube} (D^4 - D_i^4)}. \quad (4.6)$$

$\langle u^2 \rangle$ is measured from the TEM images [Fig. 4.5(a)]. The electron beam adds some energy to the nanotube cantilever, raising its temperature, so that Eq. 4.6 is not used directly, but instead the temperature T is varied and E_{tube} is calculated from the slope of the T - $\langle u^2 \rangle$ graph [Fig. 4.5(b)]. The main uncertainty comes from the $\langle u^2 \rangle$ measurement; focusing is difficult yet required after each change in temperature.

Electrostatic Excitation

Poncharal et al. [95] modified Treacy's method by driving the carbon nanotube cantilevers with an alternating current (ac) electrostatic field [Fig. 4.5(c)]. Carbon nanotubes were mounted on an electrode whose voltage could be controlled with respect to a grounded counter electrode tens of micrometers apart. The electric field induces an electrostatic charge on a nanotube, which is concentrated at its tip. The resonance frequency and its harmonics can be found by sweeping the ac voltage frequency [Fig. 4.5(d)]. The nanotube is modeled as in the thermal vibration method, in which case the angular resonance frequencies ω_n are related to the material and structural properties by

$$\omega_n = \frac{\beta_n^2 \sqrt{D^2 + D_i^2}}{4 L_{tube}^2} \sqrt{\frac{E_{tube}}{\rho}}. \quad (4.7)$$

ρ is the material density, for which the value of graphite (2250 kg/m³) is used.

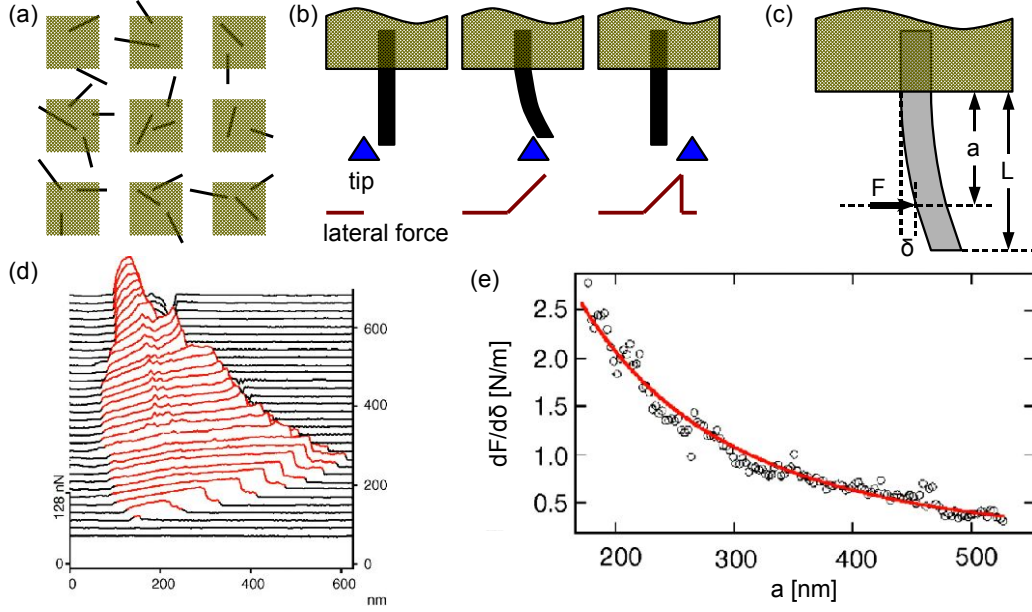


Figure 4.6: (a) For the lateral deflection measurement of carbon nanotubes, carbon nanotubes are first deposited on a substrate and then fixed by square SiO pads. (b) A nanotube clamped at one end is deflected laterally by a passing AFM tip, until the tip loses contact and the nanotube restores its original form. (c) In addition to the force applied by the AFM tip, there is a friction force opposing the deflection. (d) Lateral deflection signals at different a positions are plotted in three dimensions. (e) The nanotube spring constant k_{tube} is inversely proportional to a^3 .

Field-Emission Electron Microscopy

The setup used by Purcell et al. [96] is similar to Poncharal's, but the amplitude detection was improved by using the field emission of electrons [Fig. 4.5(e) and (f)]. Nanotube vibration is analyzed from the pattern on the detection screen, which allows a more reliable amplitude measurement than the TEM observation.

4.2.2 Atomic Force Microscopy Methods

Lateral Deflection

The first AFM measurement of the carbon nanotube elastic modulus was carried out by Wong, Sheehan, and Lieber [97]. Multiwall carbon nanotubes were ultrasonically dispersed in toluene, and deposited on the surface of a molybdenum disulfide (MoS_2) crystal which gives very low friction. Square silicon oxide (SiO) pads were deposited on top using a shadow mask to fix the nanotubes [Fig. 4.6(a)], and the clamped nanotube cantilevers were deflected laterally during contact AFM imaging [Fig. 4.6(b)]. If a nanotube may be modeled as a cylindrical beam of isotropic material, the following

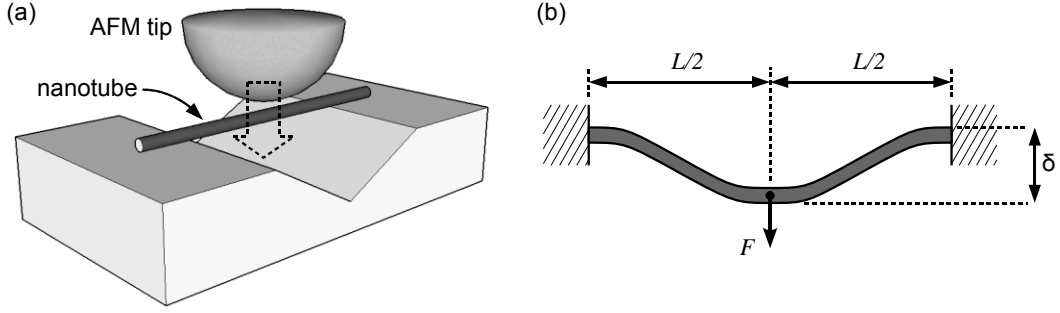


Figure 4.7: The strategy proposed by J.-P. Salvetat et al. [98] (a) A nanotube is prepared over a trench or a hole, and is pressed down in the middle with an AFM tip. (b) The nanotube is modeled as a doubly clamped beam.

equation should hold for the structure illustrated in Fig. 4.6(c):

$$F_{lat} = \frac{3 E_{tube} I_{tube}}{a^3} \delta_{tube}, \quad (4.8)$$

where I_{tube} is the second moment of inertia of the beam ($\pi D^4/64$), and F_{lat} is the lateral force applied by the tip, calculable from the torsional deflection of the AFM cantilever. Lateral deflection signal contains a jump related to the nanotube–tip jump-off-contact [Fig. 4.6(b)], and the F_{lat} and δ_{tube} values for a given position a are calculated at this jump [Fig. 4.6(c)]. The effects of friction can be minimized by plotting the tube spring constant $dF_{lat}/d\delta_{tube}$ ($= 3E_{tube}I_{tube}/a^3$) against a and fitting the data with a 3rd-order polynomial [Fig. 4.6(d)].

The biggest drawback of this method is that the measurement relies on the lateral spring constant of an AFM cantilever, which is an unresolved issue [16, 15] more than 10 years after Wong’s experiment. The relative uncertainty in cantilever lateral spring constant (easily larger than 100 %) translates directly into the uncertainty of the nanotube elastic modulus. Wong et al. may have used the silicon carbide (SiC) nanowires to serve as a reference, as their elastic modulus is not expected to differ significantly from the bulk value.

Normal Deflection

It was Salvetat et al. [98] who reported the first reliable and practical method for the nanotube elastic modulus measurement by AFM. The strategy is to (1) deposit individual carbon nanotubes over holes or trenches, and then (2) to deflect the suspended structures vertically with an AFM cantilever [Fig 4.7(a)]. Once deposited, the adhesion of a nanotube on the substrate is much stronger than the normal force applicable by the AFM cantilever, so that the suspended nanotube is modeled as a doubly clamped beam (suspended length L_{tube}) of circular and uniform cross section (diameter D) [Fig. 4.7(b)]. In this model, the midpoint deflection δ_{tube} and the loading force F_k

4.2 Measuring the Elastic Modulus of a Carbon Nanotube

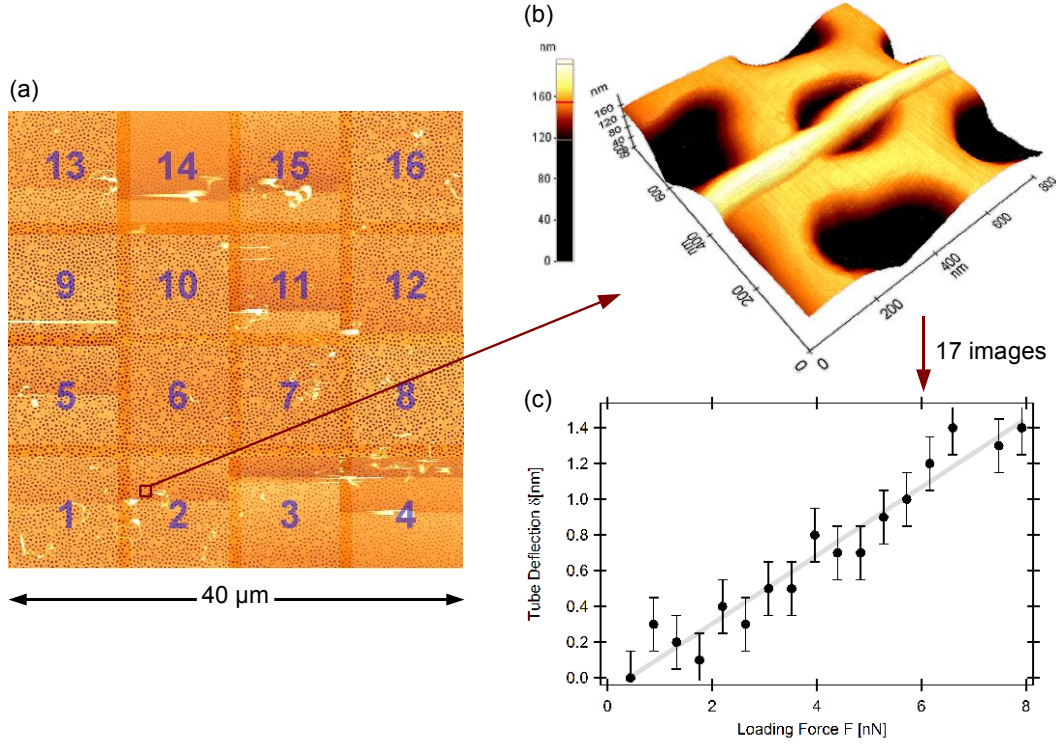


Figure 4.8: (a) A stitched ensemble of AFM images covering the whole x-y scanner range of the AFM, used to locate suspended carbon nanotubes. Images are taken sequentially in the order indicated. (b) 3D rendering of a suspended nanotube. (c) The F_k - δ_{tube} graph gives the nanotube spring constant.

satisfy the following relationship [91].

$$F_k = \frac{192 E_{tube} I_{tube}}{L_{tube}^3} \delta_{tube}, \quad (4.9)$$

where I_{tube} , the second moment of inertia, is $\pi D^4/64$ for a cylinder. The spring constant of the suspended structure k_{tube} is given by

$$k_{tube} = \frac{dF_k}{d\delta_{tube}} = \frac{3 \pi D^4}{L_{tube}^3} E_{tube}. \quad (4.10)$$

L_{tube} and D are measured from an AFM image. The measured nanotube height is used for D , because the AFM tip radius (often larger than D) results in an overestimation of the nanotube width. The elastic modulus E_{tube} can be calculated from Eq. 4.10 if k_{tube} is known.

Salvetat implemented the strategy by using filter deposition (Section 3.3.2) and contact AFM imaging (Section 2.5). Nanotubes are deposited by filtering an ultrasonically dispersed carbon nanotube solution with a polished alumina membrane. Nanotubes that are suspended over alumina pores are found by AFM [Fig. 4.8(a) and (b)], and contact AFM images are taken at different values of setpoint loading force F_k . The

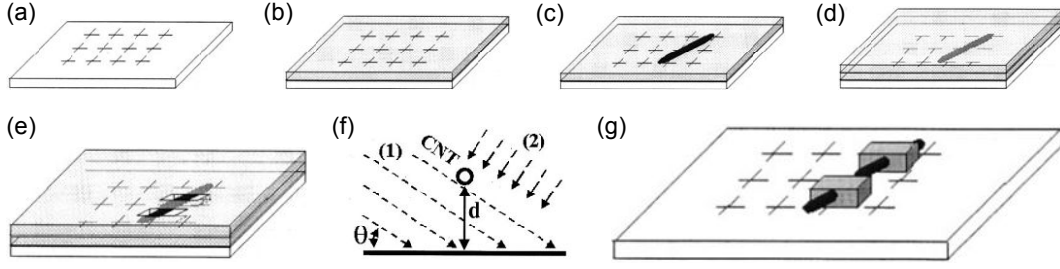


Figure 4.9: Process for preparing suspended carbon nanotubes, as reported by Kim et al. [99] (a) Si wafer with SiO₂ coordinate markers is the substrate. (b) First PMMA layer is spin-coated, (c) followed by the spin coating of carbon nanotube solution. A nanotube is found by AFM and its position is recorded. (d) Two additional PMMA layers are deposited, and (e) then e-beam lithography opens two windows around the nanotube. (f) Metal layer is deposited at two angles, and finally (g) a suspended carbon nanotube structure is obtained by lifting off the PMMA layers.

midpoint deflection δ_{tube} is measured for each image, so that a set of F_k - δ_{tube} data is obtained [Fig. 4.8(c)]. The spring constant of the suspended carbon nanotube k_{tube} is calculated by linear regression of the F_k - δ_{tube} graph.

The relative uncertainty of the E_{tube} calculation is given by

$$\left(\frac{\delta E_{tube}}{E_{tube}}\right)^2 = \left(3 \frac{\delta L_{tube}}{L_{tube}}\right)^2 + \left(4 \frac{\delta D}{D}\right)^2 + \left(\frac{\delta k_{tube}}{k_{tube}}\right)^2. \quad (4.11)$$

$\delta k_{tube}/k_{tube}$ contains uncertainties in cantilever spring constant, z scanner calibration, and F_k - δ_{tube} linear regression. $\delta L_{tube}/L_{tube}$ usually dominates the total error. $\delta L_{tube}/L_{tube}$ is often large (10–15%) because the pore edge beneath the nanotube is not visible in AFM images. A total uncertainty of 50% is realistic for E_{tube} .

Finding a suspended nanotube is time-consuming with Salvétat's method, because AFM imaging is slow. On average 1 nanotube can be found and analyzed per day. Kim et al. [99] proposed a partial solution, in which suspended carbon nanotubes are prepared by lithography. In this method, a silicon substrate with silicon oxide coordinate markers [Fig. 4.9(a)] is first spin-coated with PMMA (poly methylmethacrylate) [Fig. 4.9(b)], and then a carbon nanotube solution is additionally spin-coated on top [Fig. 4.9(c)]. Surface-bound nanotubes are found by AFM imaging, and their positions are recorded relative to the coordinate markers. After depositing additional PMMA layers on top [Fig. 4.9(d)], windows are opened around two points on a nanotube by e-beam lithography [Fig. 4.9(e)], so that metal layers can be deposited around the nanotube at the windows [Fig. 4.9(f)]. Upon lifting off the PMMA layers, a suspended carbon nanotube clamped in metal blocks is obtained [Fig. 4.9(g)]. Kim's method, however, is still time-consuming as the nanotubes are deposited at random and they must be located by AFM.

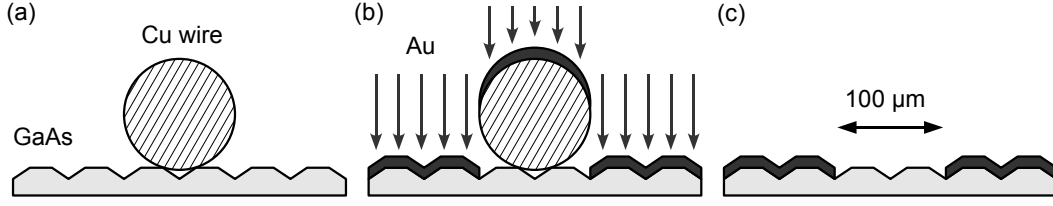


Figure 4.10: (a) A piece of 100 μm-thick copper wire is used as the mask on a v-groove GaAs substrate. (b) Gold is deposited by thermal evaporation, and (c) the copper wire is then lifted off to give a 100 μm gap between the electrodes.

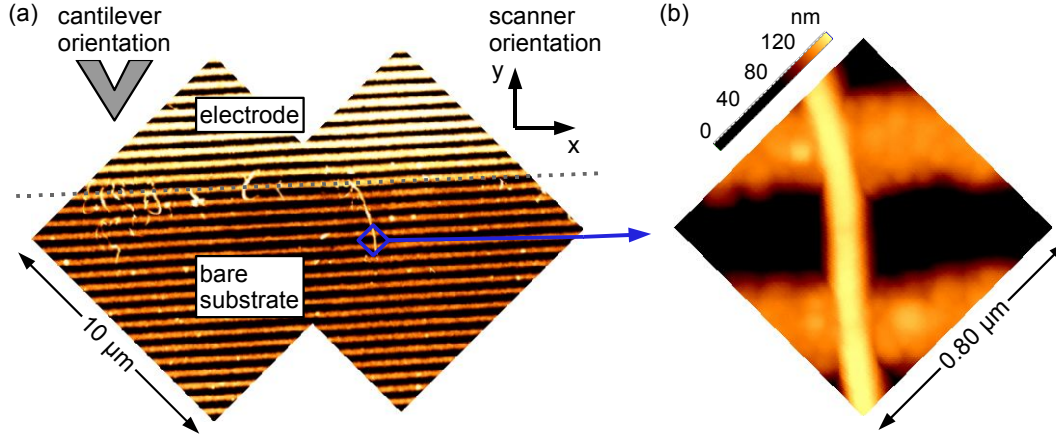


Figure 4.11: (a) Carbon nanotubes are deposited near an electrode on a v-groove GaAs substrate by ac electrophoresis. The opposing electrode is not visible at this scale. (b) A nanotube aligned in the y direction is pressed down at its midpoint with the AFM tip.

An improved method was developed in the course of this thesis, by adopting ac dielectrophoresis (Section 3.3.2) and force curves (Section 2.6) [78]. Electrodes are formed on a v-groove gallium arsenide (GaAs) substrate³ by thermal evaporation (Fig. 4.10), and ac electrophoresis is performed by depositing and drying drops of nanotube solution over the electrode gap with an ac voltage being applied.

Practically all the nanotubes are deposited at the electrode boundary [Fig 4.11(a)]. As the nanotubes are in general aligned perpendicular to the electrode, finding a suitably suspended nanotube is not too difficult if the v grooves are shorter than the nanotubes. The v groove width is 0.4 μm for Fig. 4.11(b). The nanotube midpoint is pressed down with an AFM tip, acquiring a force–displacement curve (F_k – Z curve, where Z is the z scanner displacement), as shown in Fig. 4.12(a) and (b). The slope of the curve in contact dF_k/dZ is the effective spring constant k_{eff} of the cantilever–nanotube system, which is related to the spring constants of the nanotube (k_{tube}) and

³The GaAs substrates were obtained from Dr. Benjamin Dwir of the Institute of Quantum Electronics and Photonics (IPEQ) at EPFL.

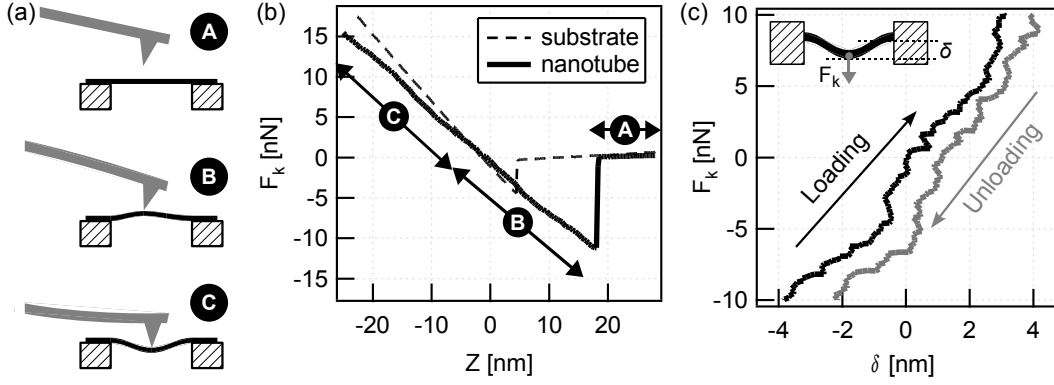


Figure 4.12: (a) Schematic of the different stages of a force curve. The AFM tip is in contact with the nanotube in stages B and C. (b) The loading force F_k (calculated from the cantilever deflection z) is plotted versus the z scanner displacement Z (solid line). Due to the nanotube deflection, the slope in contact (stages B and C) is different from that of a reference curve (dashed line). (c) F_k - δ_{tube} graph can be obtained by processing the F_k - Z curve.

the cantilever (k) by the following equation:

$$\frac{1}{k_{eff}} = \frac{1}{k} + \frac{1}{k_{tube}}. \quad (4.12)$$

k_{tube} can thus be calculated in relation to k , the normal spring constant of the cantilever, as in the Salvétat method. Equivalently, the F_k - δ_{tube} graph can be obtained by processing the F_k - Z data— δ_{tube} for a given F_k is the difference in Z values for the reference and nanotube F_k - Z graphs—and performing linear regression to calculate k_{tube} . Finally, the elastic modulus E_{tube} is calculated using Eq. 4.10.

The use of force curve demands attention to a number of practical details. Force curves are acquired after obtaining an AFM image. 2–3 minutes can pass between the midpoint imaging and the force curve acquisition, and any lateral thermal drift occurring in this period causes an error in the tip–nanotube relative position. Put simply, the AFM tip may miss the nanotube midpoint. To minimize the positioning error, Veeco Microlevers (unsharpened) of tip radius greater than 50 nm were used, and the force curves were acquired only when the thermal drift is low—AFM images were taken repeatedly and compared.

Another positioning error may come from the cantilever mounting geometry. As the cantilever is mounted at an angle α (12° in this case) to the x–y plane, the tip slides down the y axis when the cantilever deflects upwards [for the geometry shown in Fig. 4.11(a)]. The change in tip y position Δy due to cantilever deflection z is given by $\Delta y = -z \tan \alpha$ to the first order [100]. Hence for a given F range, it is best to use the stiffest cantilever available, as long as the force resolution is acceptable. Veeco Microlevers E and F offer a good compromise between the force resolution and the

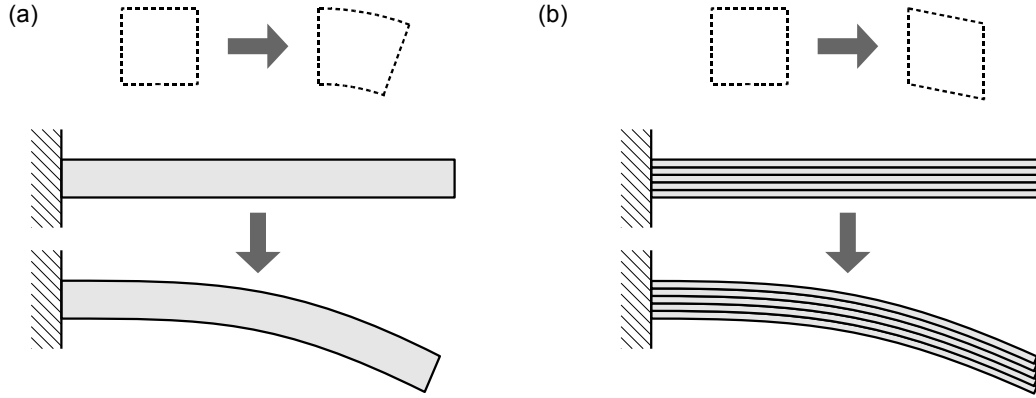


Figure 4.13: (a) The bending of an individual tube involves elongation of the outer arc and compression of the inner arc. (b) The bending of a bundle of tubes involves additional intertube shearing.

deflection-induced position error (see Table 2.1).

4.3 Previously Reported Mechanical Properties of Carbon Nanotubes

4.3.1 Exceptionally High Elastic Modulus of Arc-Discharge-Grown Carbon Nanotubes

Individual carbon nanotubes grown by arc-discharge evaporation show exceptional mechanical properties. Treacy et al. [94] obtained E_{tube} in the 0.4–4 TPa range for the arc-discharge-grown multiwall carbon nanotubes, with an average value of 1.8 GPa. Poncharal et al. [95] obtained a typical value of 1 TPa for the multiwall nanotubes thinner than 10 nm⁴. Using Treacy’s thermal-vibration method, Krishnan et al. [101] obtained an average value of 1.25 ± 0.35 TPa for the individual single-wall carbon nanotubes synthesized by arc-discharge evaporation. AFM studies gave similar results. Wong et al. [97] obtained 1.3 ± 0.6 TPa and Salvétat et al. [98] found 0.81 ± 0.29 TPa for arc-discharge-grown multiwall nanotubes. These values are in good agreement with the predicted value of 0.97 TPa [102].

4.3.2 Low Bending Modulus of Carbon Nanotube Bundles

Carbon nanotubes can aggregate in synthesis or handling to form bundles. Single- to quadruple-wall carbon nanotubes have been observed to prefer the bundled form [103, 104]. Because of the low interaction between the constituent tubes, a carbon nanotube bundle exhibits a much lower elastic modulus, as illustrated in Fig. 4.13.

⁴They also reported a diameter dependence, which will be discussed in comparison to the results of this thesis.

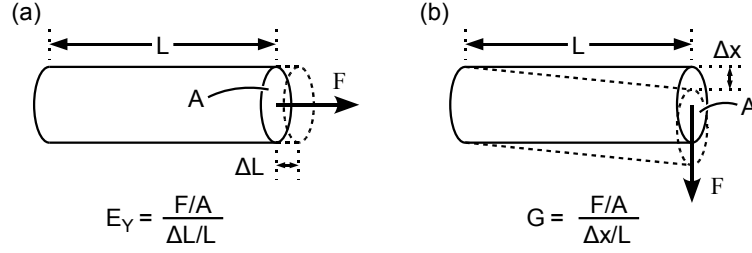


Figure 4.14: (a) Definition of Young's modulus E_Y . (b) Definition of shear modulus G .

Strictly, the elastic modulus E_{tube} calculated by Eq. 4.10 is not the Young's modulus, but the bending modulus. The deformation of a doubly clamped beam is more accurately described by

$$\delta_{tube} = \frac{F_k L_{tube}^3}{192 E_{tube} I_{tube}} = \frac{F_k L_{tube}^3}{192 E_Y I_{tube}} + f_s \frac{F_k L_{tube}}{4 G A_{tube}}, \quad (4.13)$$

where E_Y is the Young's modulus [Fig. 4.14(a)], G is the shear modulus [Fig. 4.14(b)], A_{tube} is the cross-sectional area, and f_s is the shape factor (~ 1) that varies with tube dimensions [105]. Replacing A_{tube} with $\pi D^4/4$ and I_{tube} with $\pi D^4/64$, we obtain

$$E_{tube} = E_Y \left(1 + 3 f_s \frac{E_Y}{G} \frac{D^2}{L_{tube}^2} \right)^{-1}. \quad (4.14)$$

For an isotropic and homogeneous material,

$$E_Y = 2 G (1 + \nu), \quad (4.15)$$

where ν is the Poisson ratio, and therefore

$$E_{tube} = E_Y \left(1 + 6 f_s (1 + \nu) \frac{D^2}{L_{tube}^2} \right)^{-1}. \quad (4.16)$$

$(D/L)^2$ diminishes for long and thin beams, so that E_{tube} is practically equal to E_Y .

For the multibody structure portrayed in Fig. 4.13(b), Eq. 4.14 is not valid since the shear involved is between the constituent tubes and not the shear in the tube material. The equation can nonetheless be of practical use for calculating the effective properties of the whole structure, especially if there is a large number of tubes in the bundle. As the shear strain is dominated by the *intertube* shear, Eq. 4.15 and subsequently Eq. 4.16 cannot be used. When G assumes a value much lower than $E_Y/2(1 + \nu)$, the bending modulus of carbon nanotube bundles would exhibit a strong diameter dependence not observed in the bending of individual carbon nanotubes. Indeed, the diameter dependence was observed by Salvétat et al. [103] for single-wall nanotube

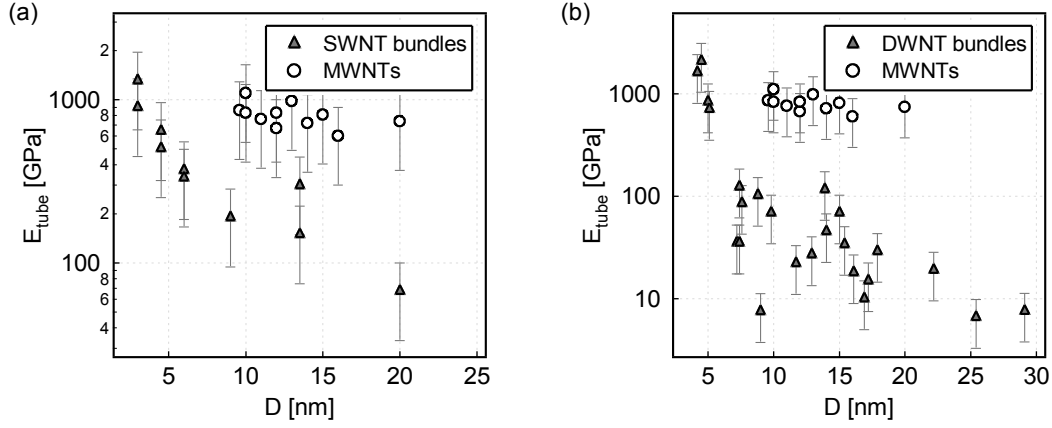


Figure 4.15: Bending modulus of carbon nanotube bundles compared to individual nanotubes. (a) Single-wall nanotube bundles (triangles; Ref. [103]) and individual multiwall nanotubes (circles; Ref. [98]) from arc-discharge evaporation. (b) Double- to quadruple-wall nanotube bundles (triangles; Ref. [104]) from chemical vapor deposition and individual multiwall nanotubes (circles; Ref. [98]) from arc-discharge evaporation.

bundles [Fig. 4.15(a)] and by Lukić et al. [104] for double- to quadruple-wall nanotube bundles [Fig. 4.15(b)]. Both works showed that the shear modulus G is close to or less than 1 GPa.

The low bending modulus may be problematic for the material application of carbon nanotube bundles. Kis et al. [106] demonstrated a solution, where bundles irradiated with electron beam showed an increase in bending modulus. The increase is due to the strong intertube covalent bonds that form during the electron–nanotube interaction.

4.3.3 Low Elastic Modulus of CVD-Grown Carbon Nanotubes

Compared to the arc-discharge-grown nanotubes, multiwall carbon nanotubes grown by chemical vapor deposition show inferior structural properties [52]. While arc-discharge-grown tubes are straight, CVD-grown nanotubes in general have a curly shape (Fig. 3.3), indicating the abundance of defects. Most seriously, the walls are not oriented parallel to the nanotube axis. Due to the misalignment, nanotube walls are seldom continuous over 100 nm, and wall discontinuities can be readily observed in TEM images [Fig. 4.16(a)]. A CVD-grown multiwall carbon nanotube is thus a complex structure composed of tube and cone (open and closed) fragments.

The fragmented structure of the CVD-grown nanotube results in a low Young's modulus [107]. The works by Salvétat et al. [98] and Lukić et al. [108] report 10–100 GPa Young's modulus for CVD-grown tubes, at least an order of magnitude lower than that of arc-discharge-grown tubes. It should be noted that Lukić et al. [108] investigated the effects of thermal annealing. TEM imaging showed a slight improvement in the definition of walls [Fig. 4.16(a)], but the bending modulus did not show any noticeable

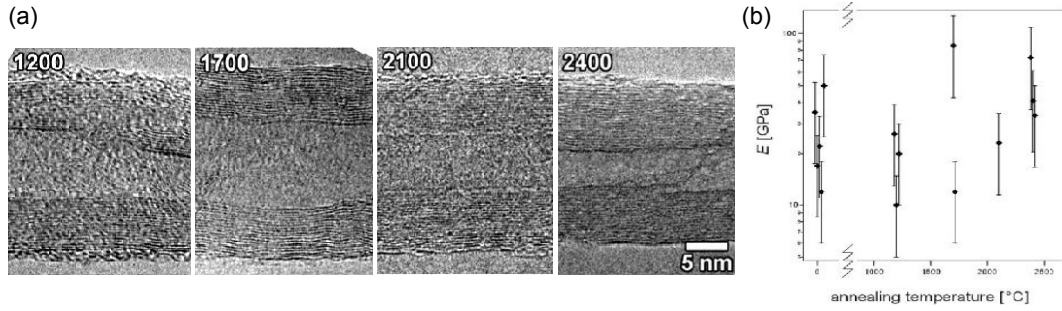


Figure 4.16: (a) Thermal annealing at the indicated temperatures generally improved the graphitic structure of multiwall carbon nanotubes. (b) But the bending modulus showed little if any improvement.

change [Fig. 4.16(b)]. The result is not surprising, as thermal annealing cannot correct the wall misalignment [109].

4.4 Diameter-Dependent Elastic Modulus of CVD-Grown Carbon Nanotubes

As chemical vapor deposition is the only method capable of large-scale production, the low structural quality of CVD-grown nanotubes is a serious problem that hinders a wider adoption of carbon nanotubes in material applications. A turning point in our research on carbon nanotubes came with the work on double- to quadruple-walled carbon nanotube bundles grown by CVD [104]. The bending modulus showed a diameter dependence typical of bundles (Section 4.3.2), but the small-diameter (< 5 nm) structures, probably individual tubes, displayed the ideal 1 TPa Young's modulus [Fig. 4.15(b)]. As our previous low-Young's-modulus results on CVD-grown multiwall carbon nanotubes were obtained from tubes of large diameter (> 15 nm), the double-wall nanotube results prompted us to investigate whether the nanotube elastic modulus shows a diameter dependence, if a proper diameter range is covered.

4.4.1 Experiment

Materials

Two batches of CVD-grown multiwall carbon nanotubes were used in the study: (I) nanotubes produced in the temperature range of 700–800 °C using acetylene as the carbon precursor and cobalt (Co) nanoparticles as catalysts on a sodium yttrium (NaY) zeolite support [110], and (II) nanotubes obtained by heat-treating a sample of the first batch to 2400 °C in a graphitization furnace. We had already reported that heat treatment could not improve the mechanical properties [108]. Nanotubes from both batches of similar diameter gave very close elastic modulus values, confirming that the

two batches were equal in their mechanical properties. The nanotubes were dispersed in ethanol and isopropanol using an ultrasonic finger before deposition.

Deposition

The batch I nanotubes were deposited by filtering with a polished alumina ultrafiltration membrane, and the batch II nanotubes were deposited using ac dielectrophoresis. Both methods are described in Section 3.3.2. The batch II nanotubes were easier to deposit with ac dielectrophoresis (Section 3.3.2), probably because of heat-induced changes in the surface structure [109]. A gallium arsenide substrate with 200 nm-deep trenches microfabricated at 0.5 μm intervals was used for the ac dielectrophoresis. Gold electrodes 30 nm thick with a 100 μm gap were prepared on the substrate by thermal evaporation, and ac dielectrophoresis was performed while applying a 20 V_{peak-to-peak} 10 MHz sinusoidal signal between the electrodes. The deposition results are shown in Fig. 4.8(a) and Fig. 4.11(b).

Stiffness Measurement

The stiffness ($dF_k/d\delta_{tube}$) of suspended carbon nanotube structures, where F_k is the loading force and δ_{tube} is the midpoint deflection, was also measured by two different methods. Salvétat's contact-AFM-imaging method was used for the batch I nanotubes, and the force curve method was used for the batch II nanotubes. The methods are described in Section 4.2.2. Altogether, 25 individual multiwall carbon nanotubes were analyzed.

Model

A suspended nanotube was modeled as a doubly clamped beam (Fig. 4.7) of uniform cross section, made of homogeneous and isotropic material. The Young's modulus E_{tube} was calculated by Eq. 4.10.

4.4.2 Results and Discussion

Figure 4.17 shows our results. The elastic modulus E_{tube} varies dramatically in the 10–20 nm diameter range, increasing almost exponentially with decreasing diameter. Data for small-diameter double- to quadruple-wall carbon nanotube bundles [104] have been included to show the upper limit possible with CVD-grown nanotubes (triangles in Fig. 4.17). Previous results on multiwall carbon nanotubes [98] and small-diameter single-wall nanotube bundles [103] are also included in the graph for comparison (squares in Fig. 4.17). Unlike the CVD-grown multiwall nanotubes, the arc-discharge-grown nanotubes show fairly constant elastic modulus over the same diameter range.

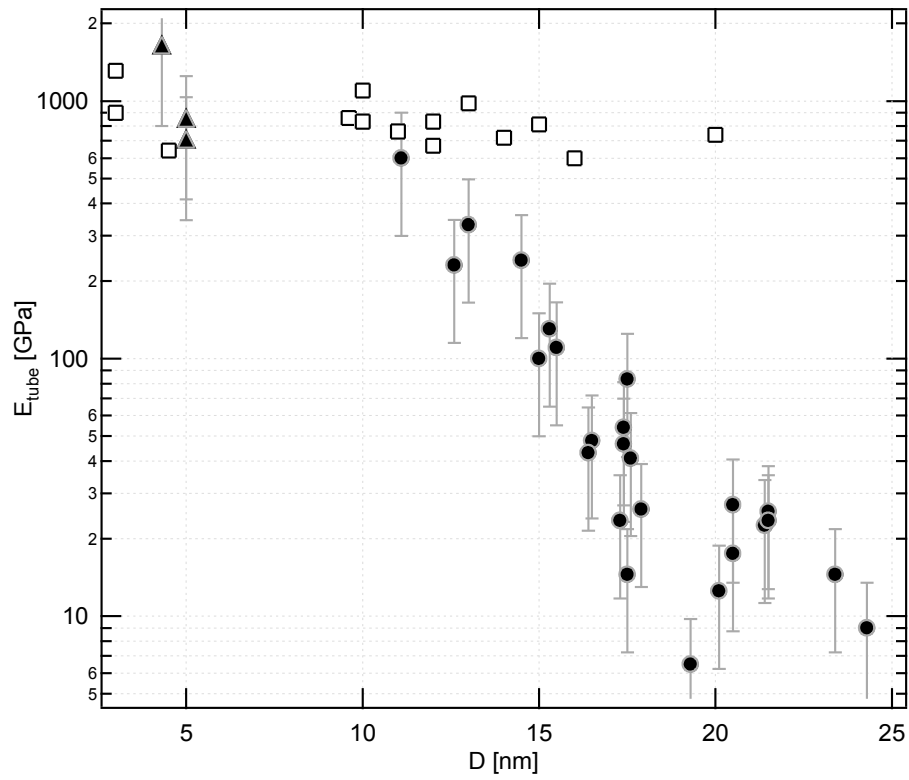


Figure 4.17: Circles: results on CVD-grown multiwall carbon nanotubes. Triangles: bending modulus of small-diameter CVD-grown double-wall carbon nanotube bundles [104]. Squares: bending modulus of multiwall carbon nanotubes grown by arc-discharge evaporation [98] and small-diameter single-wall carbon nanotube bundles [103].

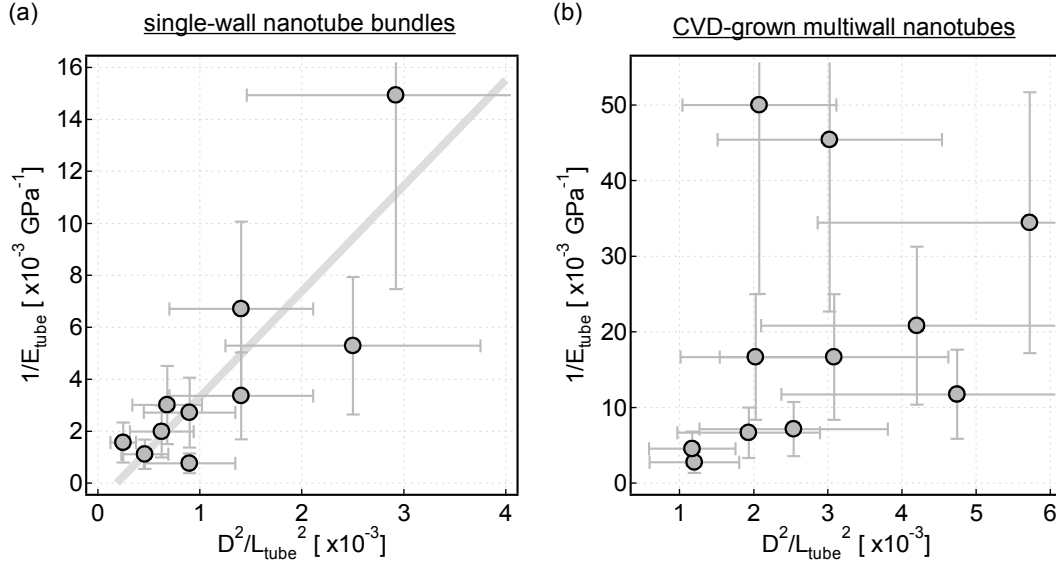


Figure 4.18: The $1/E_{tube}$ versus D^2/L_{tube}^2 graphs for (a) single-wall nanotube bundles from arc-discharge evaporation [103] and (b) the batch II multiwall nanotubes used in this study.

Bundling? Diameter-Independent Material Quality?

It should be first discussed whether the observed diameter dependence is not the shearing-in-bundle effect described in Section 4.3.2. Study by TEM showed that nanotubes from the two batches in the 10–25 nm diameter range were individual tubes and not bundles. Also, we avoided any structure that diverged at its ends or changed significantly in diameter along its length when observed with AFM, thereby avoiding any bundle that may have formed during the dispersion and the deposition.

Another evidence that the nanotubes were not bundles can be obtained from the correlation between $1/E_{tube}$ and D^2/L_{tube}^2 data. Diameter-independent E_Y and G values can be assumed for nanotubes in a bundle, and according to Eq. 4.14, $1/E_{tube}$ and D^2/L_{tube}^2 should have a linear relationship. It is indeed the case for single-wall nanotube bundles grown by arc-discharge evaporation [103], as shown in Fig. 4.18(a). Graph in Fig. 4.18(b) for batch II multiwall nanotubes does not show a similar correlation, indicating that the multiwall nanotubes used in the experiment were not bundles.

The same argument applies to the possibility that the nanotubes may have identical stacked-cup or stacked-open-cone structures at different scales. These structures, since they have a high E_Y to G ratio (dependent on the misorientation between the wall direction and the nanotube axis [98]), would still exhibit a diameter dependence of E_{tube} according to Eq. 4.14. But Fig. 4.18(b) shows that our results cannot be explained by Eq. 4.14, refuting the stacked-cone model. The strong, almost exponential change of bending modulus in the 10–20 nm range cannot be accounted for by the polynomial behavior of Eq. 4.14 nor by corrections to the coefficients to allow for a hollow core.

Furthermore, we could not find any regularity in the structure of the nanotubes by TEM.

Radial Deformation

As the radial deformation of a carbon nanotube depends on its curvature, a false diameter dependence may be observed if the radial deformation is significant. However, the stiffness of AFM tip–nanotube contact was already discussed by Salvétat et al. [98], who concluded that the theoretical ~ 200 N/m stiffness calculated as $(6 F_k \bar{R} E^*)^{1/3}$, where \bar{R} is the reduced radius of curvature $(1/R_t + 2/D)^{-1}$ (R_t : AFM tip radius), and E^* is the reduced elastic modulus of the tip–nanotube system (~ 200 GPa), was too high compared to the stiffness of a suspended nanotube (typically < 10 N/m). The estimated ~ 200 N/m has been verified experimentally [111]. Furthermore, the diameter dependence of the radial stiffness is in the opposite direction to the trend observed.

Diameter Dependence for Very Small Nanotubes

A number of theoretical works have actually predicted the carbon nanotube elastic modulus to drop with decreasing diameter because of the excessive strain imposed on the graphene shells at small diameters [112, 113]. But the effect is important only for small-diameter (< 1.5 nm) single-wall nanotubes, and so we believe that the phenomenon is not relevant to our results, as we are dealing with multiwall nanotubes of larger diameters.

Diameter Dependence Observed by Poncharal et al.

In contradiction to our previous data on arc-discharge-grown nanotubes (squares in Fig. 4.17), Poncharal et al. [95] observed a diameter dependence in the bending modulus of individual multiwall nanotubes grown by arc-discharge evaporation. They attributed the diameter dependence to the rippling of nanotube walls that was observed on some curved nanotubes. But the effect of rippling on the bending modulus is unclear. Poncharal et al. asserted that the ripple-bending mode is a linear bending mode, because the frequency response they obtained did not show any asymmetry typical of nonlinear oscillators [Fig. 4.5(d)]. But a theoretical study showed that the rippling mode must be nonlinear, contrary to Poncharal’s predictions [114]. In our F_k – δ_{tube} data, we did not find any transition from the linear small-deflection bending mode to the nonlinear ripple-bending mode. It is possible that the ripples were never introduced during our experiments due to the lower curvatures experienced by our nanotubes.

A recent molecular-dynamics simulation offers an alternative explanation to Poncharal’s data. Akita et al. [115] showed intershell van der Waals interactions in a vibrating double-wall nanotube to dissipate energy, and the simulated results agreed well with their experimental data. The proposed damping mechanism can explain (a) why

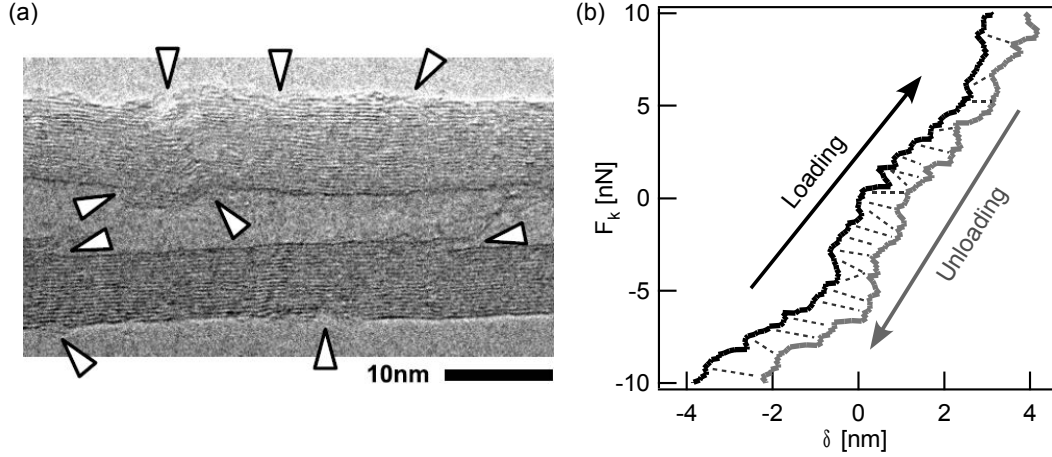


Figure 4.19: (a) TEM image of a CVD-grown multiwall carbon nanotube shows an abundance of defects, the most serious of which are the wall discontinuities indicated by markers. (b) Matching kinks (indicated by dashed lines) are found in the F_k - δ_{tube} loading and unloading curves, suggesting intratube stick-slip events.

Poncharal observed low quality factors (< 500), (b) why the frequency response was a Lorentzian typical of a damped harmonic oscillator, and (b) why Poncharal observed a diameter dependence in bending modulus. The dynamic intershell interactions, however, would not play a role in our static methods. For these reasons, we believe that our diameter dependence was not caused by the surface rippling of nanotubes.

We have exhausted the possibility of our diameter dependence being false or stemming from a material-independent factor. Therefore, we conclude that the observed diameter dependence is a reflection of the diameter-dependent material quality: when grown by chemical vapor deposition, thinner multiwall carbon nanotubes are structurally superior to the thicker tubes.

Intrananotube Stick-Slip

It was mentioned earlier that a CVD-grown multiwall nanotube should be viewed as a multibody structure composed of nanotube fragments, as the walls are not continuous over long ranges [Fig. 4.19(a)]. If so, is it possible that the nanotube bending occur through a series of stick-slip events between the fragments rather than through a smooth deformation of the material? The carbon-carbon (C-C) bond (from the overlap of sp^2 -hybridized orbitals) in a graphite plane is extremely strong—the elastic constant c_{11} for tensile deformation is 1 TPa, and the elastic constant c_{66} for in-plane shear is $(c_{11} - c_{12})/2 = 330$ GPa [103]. And as the plane-plane shear of graphite ($c_{44} = 4.5$ GPa) is linear at best to the C-C bond length (3.534 \AA), it seems probable that the deformations in our experiment (maximum $\delta_{tube} \approx 10 \text{ nm}$) involved more than the reversible shear between graphitic shells.

Experimental evidence is present in our F_k - δ_{tube} curves. Numerous *kinks* are present, and we find matching pairs of kinks in the loading and unloading curves [Fig. 4.19(b)]. These are details that were not available in the original Salvétat method. The kinks are not perfectly periodic, and some large kinks in a curve are divided into smaller kinks on the other curve. These clues hint that the kinks come from mechanical instabilities. As our AFM tip slips by roughly 10 nm along the nanotube [y axis in Fig. 4.11(a)] over a 20 nN loading range, one may consider the atomic-scale stick-slip motion of the AFM tip on graphite [116] as the source of these kinks. But the aperiodicity of the kinks is difficult to explain with this idea. In our opinion, the kinks are related to the stick-slip motion in a nanotube fragmented by structural defects—coffee-cup structures, bamboo nodes, incomplete shells, etc.

The diameter-dependent elastic modulus thus points to the diameter-dependent abundance of structural defects. Thicker nanotubes are more fragmented than thinner tubes. The diameter dependence has important implications on the growth mechanism of carbon nanotubes by chemical vapor deposition, as explained in the next Section.

4.5 Metastable-Catalyst Model of Carbon Nanotube Growth

4.5.1 Vapor–Liquid–Solid Model

As briefly introduced in Section 3.2.2, the vapor–liquid–solid (VLS) model⁵ is frequently adopted to explain the carbon nanotube growth by chemical vapor deposition [53]. Precursor gas molecules (*vapor*) dissociate at the surface of a metal nanoparticle at high temperatures, and carbon atoms dissolve into the molten nanoparticle (*liquid*). Upon passing the supersaturation limit, the carbon atoms precipitate out as the nanotube crystal (*solid*). The metal nanoparticle is the *catalyst* of precursor dissociation, and subsequently, the catalyst of nanotube growth. The VLS model is illustrated in Fig. 4.20.

The details of the catalytic growth, however, are not clearly understood, and the exact role of the catalyst is a topic of intensive study [53]. For example, the dissociation of precursor molecules and the precipitation of carbon nanotube are considered to occur at different sides of the catalyst, but the driving force for the necessary diffusion has not been clearly explained. While the concentration gradient is expected to play the dominant role [119], the effects of temperature gradient [120]—precursor decomposition is often exothermic (for hydrocarbon precursors) and the nanotube precipitation is endothermic—are also being investigated.

⁵The VLS model was first proposed by Wagner and Ellis [117] to explain the silicon nanowire growth from gold nanoparticles, and then it was adapted to explain the growth of carbon filaments [118].

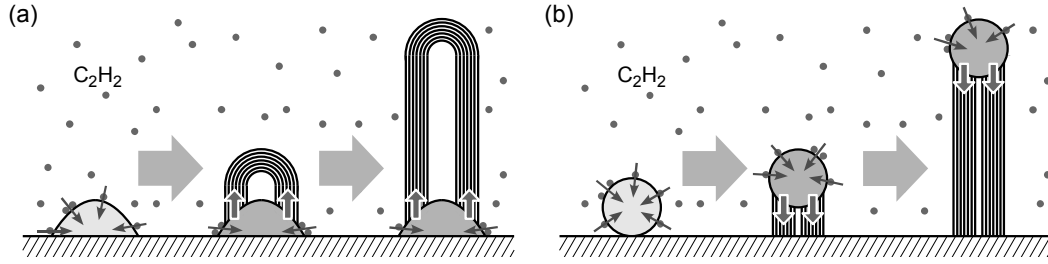


Figure 4.20: In the CVD synthesis of carbon nanotubes, carbon atoms from precursor molecules first dissolve into the catalyst and then precipitate out as the nanotube crystal. Both (a) the base growth and (b) the tip growth have been observed.

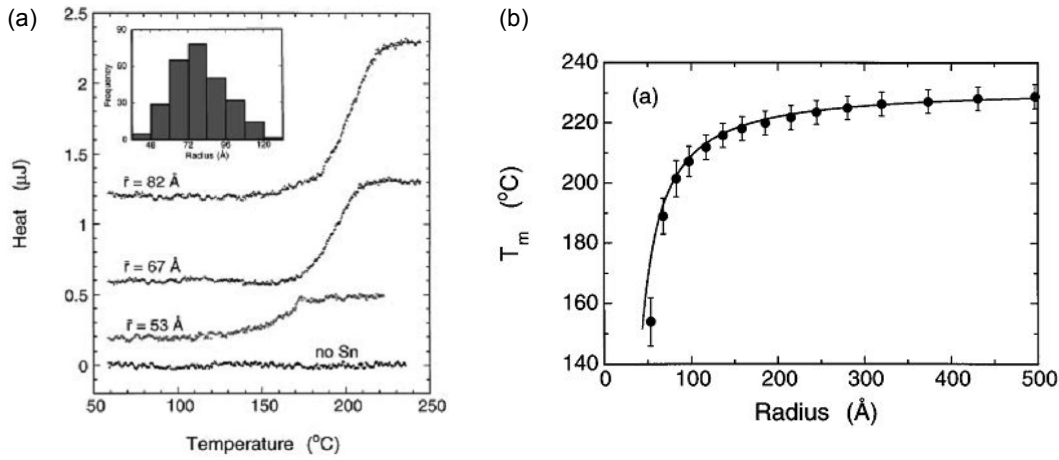


Figure 4.21: Calorimetric measurements of tin nanoparticle melting point, as carried out by Lai et al. [122] (a) The heat needed to raise the temperature of a stage coated with tin (Sb) nanoparticles is obtained. The sudden change in curve indicates the melting of nanoparticles. The inset shows the size distribution of 16.4 nm-wide nanoparticles. (b) The melting point drops as the particle size decreases.

4.5.2 Nanoparticle Melting Point Depression Effect

An important issue is whether the catalyst is solid or liquid during the nanotube growth. While the original model by Wagner and Ellis [117] assumes a liquid catalyst, the issue is unclear for carbon nanotubes, because the CVD process temperature is often much lower than the bulk melting temperature [121]. For example, the bulk melting point (T_m) of cobalt (Co) in methane atmosphere is 1321 °C, while CVD processes using cobalt nanoparticles are usually carried out at temperatures 700–1000 °C.

The melting point of a metal nanoparticle T_m^{NP} is lower than the bulk value T_m^{bulk} because of the high surface-to-volume ratio. The cohesive energy of an atom at or near the surface is lower than that inside the bulk, because of the reduced number of neighboring atoms. To the first order, the *Gibbs–Thompson* melting-point-depression

effect can be described by

$$T_m^{NP} = T_m^{bulk} \left(1 - \frac{V_M}{\Delta H_m} \frac{4\gamma^{SL}}{D_{NP}} \right), \quad (4.17)$$

where V_M is the molar volume of the solid, γ^{SL} is the surface tension between the solid and the liquid, ΔH_m is the melting molar enthalpy of the solid, and D_{NP} is the nanoparticle diameter [123]. Eq. 4.17 indicates that the melting point depression is proportional to the particle surface curvature. The melting point depression of metal nanoparticles can be verified experimentally, either by monitoring changes in the TEM diffraction pattern [124] or by calorimetry (Fig. 4.21) [122].

Homma et al. [121] monitored the morphological change of 30 nm cobalt nanoparticles after heating, and concluded that the nanoparticle melting point is 600 °C in a methane atmosphere, more than 700 °C lower than the bulk melting point. They also obtained similar results on 30 nm iron nanoparticles ($T_m^{bulk} = 1148$ °C, $T_m^{NP} = 650$ °C in methane).

While the small size (typically 1–20 nm) may allow a catalyst nanoparticle to melt at the CVD process temperatures, other factors involved in the nanotube growth complicate the prediction of the exact physical state. The dissociation of precursor molecules is exothermic for hydrocarbon gas [120], and the generated heat is absorbed by the catalyst particle. When carbon atoms dissolve into the catalyst, the melting point varies with the carbon content, and the dependence is not monotonic [125, 126]. The precipitation of carbon in the form of a nanotube is an endothermic process that takes away heat from the catalyst [53]. Once the nanotube precipitates, the nanotube–catalyst interface strongly influences the catalyst melting point [127, 128]. Strong catalyst–substrate adhesion leads to the base-growth mode [Fig. 4.20(a)], and then the catalyst–support interface becomes as important as the catalyst–nanotube interface [129, 130]. For typical CVD processes, all three states—completely liquid, partially liquid, and completely solid—may coexist due to a distribution in the catalyst size and these factors.

4.5.3 Partially Liquid Catalyst—Solid Core, Liquid Skin

A partially liquid particle is possible because melting starts at the surface. The melting point T_m^{NP} refers to the temperature at which the whole nanoparticle is liquid, and it is known that a nanoparticle can have the solid core–liquid skin structure below T_m^{NP} [131]. When a nanoparticle is partially liquid, the factors that influence the melting temperature would influence the thickness of the liquid skin (Fig. 4.22).

Metastability

The liquid skin, especially when it is thin, is metastable. Its thickness and morphology depends on the history of heat exchange [132]. Precursor dissociation, carbon dissolution, and carbon precipitation are exothermic or endothermic processes that may

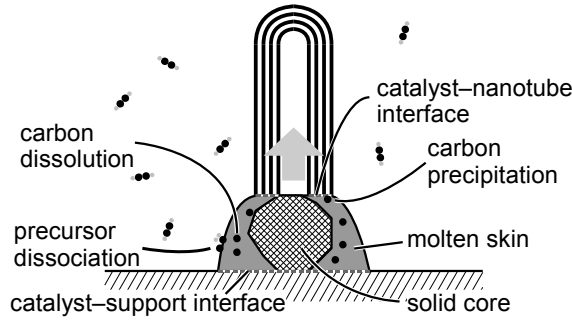


Figure 4.22: Growth of multiwall carbon nanotube from a partially liquid catalyst. Different factors influencing the liquid-skin thickness are indicated.

appear to the catalyst as discrete events, on the time scale at which changes can occur to its liquid skin. The catalyst's liquid skin would thus be continuously agitated by these processes, and suffer stochastic perturbations in its thickness and morphology.

4.5.4 Size-Dependent Structural Quality of Carbon Nanotubes

TEM studies have shown that liquid catalysts favor tubular high-quality growth [Fig 4.23(a)], while solid catalysts create defective structures [Fig 4.23(b)] [127, 134, 133, 135]. Bartsch and co-workers [133, 135] notably reported that fast tubular growth from small liquid catalysts dominated the early stage of CVD before eventually being outnumbered by slow bamboo-like growth from larger solid catalysts. The small-diameter tubular nanotubes would have good mechanical properties, while the large-diameter bamboo-like nanotubes would show poor structural qualities.

The nanotubes created by partially molten catalysts are of particular interest to us. TEM studies show that a nanotube can oscillate from tubular to defective growth [Fig. 4.23(c)], and such oscillations may be a property of metastable, partially molten catalysts. Instabilities that change the nanoparticle melting point would cause partial melting and freezing of the liquid layer. According to the *metastable-catalyst* growth model proposed by Kukovitsky et al. [127], the corresponding perturbations at the catalyst-nanotube interface would result in alternating growth modes, as the carbon diffusion through the liquid skin is much faster than the diffusion through the solid catalyst.

The frequency and the gravity of perturbation would depend on the catalyst size. Under the same conditions, the smaller catalyst would have a thicker liquid skin due to its larger surface-to-volume ratio. The thicker skin would lead to a less frequent fluctuation at the nanotube-catalyst interface, as well as allowing a more stable carbon diffusion despite some perturbations (Fig. 4.24). Hence a multiwall carbon nanotube with a better structure would grow from the smaller catalyst.

Our results on the elastic modulus of multiwall nanotubes grown by a single CVD process shows a *transition-like* change in the elastic modulus over the 10–20 nm range

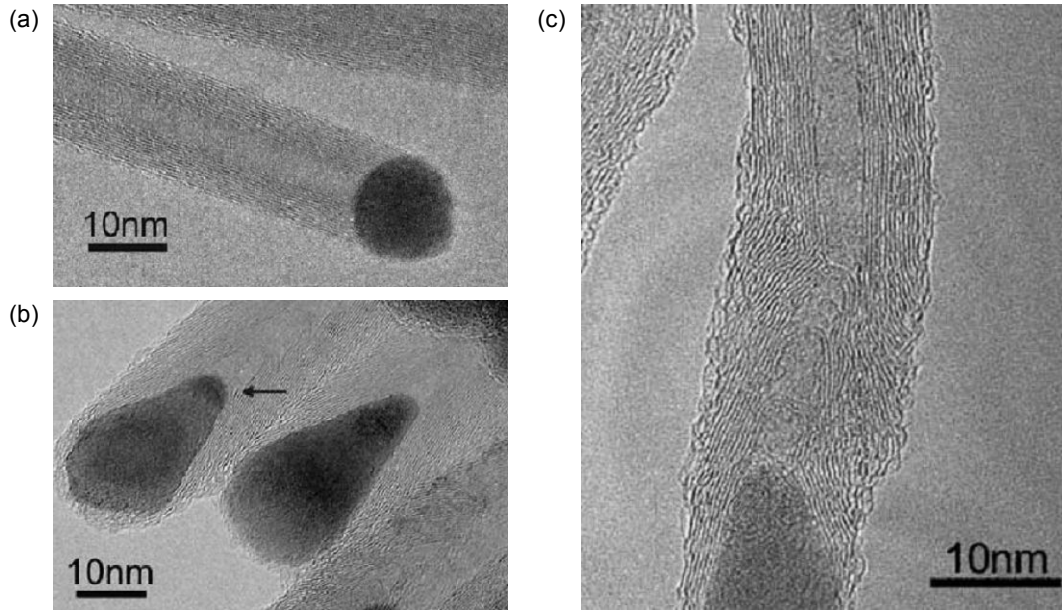


Figure 4.23: TEM images of catalysts and their nanotubes after CVD growth [133]. (a) Spherical catalysts show tubular carbon nanotube growth, (b) while conical, faceted catalysts show defective growth. (c) The well-defined transition from tubular growth to defective growth suggests a corresponding sphere-to-cone shape change of the catalyst.

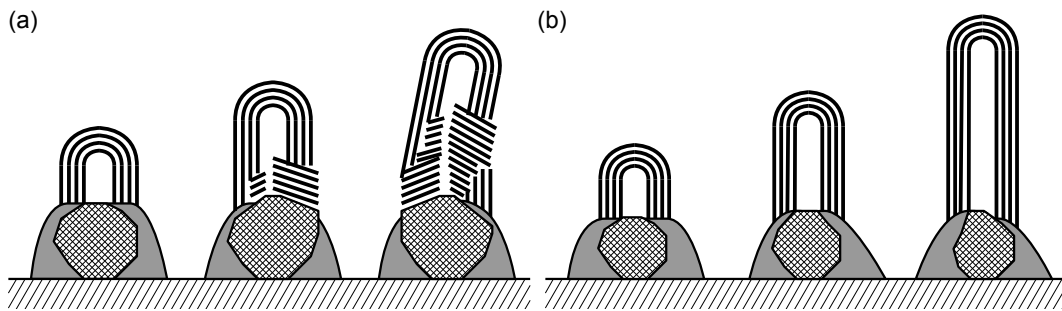


Figure 4.24: (a) Perturbations at the liquid skin lead to perturbations at the catalyst-nanotube interface. The nanotube growth mechanism fluctuates, leading to a defective structure. (b) A smaller catalyst has a thicker liquid skin and is thus more resistant against perturbations. The catalyst-nanotube interface remains stable, and a high quality nanotube is created.

(Fig. 4.17). The observed diameter dependence can be explained by the metastable-catalyst model. We believe that the large-diameter (> 20 nm) low-modulus (~ 10 GPa) nanotubes were grown from solid catalysts, and that the nanotubes in the 10–20 nm range were grown from metastable catalysts. Considering that 30 nm cobalt nanoparticles have been observed to melt at $600 \pm 50^\circ\text{C}$ in methane atmosphere on silica support [121], our 10–20 nm transition range is situated slightly lower than expectation. The difference could be due to a number of reasons: a catalyst often produces a nanotube thinner than its size, and the carbon precursor and the support were different for our nanotubes. Nonetheless, the diameter-dependent variation of the elastic modulus is a strong evidence for the metastable-catalyst growth model.

4.6 Conclusions and Outlook

The mechanical properties of surface-bound nanowires were studied by atomic force microscopy. We have measured the elastic modulus of individual multiwall carbon nanotubes grown from a single CVD process. The data show the elastic modulus changing dramatically in a narrow diameter range. The diameter dependence in elastic modulus is a strong evidence for the metastable-catalyst growth of multiwall carbon nanotubes in CVD.

It is difficult to arrive at the near-exponential diameter dependence starting from the growth model. Successfully modeling the stochastic perturbations at the liquid-skin and accurately predicting the type and frequency of induced defects are daunting tasks. Calculating how the different structural defects influence a nanotube’s mechanical strength is also very challenging. A possible solution is to model a metastable catalyst to be oscillating between liquid and solid forms, with the time constants determined by the environment and the catalyst size. The produced nanotube should then be modeled as a series of high-quality segments joined by poor-quality nodes, the lengths of these parts being related to the time constants of the liquid and solid forms. It would be interesting to study if such a simple model can reproduce the strongly nonlinear, diameter-dependent change in the elastic modulus.

Our data suggests that high-quality nanotubes can be obtained chemical vapor deposition, but it also shows that a good control over the catalyst’s physical state is necessary to achieve a high yield of pristine nanotubes. The ease or difficulty with which the liquid–solid state can be controled should become an important criterion in selecting a catalyst. Research is under way in our group to find the catalyst that will maintain a stable liquid skin, with the goal of producing perfect multiwall carbon nanotubes by chemical vapor deposition.

5 Metrological Properties of Surface-Bound Nanoparticles

Surface-bound nanoparticles show size-dependent catalytic and optical properties. Dynamic AFM is the most reliable tool for measuring the size of nanoparticles, but its bistable nature causes anomalies in the measurement. Novel experimental data that exemplify different problems are presented, and the problems are explored with a realistic numerical model of the dynamic AFM.

5.1 Size-Dependent Properties of Nanoparticles

5.1.1 Catalytic Properties

Different semiconductor nanowires can be grown by chemical vapor deposition (CVD), using metal nanoparticles as catalysts (Section 3.2.2). As the TEM images in Figs. 5.1(a)–(c) show, the nanowire diameter is determined by the catalyst size. The relationship between the nanotube diameter and the catalyst size is more complicated for CVD-grown single-wall carbon nanotubes [Fig. 5.1(d)] [139]. CVD-grown multiwall carbon nanotubes show a more direct diameter dependence on the catalyst size [48], and hence controlling the catalyst nanoparticle size is the first step towards growing carbon nanotubes of uniform diameter. As the kinetics of the carbon nanotube CVD growth is sensitive to the catalyst size (Chapter 4), the size measurement of surface-bound catalyst nanoparticles is an important issue.

5.1.2 Optical Properties

The optical properties of metal nanoparticles are dominated by surface the collective oscillation of conduction electrons resulting from the interaction with electromagnetic radiation [140]. These properties are mainly observed in gold, silver, and copper, because of the presence of free conduction electrons. The electric field of the incoming radiation induces the formation of a dipole in the nanoparticle. A restoring force in the nanoparticle tries to compensate for this, resulting in a unique resonance wavelength [Fig. 5.2(a)]. The plasmon resonance wavelength depends on a number of factors, among which the particle size and shape, as well as the properties of the surrounding medium, are the most important. For nonspherical particles, such as rods, the reso-

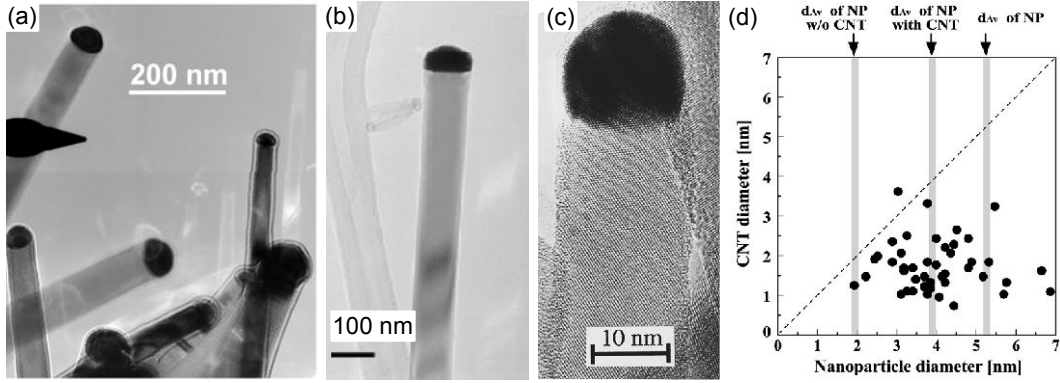


Figure 5.1: TEM images of (a) Ge [136], (b) ZnO [137], and (c) Si [138] nanowires grown with gold nanoparticle catalysts show that the nanowire diameter is determined by the catalyst size. (d) Size relationship between ferritin nanoparticles and the resulting single-wall carbon nanotubes, as reported by Jeong et al. [139]

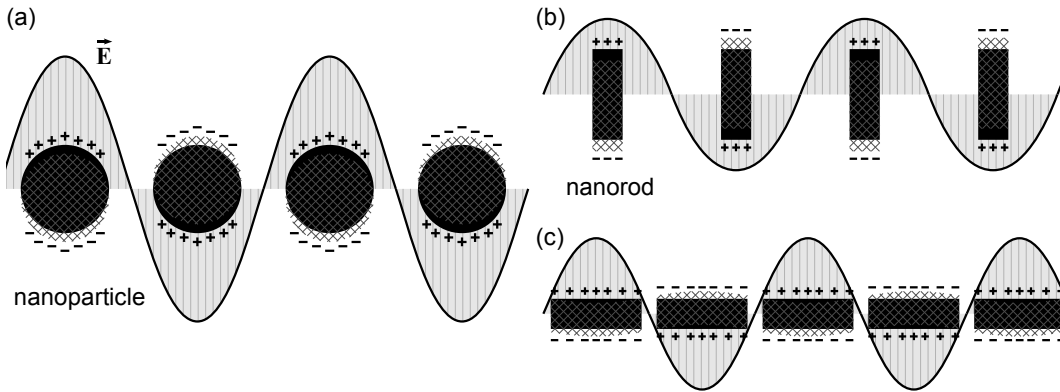


Figure 5.2: (a) A spherical nanoparticle absorbs light most efficiently when the frequency matches the plasmon resonance frequency. (b) The optical absorption by a nanorod is orientation-dependent.

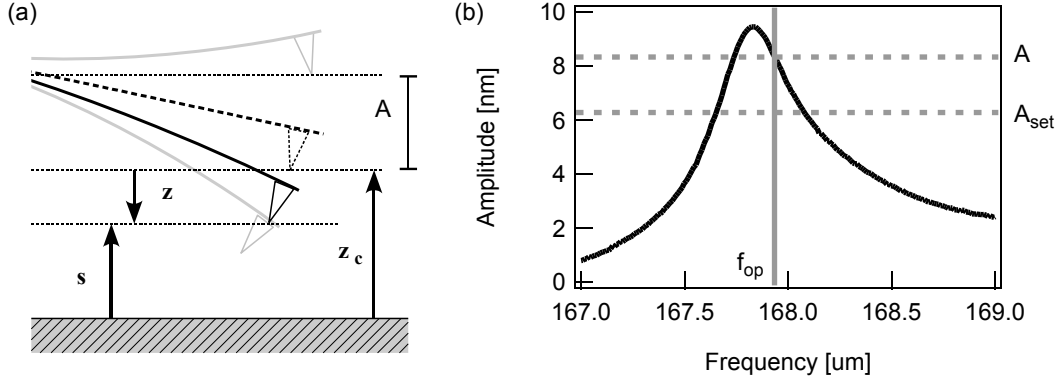


Figure 5.3: (a) Schematic of an oscillating cantilever. z_c : tip-sample rest separation; z : tip displacement from rest position; s : instantaneous tip-sample separation. $z_c + z = s$. (b) In AM-AFM, the dynamic response of an AFM cantilever is obtained before engaging the surface. The initial oscillation amplitude A_o is determined by the operation frequency f and the piezo driving voltage. The controller approaches the surface until the tip-surface interactions dampen down the oscillation amplitude to the setpoint A_{set} .

nance wavelength depends on the orientation of the electric field. The transverse and longitudinal oscillations have different resonance wavelengths [Fig. 5.2(b)].

To study the optical properties of a single nanoparticle, the nanoparticles need to be bound on a substrate and analyzed individually [141]. For a such study, it is again important to be able to determine the size of a surface-bound nanoparticle accurately.

5.2 Anomalies in Size Measurement by Dynamic AFM

Dynamic atomic force microscopy (AFM), introduced in Section 2.8, is often the only option in measuring the size of surface-bound nanoparticles accurately. Scanning tunneling microscopy (STM) cannot be used on insulating substrates. Transmission electron microscopy (TEM) requires an electron-transparent substrate, and hence is unsuitable for substrates that are difficult to thin down to an acceptable level of transparency. Scanning electron microscopy (SEM) has a lateral resolution of 1–20 nm due to the finite volume of electron-matter interaction, and thus cannot measure the size of small nanoparticles (< 20 nm) accurately. Contact AFM (Section 2.5) can give accurate measurements, but the lateral forces generated during operation can displace nanoparticles that are not strongly bound to the substrate. It is the author's experience that even the weakly-bound nanoparticles unsuitable for contact AFM can be imaged stably using the dynamic AFM.

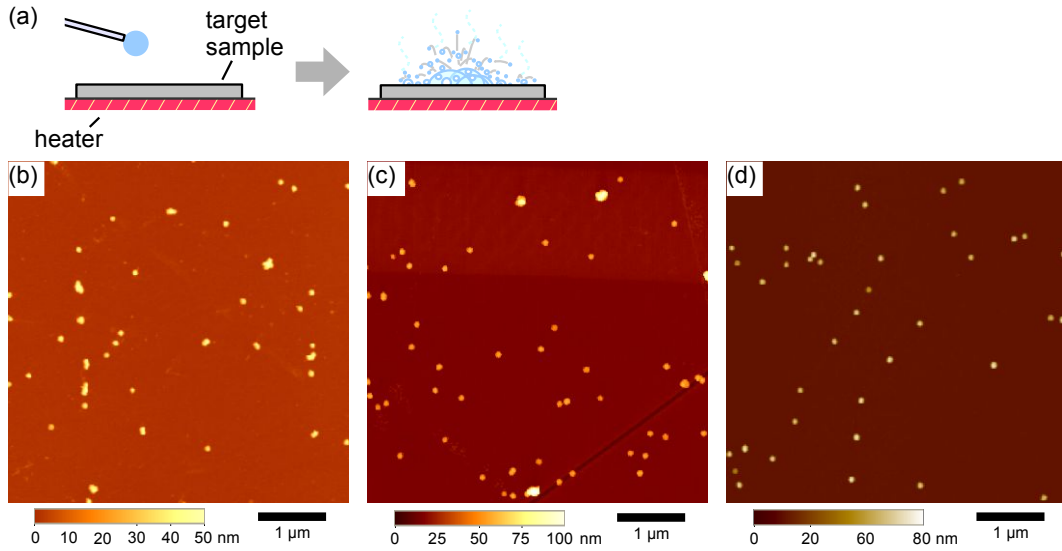


Figure 5.4: Surface-bound 40 nm gold nanoparticles were prepared by (a) boil deposition on (b) Si, (c) polished steel, and (d) GaAs substrates.

5.2.1 Amplitude-Modulation AFM

Amplitude-modulation AFM (AFM), already introduced in Section 2.8.1, is the most common implementation of the dynamic AFM in commercial ambient AFM systems. In the AM-AFM operation, the amplitude of an oscillating cantilever is used as the input signal for a z scanner feedback loop, with the goal of maintaining a constant tip-sample rest separation z_c [Fig. 5.3(a)]. The dynamic response of the cantilever is obtained before engaging the surface by driving the cantilever with a dither piezo and recording the cantilever response—the oscillation amplitude and phase. The operator chooses a suitable operation frequency f around the resonance frequency f_R and defines the setpoint amplitude A_{set} [Fig. 5.3(b)]. The feedback loop, once turned on, attempts to maintain the amplitude A at A_{set} by controlling the z scanner position. Hence the AM-AFM operation involves multiple parameters—the operation frequency f , the initial amplitude A_o (which is varied by the dither piezo signal), and the setpoint amplitude A_{set} . The multiple-parameter nature makes the AM-AFM trickier to operate than the contact AFM.

5.2.2 Experiment

Sample Preparation and Imaging

40 nm gold nanoparticles were dispersed on silicon (Si), polished steel, and gallium arsenide substrates from a gold colloid solution by the boil deposition method described in Section 3.4 (Fig. 5.4). The samples were then cleaned in a plasma cleaner (using argon gas at 0.5 mbar), with the intention of removing any organic molecules used for the steric stabilization of the gold colloid. The samples were then imaged by AM-AFM

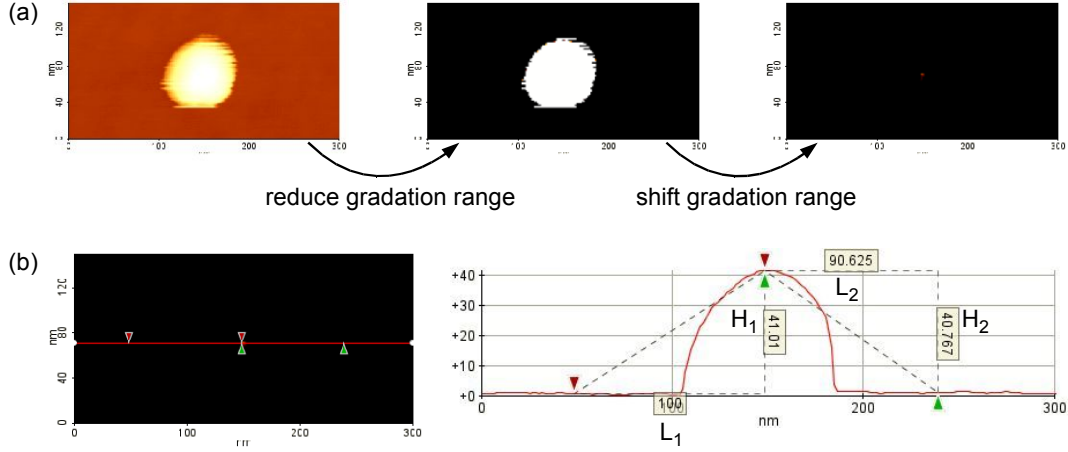


Figure 5.5: (a) The apex of a surface-bound nanoparticle is located by scaling and shifting the gradation range in the AFM image analysis software. (b) The line cross section, parallel to the fast scan direction, is then analyzed to measure the nanoparticle height. Using two reference points yielded the most precise results. In this case, the measured height is $(90.625 \times 41.010 \text{ nm} + 100.000 \times 40.767 \text{ nm}) / (90.625 + 100.000) = 40.883 \text{ nm}$.

using various imaging parameters. Nanosensors NCL cantilevers with sharp pyramidal PPP tips were used as probes.

Height Measurement

The AFM images were analyzed using the XEI software provided by Park Systems. The apex of the nanoparticle was found by varying the coloring parameters [Fig. 5.5(a)], and then a line cross section through the apex was then used to calculate the apex height, using two reference points [Fig. 5.5(b)].

When the height difference with respect to the reference point 1 located L_1 to the left of the apex is H_1 and the height difference with respect to the reference point 2 located L_2 to the right of the apex is H_2 [Fig. 5.5(b)], the weighted average of the nanoparticle height is $(L_2 \times H_1 + L_1 \times H_2) / (L_1 + L_2)$. This method was found to be more precise than using a single reference point, as the thermal drift and the sample slope are compensated for. It was important to use reference points reasonably far away from the nanoparticle, to avoid the effect of the piezoelectric creep.

5.2.3 Dependence on the Initial Amplitude

The measured height of a nanoparticle was found to vary with the initial amplitude A_0 . The results for a silicon-wafer-bound gold nanoparticle are shown in Fig. 5.6. AM-AFM images were acquired with different initial amplitudes A_0 over the range of 5.4–19.2 nm, and with the setpoint amplitude A_{set} at 5.0 nm and the operation frequency f at 167.25 kHz. The cantilever resonance frequency f_R was measured to be

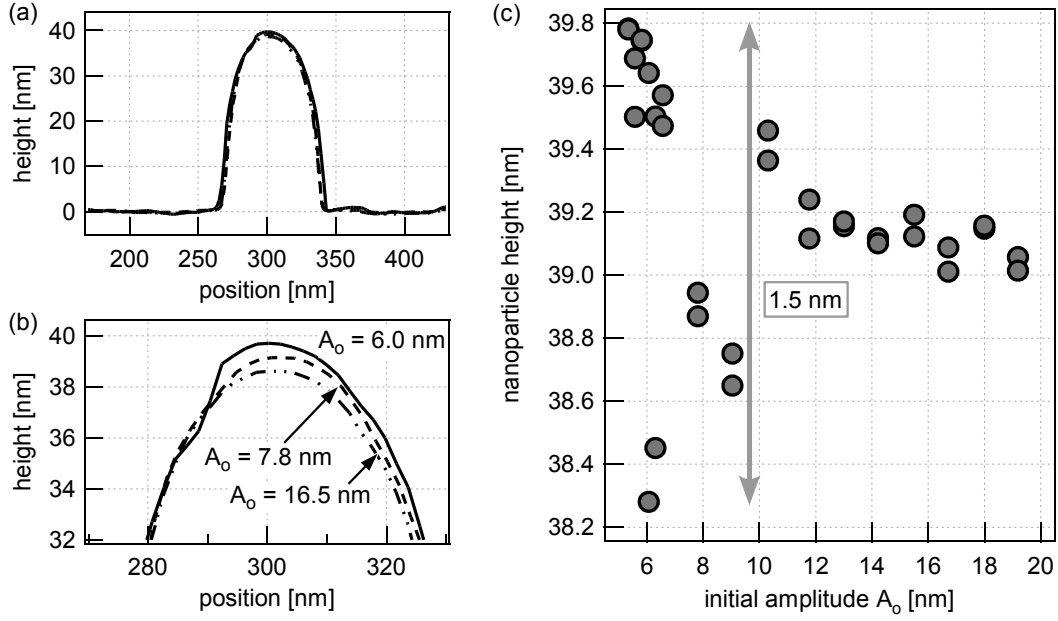


Figure 5.6: AM-AFM images of a Si-wafer-bound gold nanoparticle were acquired with different initial amplitudes and compared. (a) The line cross sections of 3 different images at the nanoparticle apex appear nearly identical, (b) but a closer inspection shows a variation in the apex height. (c) The measured height is in the range of 38.3–39.8 nm, depending on the initial amplitude A_o .

167.16 kHz, with the quality factor Q at 600. The tip radius R_t was estimated to be 12 nm. The relative humidity RH was at 25%, and the temperature T was at 25 °C. The measured nanoparticle height varies with the initial amplitude, but the dependence is not monotonic, nor does it suggest a polynomial dependence [Fig. 5.6(c)]. The height variation can be as large as 1.5 nm.

The results for a gold nanoparticle bound on a polished steel substrate are shown in Fig. 5.7. AM-AFM images were acquired at a constant A_{set} of 5.0 nm, with A_o values over the range of 5.8–26.1 nm. Other parameters and conditions were identical to the case of the silicon-wafer-bound gold nanoparticle. The measured height of the stainless-steel-bound gold nanoparticle varies with the initial amplitude, and again the behavior is complex [Fig. 5.7(c)]. Furthermore, the graph is not similar to that of the silicon-bound nanoparticle Fig. 5.6(c)]. The apparent height varies over a wider range, with the maximum difference reaching 3.3 nm.

5.2.4 Dependence on the Setpoint Amplitude

The measured height of a surface-bound gold nanoparticle was also found to vary with the setpoint amplitude A_{set} . Shown in Fig. 5.8 are the results for a gallium-arsenide-wafer-bound gold nanoparticle. AM-AFM images were acquired with A_{set} varying over the range of 2.5–7.0 nm. The imaging parameters were $A_o = 9.4$ nm and $f = 167.82$ kHz.

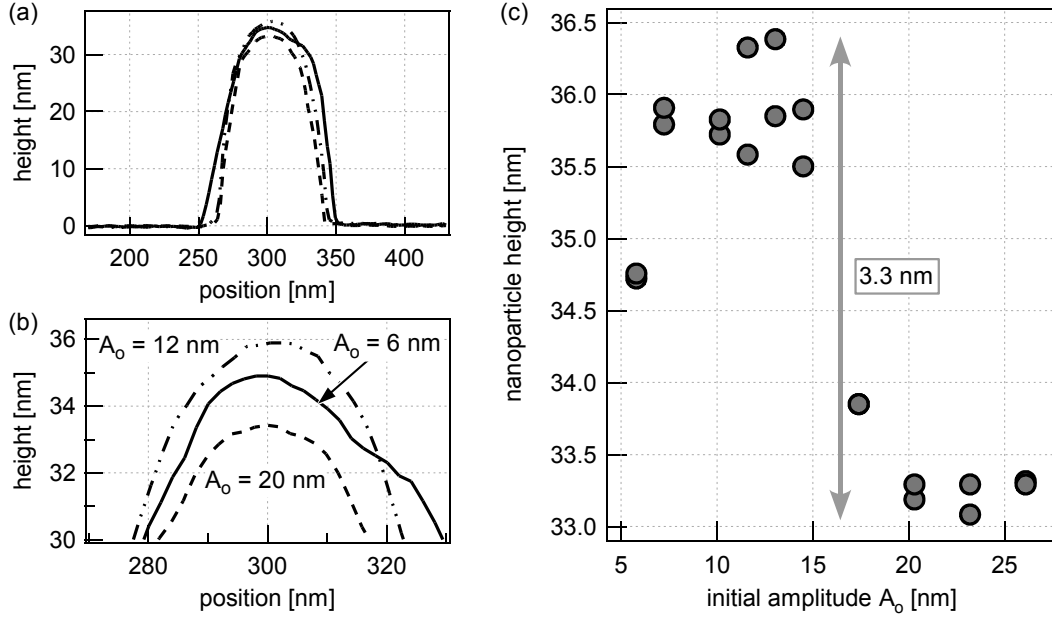


Figure 5.7: AM-AFM images of a stainless-steel-bound gold nanoparticle were acquired with different initial amplitudes and compared. (a) The line cross sections of 3 different images at the nanoparticle apex appear similar, (b) but a closer inspection shows a variation in the apex height. (c) The measured height is in the range of 33.1–36.4 nm, depending on the initial amplitude A_o .

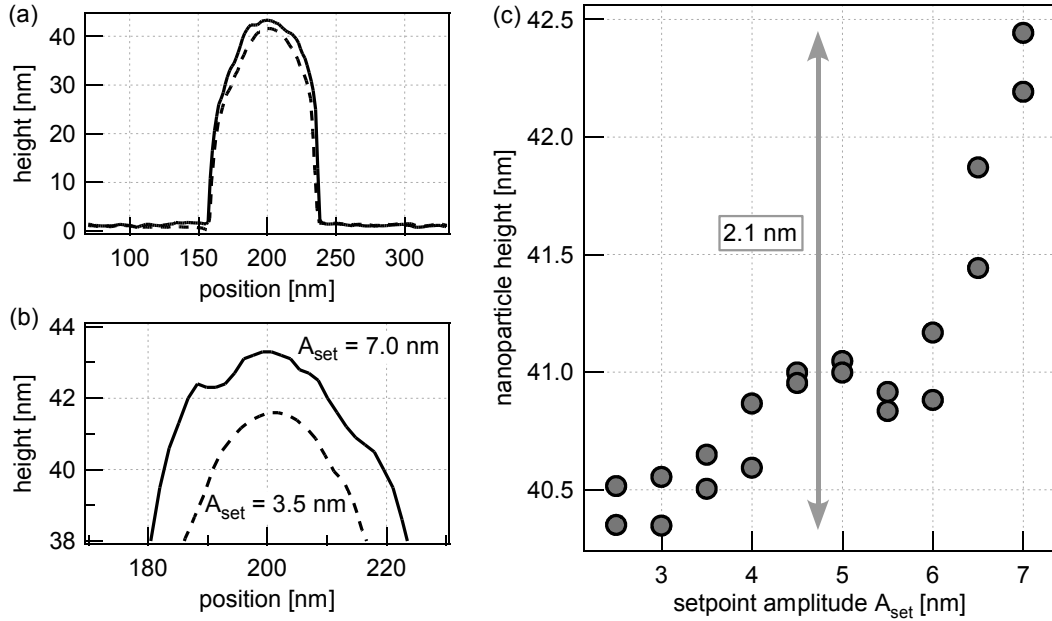


Figure 5.8: AM-AFM images of a GaAs-wafer-bound gold nanoparticle were acquired with different setpoint amplitudes A_{set} and compared. (a), (b) The line cross sections of 2 images at different A_{set} values a difference in the nanoparticle apex height. (c) The measured height is in the range of 40.3–42.4 nm, depending on A_{set} .

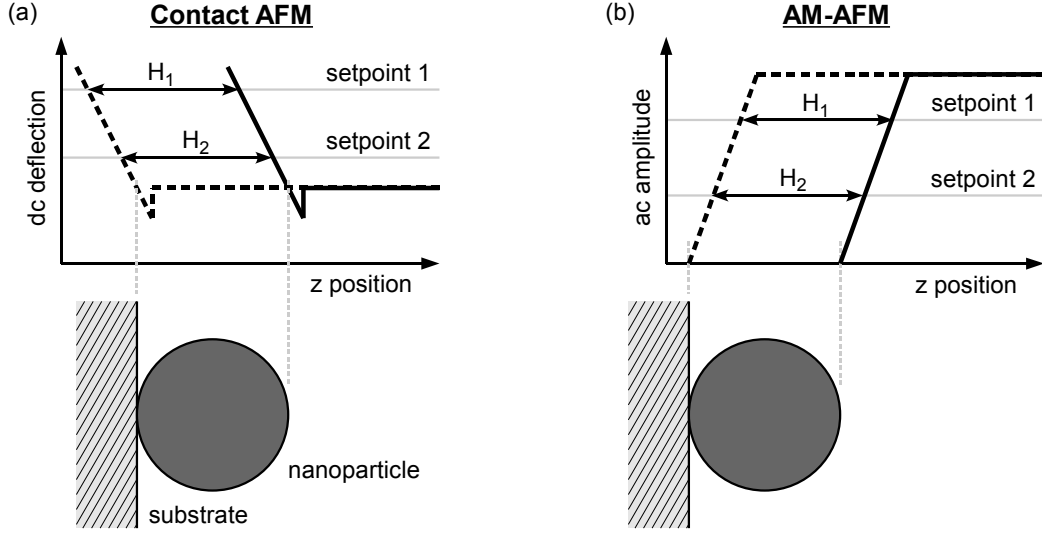


Figure 5.9: (a) In contact AFM, the force curve on the nanoparticle is shifted relative to the curve on the substrate, and the position shift is equal to the particle height. If the sample deformation is negligible, the measured height is independent of the cantilever's dc deflection. (b) The measured height of a nanoparticle would be setpoint-independent only if the amplitude–distance curves have an identical form on both the substrate and the particle.

The conditions were $f_R = 167.82$ kHz, $Q = 600$, $R_t = 12$ nm, $RH = 20\%$, and $T = 20^\circ\text{C}$. The measured nanoparticle height appears to increase with A_{set} . The height variation over the measured range was 2.1 nm.

5.3 Experimental Amplitude–Phase–Distance (APD) Curves

5.3.1 Why are APD Curves Important?

Before investigating the cause of height measurement anomalies in dynamic AFM, it is insightful to first understand the principle behind the contact AFM height measurement. Imagine that force (dc deflection)–displacement curves are acquired on a substrate and then on a substrate-bound nanoparticle, as depicted in Fig. 5.9(a). The force curves exhibit a shift in the z position due to the nanoparticle height. When contact AFM images are obtained at two different setpoints 1 and 2, the measured values of the nanoparticle height will be H_1 and H_2 , respectively. If both the nanoparticle and the substrate are much stiffer than the AFM cantilever, the force curve will have the same contact slope on both the substrate and the particle, and therefore H_1 will be equal to H_2 . The measured nanoparticle height will be constant, independent of the dc deflection setpoint.

In expecting the measured particle height to be constant independent of the AM-AFM parameters, we have implicitly assumed that the dynamic AFM amplitude–

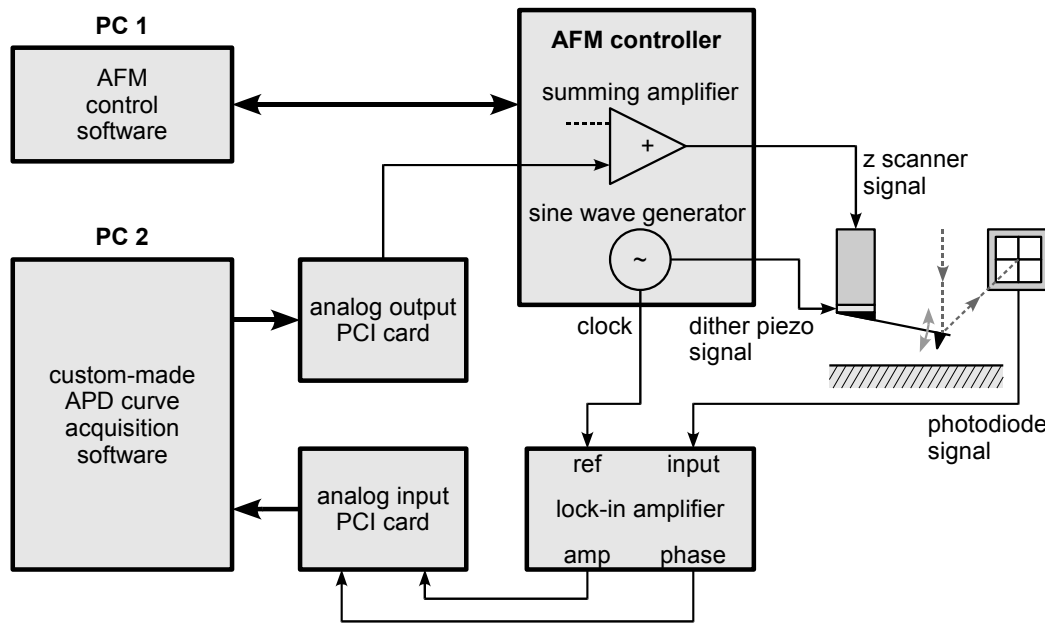


Figure 5.10: A custom solution for the amplitude–phase–distance curve acquisition was realized by using PC data acquisition cards, an external lock-in amplifier, and by hacking the controller electronics.

distance curves behave similarly. If the amplitude–distance curves behave as illustrated in Fig. 5.9(b), i.e. the oscillation amplitude decreases in an identical fashion on both the substrate and the nanoparticle, then H_1 and H_2 , again the measured values of the nanoparticle height at two different setpoints, will be equal.

The contrapositive is thus true. The height measurement anomalies in AM-AFM indicate that the amplitude–distance curves must not be so simple.

5.3.2 Instrumentation

The data acquisition software provided by the AFM manufacturer did not support amplitude–distance curves. Therefore a custom solution was realized using an external lock-in amplifier and PC data acquisition cards. The schematics of the instrumentation are shown in Fig. 5.10. The controller electronics was modified to control the z scanner piezo with a signal from a data acquisition card.

The software “AmplitudeCurve.exe” was built using Borland C++ Builder 6. The user interface is shown in Fig. 5.11. In addition to the amplitude and phase signals from the external lock-in amplifier, the software also collects the laser intensity signal, the dc deflection signal, the lateral force signal, and the z detector signal. Some notable features of the software are:

Amplitude limiter Upon reaching a predefined setpoint for the amplitude, the z scanner retracts. Tip damage could be prevented by avoiding extremely low setpoints.

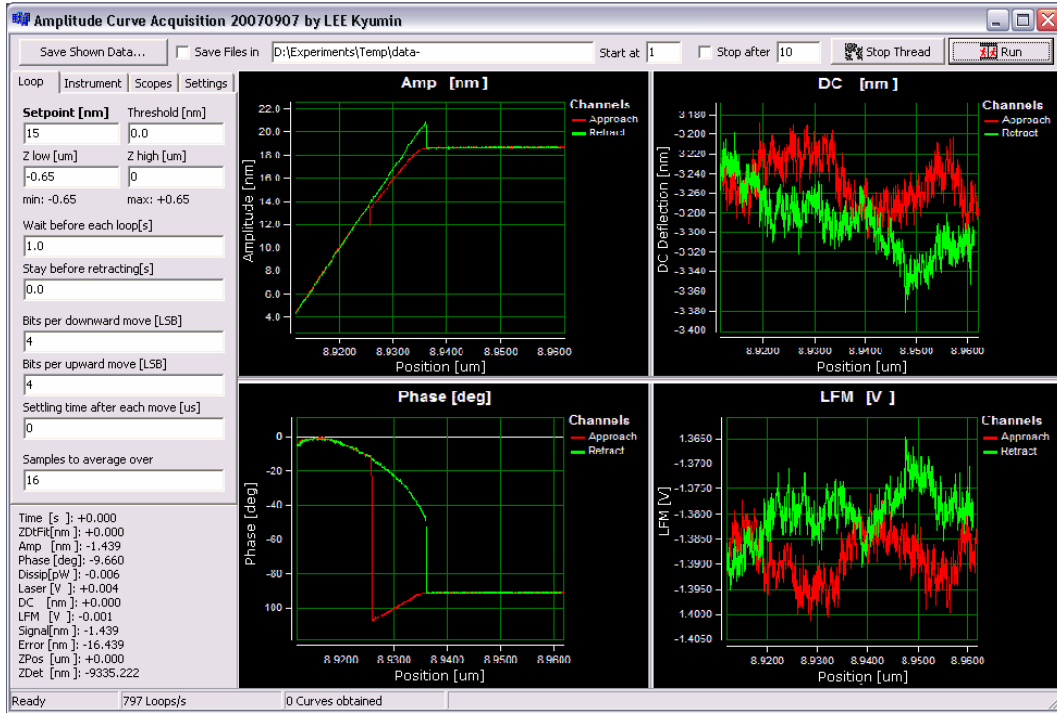


Figure 5.11: A screen capture of the “AmplitudeCurve” software

Z detector fitting After each approach–retract cycle, the z detector data is regressed as a second-order polynomial of the z scanner voltage¹, to eliminate the signal noise. The result of the fit proved to be more reliable than the z scanner voltage data or the raw z detector data.

Automatic data save The data are saved as a text file automatically after each cycle, in a predefined directory.

The data acquisition functions are isolated into a single file. Should the need to change the data acquisition instrument arise, only this file needs to be rewritten.

5.3.3 Results

Using the AmplitudeCurve software, amplitude–distance and phase–distance curves were acquired on different substrates and also on the apexes of substrate-bound gold nanoparticles. The phase value is defined with respect to the dither piezo signal. When the dither piezo is driven by a sinusoidal signal $V_d \cos(2\pi f t)$, the cantilever deflection shows the response $A \cos(2\pi f t - \phi)$, where A and ϕ are the amplitude and the phase of cantilever oscillation, respectively. Figure 5.12 shows sample amplitude–distance and phase–distance curves, obtained on a silicon wafer. It should first be noticed that the approach and retract curves contain jumps, and that they occur at different

¹ A higher-order regression is possible, but the second-order regression already gives satisfactory results.

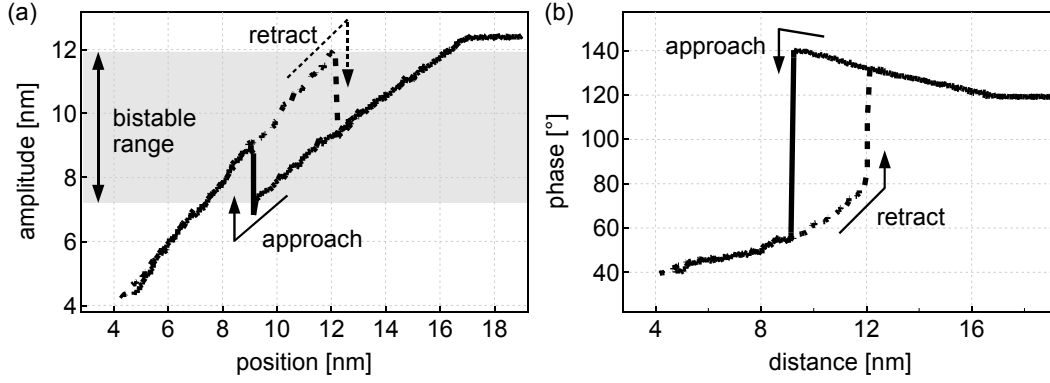


Figure 5.12: Sample (a) amplitude–distance and (b) phase–distance curves acquired on a Si substrate

positions, resulting in a hysteresis. The jumps, however, did not always occur at the same positions when the curves were repeated.

The amplitude–phase–distance (APD) curves obtained on a gold nanoparticle–silicon wafer (Au–Si) system, a gold nanoparticle–steel substrate (Au–SS) system, and a gold nanoparticle–gallium arsenide wafer (Au–GaAs) system are shown in Fig. 5.13. The APD curves on the gold nanoparticles are in general similar to those obtained on the substrates, but there are notable differences. Most importantly, the slopes are slightly different—most pronounced for the Au–SS system [Fig. 5.13(b)]—and the position gaps in the bistable regions are different in magnitude—most pronounced in the Au–Si system [Fig. 5.13(a)]. These characteristics would all contribute to the height measurement anomalies.

To proceed further, we need a theoretical model to explain the various aspects of APD curves.

5.4 Dynamic AFM Simulation

The basics of the dynamic-AFM simulation were introduced in Section 2.8.3, but for the purpose of this chapter, both the model and the simulation process need to be explained in greater detail. The model and the nomenclature are similar to those used by Garcia et al. [142].

5.4.1 Mass–Spring Model

The tip–sample system is treated as a mass on a spring oscillating near a surface (Fig. 5.14). The equation of motion of the system is

$$m^* \frac{d^2 z}{dt^2} + \frac{2\pi m^* f_R}{Q} \frac{dz}{dt} + k z = F_d(t) + F_{ts}(s), \quad (5.1)$$

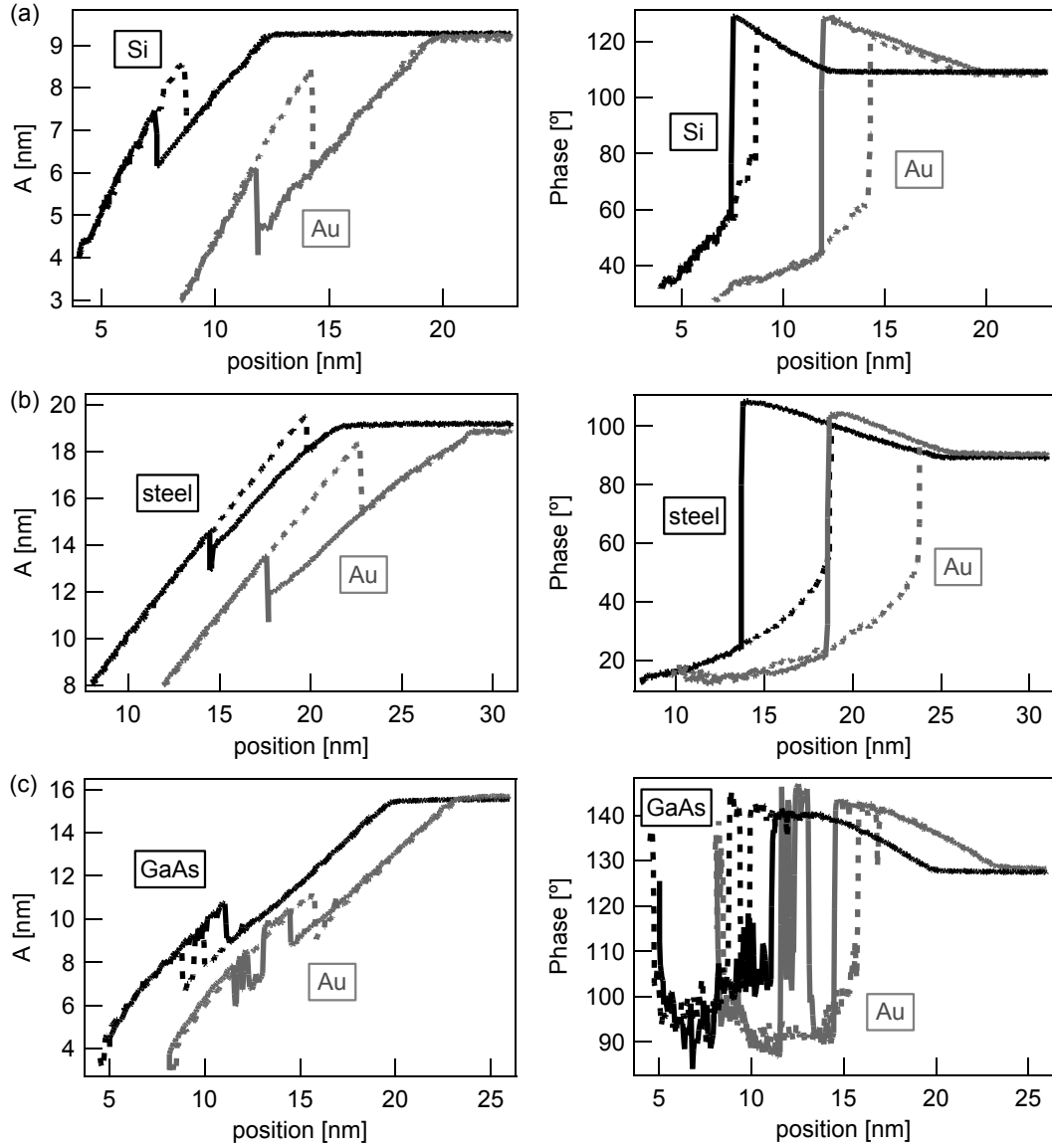


Figure 5.13: Amplitude–distance (left) and phase–distance (right) curves on (a) a gold nanoparticle–Si wafer (Au–Si) system, (b) a gold nanoparticle–polished steel substrate (Au–SS) system, and (c) a gold nanoparticle–GaAs wafer (Au–GaAs) system. The solid lines are the approach curves, and the dashed lines are the retract curves. The APD curves on the gold nanoparticles have been shifted 4 nm to the right for better visibility.

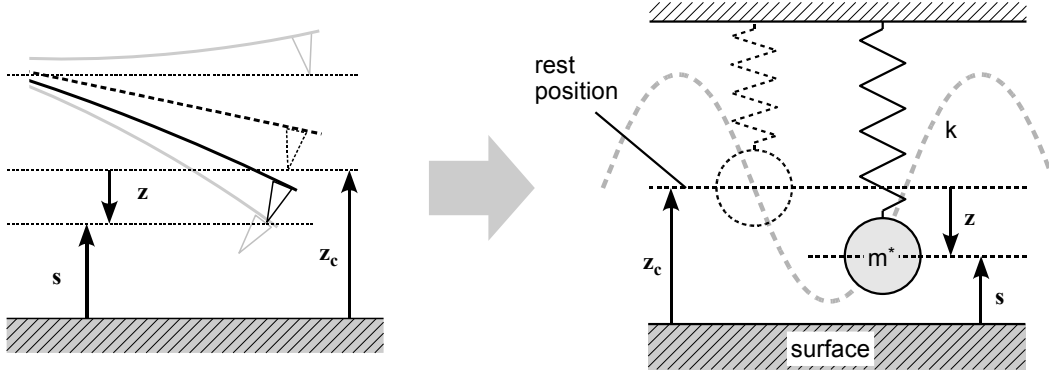


Figure 5.14: The oscillating tip in dynamic AFM is modeled as a mass on a spring.

where m^* is the effective mass of the cantilever, f_R is the resonance frequency, Q is the quality factor of the dynamic response, and k is the cantilever spring constant. z is the instantaneous displacement from the rest position, and s is the instantaneous tip-sample separation. z and s are related by $z_c + z = s$, where z_c is the tip-sample separation at rest (Fig. 5.14).

$F_d(t)$ is the sinusoidal driving force described by

$$F_d = F_o \cos(2\pi f t), \quad (5.2)$$

with the driving amplitude F_o and the driving frequency f . Strictly, as the cantilever in our AFM is modulated using a dither piezo, an oscillation in the tip-sample rest separation z_c is inevitable. However, as our system has a high quality factor (always greater than 500) and as the system is driven near the resonance frequency, the oscillation in z_c value is roughly $1/Q$ times the oscillation amplitude, which is negligible in practice.

$F_{ts}(s)$ is the tip-sample interaction force that is described by the following set of equations.

$$F_{ts}(s) = \begin{cases} F_{vdW}(s) & \text{in contact,} \\ F_{ad} + F_{ct}(s) & \text{not in contact,} \end{cases} \quad (5.3)$$

where F_{vdW} is the attractive van der Waals force, $F_{ct}(s)$ is the force generated by contact, and F_{ad} is the adhesion force. Whether the tip is in contact with the surface or not depends on the tip separation s .

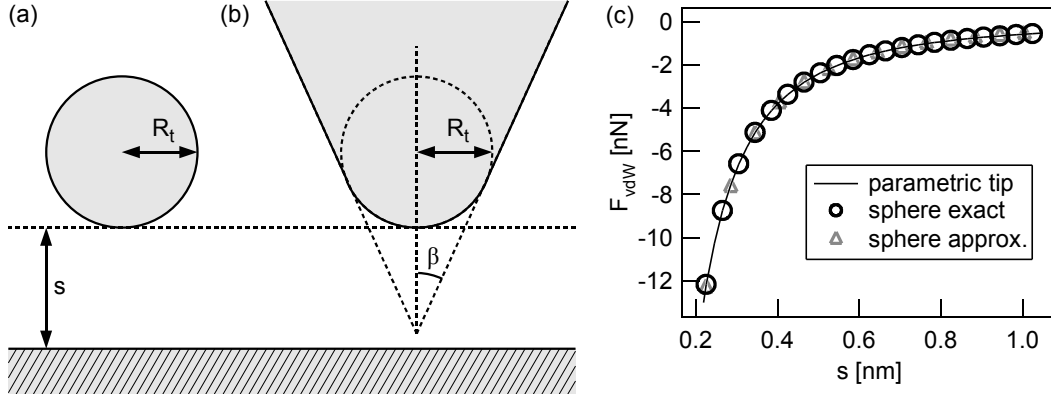


Figure 5.15: The tip and the sample can be modeled as either (a) a sphere and a plane (exact: Eq. 5.5; approximation: Eq. 5.6), or (b) a cone with spherical cap and a plane (Eq. 5.7) [143]. (c) For the relevant dimensions and constant values, however, all three equations—Eq. 5.7: solid line; Eq. 5.5: circles; Eq. 5.6: triangles—give very close values. Parameters for the curves: $H = 250 \text{ zJ}$; $R_t = 15 \text{ nm}$; $\beta = 10^\circ$.

5.4.2 van der Waals Force

The van der Waals force arises from the interaction of oscillating dipoles [144]. The van der Waals interaction potential between a pair of molecules is

$$w(d) = -\frac{C_{disp}}{d^6}, \quad (5.4)$$

where C_{disp} is the interaction constant as defined by London [145]. Hamaker [146] undertook the task of calculating the van der Waals force between surfaces, and the force between a sphere and a plane [Fig. 5.15(a)] was found to be

$$F_{vdW}(s) = -\frac{2 H R_t^3}{3 s^2 (s + 2 R_t)^2}, \quad (5.5)$$

where H is the Hamaker constant defined as $\pi^2 C_{disp} \rho_t \rho_s$ (ρ_t and ρ_s are the number densities of the sphere and the plane materials, respectively), R_t is the sphere radius, and s is the separation. In the case where $R_t \gg s$, Eq. 5.5 can be approximated to

$$F_{vdW}(s) = -\frac{H R_t}{6 s^2}. \quad (5.6)$$

As the real AFM tip is not a sphere, Argento and French [143] proposed a parametric tip model where the tip is modeled as a cone with a spherical cap [Fig. 5.15(b)]. They calculated the parametric tip–plane van der Waals force to be

$$F_{vdW}(s) = \frac{-H R_t^2 (1 - \sin \beta) [R_t (1 - \sin \beta) + s (1 + \sin \beta)]}{6 s^2 [s + R_t (1 - \sin \beta)]^2} + \frac{-H \tan \beta [s \sin \beta + R_t (\sin \beta + \cos 2\beta)]}{6 \cos \beta [s + R_t (1 - \sin \beta)]^2}. \quad (5.7)$$

When the van der Waals forces were calculated for the realistic values of H , R_t , and β , however, both Eq. 5.5 and Eq. 5.6 gave results very close to that obtained by Eq. 5.7. As Eq. 5.7 is significantly more computation-intensive than the other two equations, Eq. 5.5 was used in the computer simulation of the dynamic AFM.

5.4.3 Contact Force and Adhesion Force

The DMT (Derjaguin–Müller–Toporov) contact mechanics was used to model the contact force. An intermolecular spacing a_o is defined, and the tip is assumed to be in contact with the surface if $s \leq a_o$ and not in contact if $s > a_o$. The typical value is 0.165 nm. The contact force F_{ct} is given by

$$F_{ct}(s) = K \sqrt{R_t} \delta_k^{\frac{3}{2}}, \quad (5.8)$$

where δ_k and K are the contact deformation and the reduced elastic modulus, respectively. K is calculated from

$$\delta_k = a_o - s, \quad (5.9)$$

$$\frac{1}{K} = \frac{3}{4} \left(\frac{1 - \nu_t^2}{E_t} + \frac{1 - \nu_s^2}{E_s} \right), \quad (5.10)$$

where E_t and E_s are the elastic moduli of the tip and the sample, respectively, and ν_t and ν_s are the Poisson ratios of the tip and the sample, respectively.

The adhesion force F_{ad} ($= -2\pi R_t W$, where W is the work of adhesion per unit area) is identified with the van der Waals force at $s = a_o$ [142].

$$F_{ad} = F_{vdW}(a_o). \quad (5.11)$$

Combining Eq. 5.3 with Eq. 5.5, Eq. 5.8, and Eq. 5.11, we obtain

$$F_{ts}(s) = \begin{cases} -\frac{2H R_t^3}{3s^2(s+2R_t)^2} & \text{if } s > a_o, \\ -\frac{2H R_t^3}{3a_o^2(a_o+2R_t)^2} + K \sqrt{R_t} (a_o - s)^{\frac{3}{2}} & \text{if } s \leq a_o. \end{cases} \quad (5.12)$$

5.4.4 Algorithm and Software

Algorithm

For the computer simulation of the dynamic AFM, normalized time τ ($= f t$) was used for convenience. Equation 5.1 then becomes

$$m^* f^2 \frac{d^2 z}{d\tau^2} + \frac{2\pi m^* f_R f}{Q} \frac{dz}{d\tau} + k z = F_d(\tau) + F_{ts}(s), \quad (5.13)$$

and rearranging the equation gives

$$\frac{d^2 z}{d\tau^2} = -\frac{k}{m^* f^2} z + -\frac{2\pi f_R}{Q} \frac{dz}{f d\tau} + \frac{1}{m^* f^2} [F_d(\tau) + F_{ts}(s)]. \quad (5.14)$$

This second-order differential equation can be divided into two first-order differential equations by introducing the normalized velocity v .

$$\frac{dz}{d\tau} = v \quad (5.15)$$

$$\frac{dv}{d\tau} = -\frac{k}{m^* f^2} z + -\frac{2\pi f_R}{Q} \frac{v}{f} + \frac{1}{m^* f^2} [F_d(\tau) + F_{ts}(s)]. \quad (5.16)$$

The pair of equations Eq. 5.15 and Eq. 5.16 are in the form

$$\frac{dz}{d\tau} = p(\tau, z, v), \quad (5.17)$$

$$\frac{dv}{d\tau} = q(\tau, z, v), \quad (5.18)$$

and this system of equations can be solved numerically by the fourth-order Runge–Kutta method [147]. To be specific, the oscillation period T_{osc} ($= 1/f$) is divided into N points, so that $\tau_0 = 0$, $\tau_1 = h$, $\tau_2 = 2h$, \dots , and $\tau_{N-1} = (N-1)h$, with $h = 1/N$. For each time pixel τ_i , the corresponding displacement z_i and the velocity v_i are then calculated by

$$z_{i+1} = z_i + \frac{1}{6}(k_1 + 2k_2 + 2k_3 + k_4), \quad (5.19)$$

$$v_{i+1} = v_i + \frac{1}{6}(l_1 + 2l_2 + 2l_3 + l_4), \quad (5.20)$$

where

$$k_1 = h p(\tau_i, z_i, v_i), \quad (5.21)$$

$$l_1 = h q(\tau_i, z_i, v_i), \quad (5.22)$$

$$k_2 = h p(\tau_i + h/2, z_i + k_1/2, v_i + l_1/2), \quad (5.23)$$

$$l_2 = h q(\tau_i + h/2, z_i + k_1/2, v_i + l_1/2), \quad (5.24)$$

$$k_3 = h p(\tau_i + h/2, z_i + k_2/2, v_i + l_2/2), \quad (5.25)$$

$$l_3 = h q(\tau_i + h/2, z_i + k_2/2, v_i + l_2/2), \quad (5.26)$$

$$k_4 = h p(\tau_i + h, z_i + k_3, v_i + l_3), \quad (5.27)$$

$$l_4 = h q(\tau_i + h, z_i + k_3, v_i + l_3). \quad (5.28)$$

The equations are iterated using the condition $z_{i+N} = z_i$ and $v_{i+N} = v_i$. It was found that iterating the set of equations 2000 times with $N = 900$ gave satisfactory results in almost all cases.

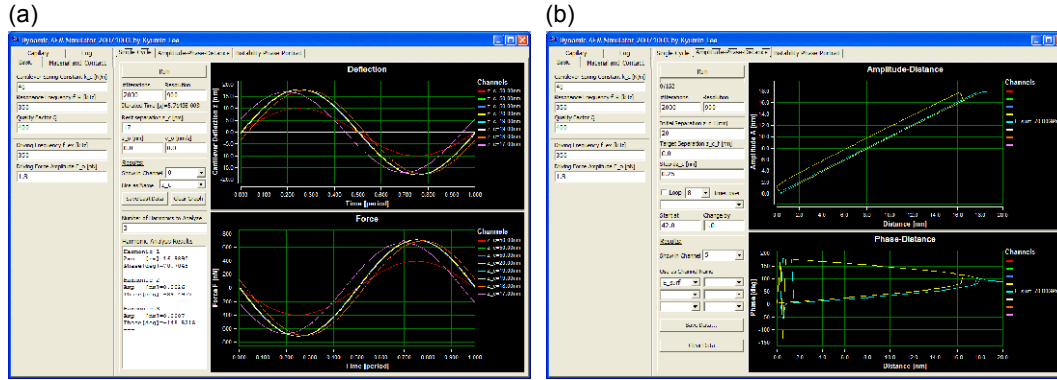


Figure 5.16: The “Dynamic AFM Simulator” software can simulate (a) an oscillation cycle at different positions, and (b) APD curves.

Software

A Windows software, titled “Dynamic AFM Simulator” was created using Borland C++ Builder 6. The software is capable of simulating an oscillation cycle at different rest positions [Fig. 5.16(a)], and simulating the APD curves [Fig. 5.16(b)]. The software source code is divided into 3 files that have the following functions.

dynafm.cpp contains the “TDynAFM” class, which implements the model and the algorithm.

dynafmthread.cpp loops the TDynAFM simulation over a user-defined z_c range, simulating the APD curves. The process runs in a separate thread.

main.cpp contains functions related to the user interface.

While dynafmthread.cpp and main.cpp are tied to the Visual Component Library by Borland, dynafm.cpp is written in standard C++ and can be reused for different user interfaces, for example, a web CGI script.

5.4.5 Non-Contact Versus Intermittent Contact

Oscillation Cycle

The Dynamic AFM Simulator could successfully reproduce both the non-contact AFM (NC-AFM) and the intermittent-contact AFM (IC-AFM). Sample z , dz/dt , s and F_{ts} cycles are shown in Fig. 5.17 for both modes, simulated for a silicon tip–silicon sample system with native oxide layers. It is important to note that the z cycles look very similar except for the phase difference. Even with the sharp positive force acting at contact, the z cycle for the intermittent-contact AFM remains sinusoidal. The second-harmonic amplitude is only 0.0039 nm, compared to the first-harmonic amplitude of 10.67 nm. As the AmplitudeCurve software acquires amplitude and phase signals, the

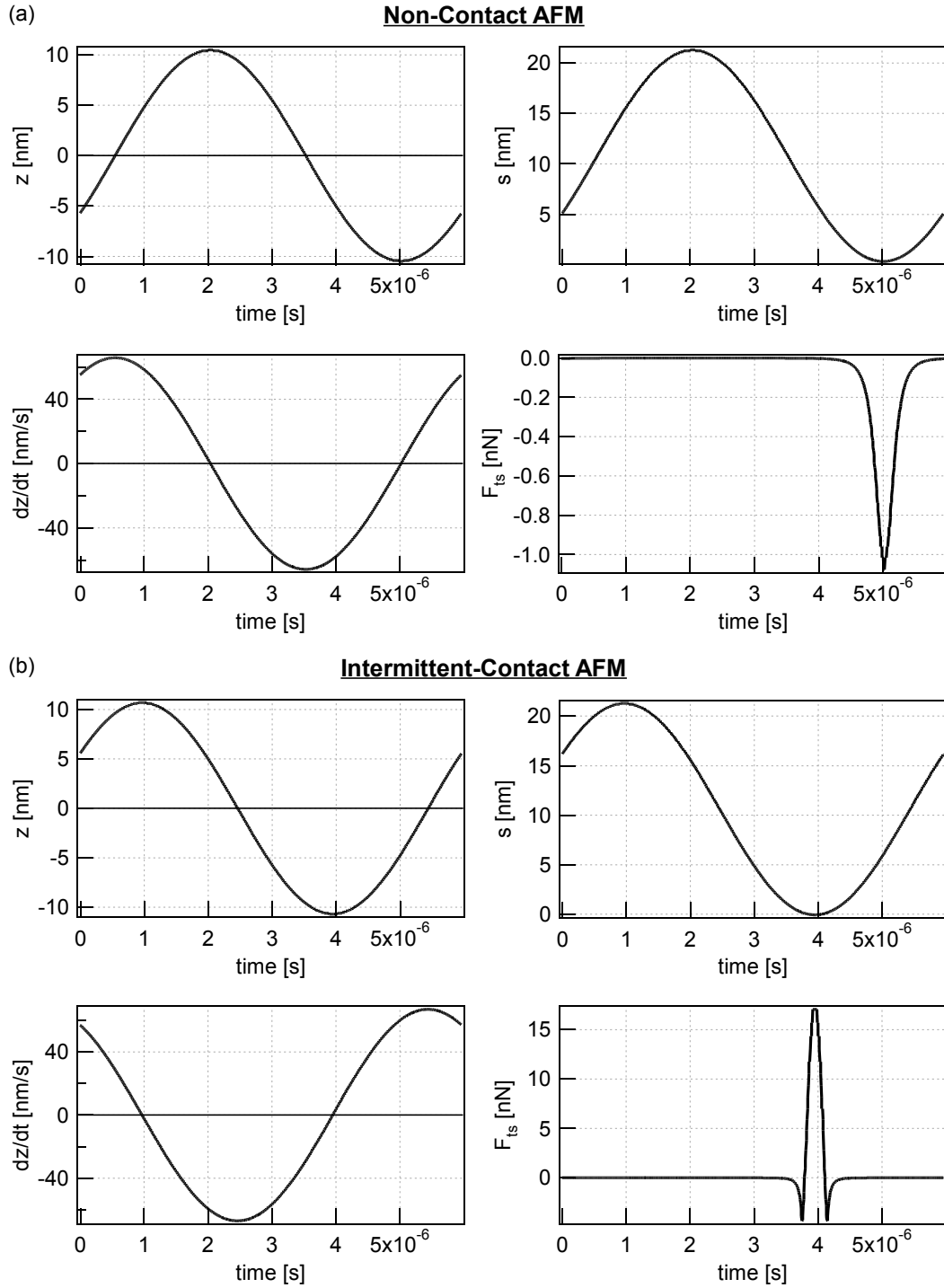


Figure 5.17: The Dynamic AFM Simulator could reproduce both (a) the non-contact AFM ($z_c = 10.8$ nm) and (b) the intermittent-contact AFM ($z_c = 10.6$ nm). The parameters were $k = 42.0$ N/m, $f_R = 167.76$ kHz, $Q = 525$, $f = 167.84$ kHz, $F_o = 1.00$ nN, $H = 65.0$ zJ, $a_o = 0.165$ nm, $R_t = 12.0$ nm, $E_t = 75.0$ GPa, $\nu_t = 0.300$, $E_s = 75.0$ GPa, and $\nu_s = 0.300$.

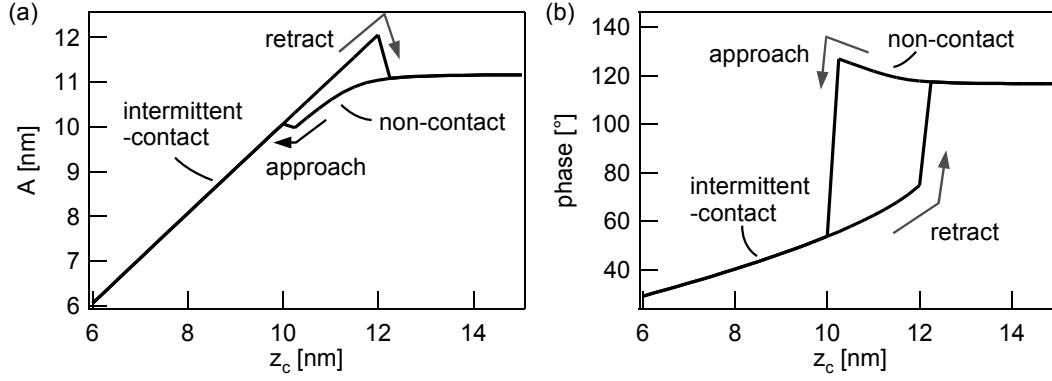


Figure 5.18: (a) Amplitude–distance and (b) phase–distance curves were simulated for the z_c range 6–15 nm, with z_c step of 0.25 nm. Parameters were identical to those used for Fig. 5.17.

phase signal can be used to decide if the tip–sample system is in the NC-AFM or the IC-AFM mode.

Amplitude–Phase–Distance Curves

The APD curves could also be simulated, by decreasing z_c step by step down to a set-point value, and then increasing z_c back to the original value. Simulation is performed at each z_c step, using the z and v data for the previous z_c step as the initial values. The amplitude and phase values are recorded at each z_c position.

Sample APD curves are shown in Fig. 5.18, again simulated for a silicon tip–silicon sample system. Characteristic features of the experimental APD curves—bistability and hysteresis—could be reproduced successfully. Again, the phase signal is useful for determining if the system is in the NC-AFM or the IC-AFM mode.

5.5 Anomalies Explained

5.5.1 Height Measurement Error due to Mode Switching

Now we have the theoretical basis to understand the height measurement anomalies. As Fig. 5.19 shows, mode switching between IC-AFM and NC-AFM on the particle and the substrate can lead to different values for the particle height. Evidently, the measured nanoparticle height with NC-AFM on the substrate and IC-AFM on the particle will be different from the height measured with NC-AFM on both the substrate and the particle. Letting H_A , H_B , H_C , and H_D denote the measured height in the cases A, B, C, and D shown in Fig. 5.19(b), respectively, we see that $H_B > H_A$, $H_D > H_C$.

While Fig. 5.19 has been drawn for the case of the height dependence on the the setpoint amplitude A_{set} , similar mode switching can occur by varying the initial amplitude A_o . Whether the tip–sample system stays in the NC-AFM mode or jumps to

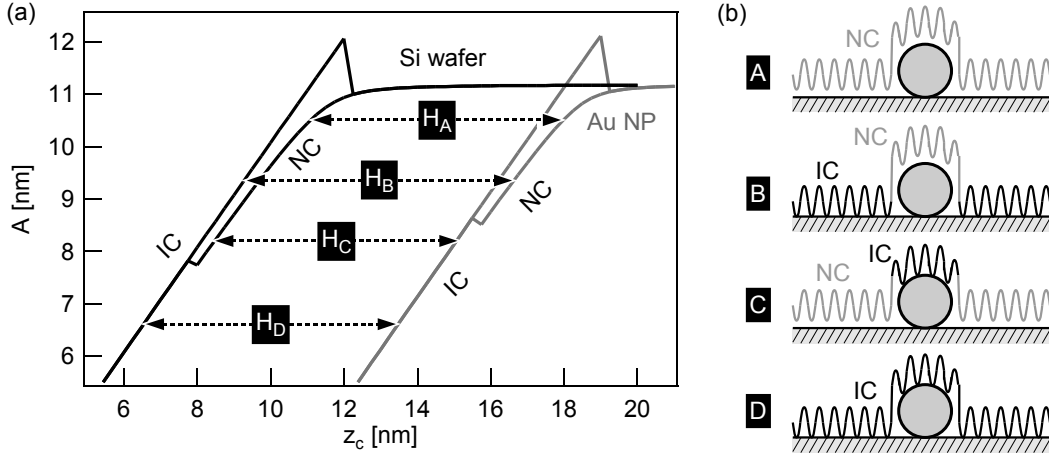


Figure 5.19: (a) The amplitude–distance bistability on the silicon substrate and the nanoparticle can lead to at 4 different height values, depending on the IC/NC-AFM mode switching. (b) A: NC-AFM on both the substrate and the particle, B: IC-AFM on the substrate and NC-AFM on the particle, C: NC-AFM on the substrate and IC-AFM on the particle, and D: IC-AFM on both the substrate and the particle.

the IC-AFM mode depends on the rest separation z_c , the initial z , and the initial v . For practical values of A_o and A_{set} , the NC-AFM mode is favored far from the surface, and the IC-AFM mode is favored near the surface [142].

We can now make sense of the height data for the surface-bound gold nanoparticles (Fig. 5.6, Fig. 5.7, and Fig. 5.8), by sorting them using the phase images. The results are shown in Fig. 5.20, Fig. 5.21, Fig. 5.22. As predicted, the $H_B > H_A$, $H_D > H_C$ relationship holds.

We also notice that the measured heights H_A in the all-NC-AFM case and H_D in the all-IC-AFM case are different, albeit the values are closer together compared to H_B and H_C . Also, the all-IC-AFM height H_D seems to vary with both A_o and A_{set} .

But why do the all-NC-AFM height H_A differ from the all-IC-AFM height H_D ? The phenomenon can be first understood from the experimental APD curves. When superposing the amplitude–distance curves on the substrate and the particle (overlapping the NC-AFM branches), the IC-AFM branches do not match and show a horizontal gap. This position gap corresponds to the difference $H_A - H_D$ (Fig. 5.23) for a given A_{set} . But why does such a gap occur? We now investigate the effect of deformation at the nanoparticle–substrate contact, and also the role of capillary forces.

5.5.2 Particle–Substrate Deformation

When APD curves were simulated ($k = 42.0$ N/m, $f_R = 167.76$ kHz, $Q = 525$, $f = 167.84$ kHz, and $F_o = 0.89$ nN) for a silicon tip with native oxide ($E_t = 75$ GPa and $\nu_t = 0.30$ for silica) on the gold nanoparticle ($H = 120$ zJ, $E_s = 78$ GPa, $\nu_s = 0.44$, $R_t = 7.5$ nm) and

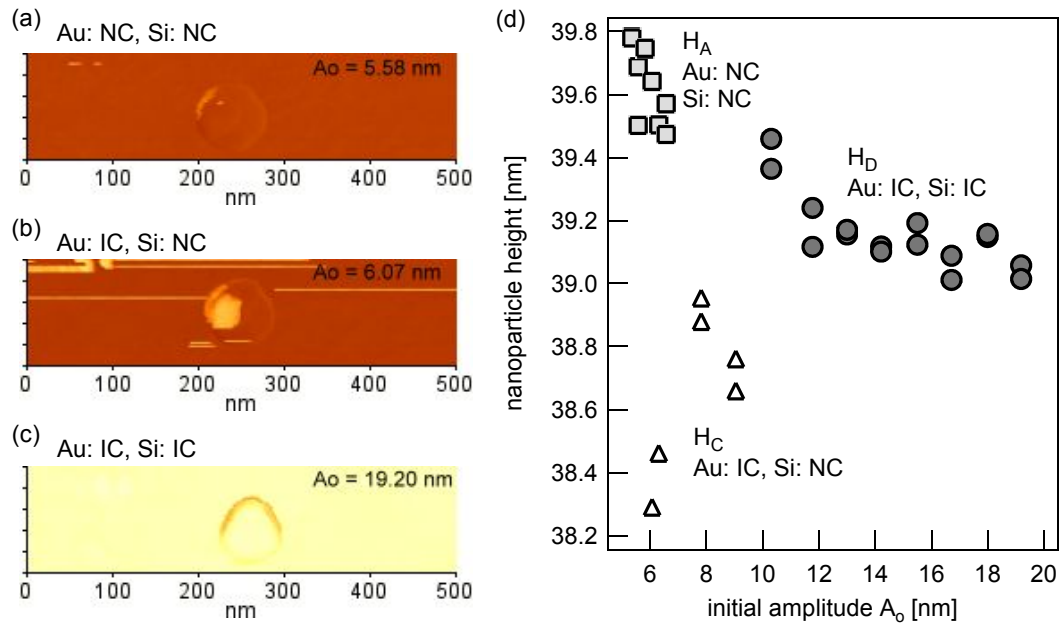


Figure 5.20: The phase images show that the tip-sample system can be in (a) the NC-AFM mode on the silicon wafer (Si) and the gold nanoparticle (Au), (b) NC-AFM on Si but in the IC-AFM mode on Au, and (c) IC-AFM on both Si and Au. (d) The height data are sorted into three groups, using the symbols introduced in Fig. 5.19.

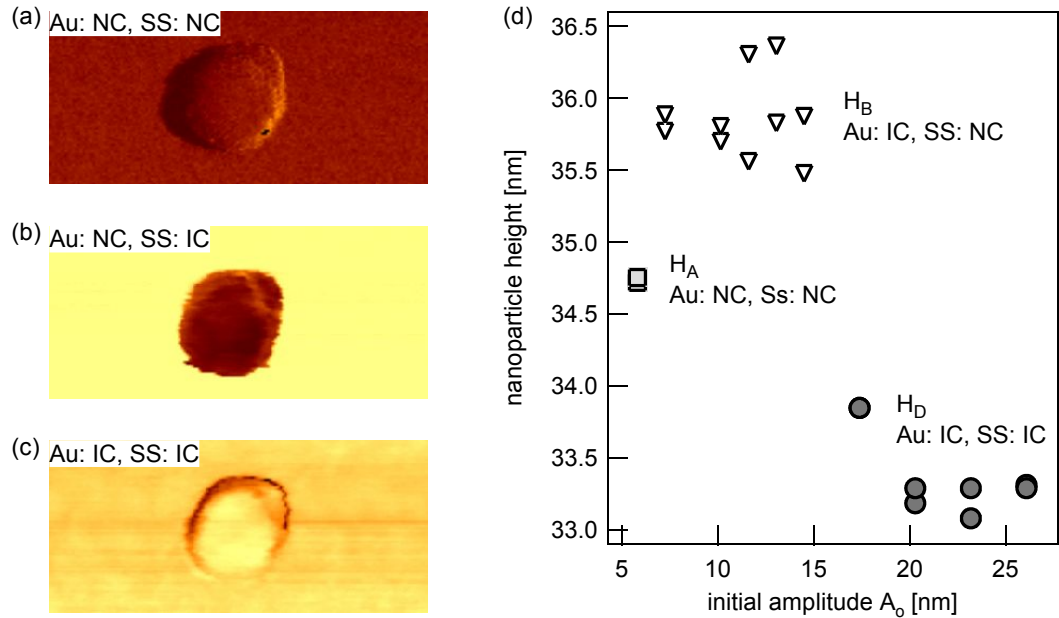


Figure 5.21: The phase images show that the tip-sample system can be in (a) the NC-AFM mode on the steel substrate (SS) and the gold nanoparticle (Au), (b) the IC-AFM mode on SS but NC-AFM on Au, and (c) IC-AFM on both SS and Au. (d) The height data are sorted into three groups.

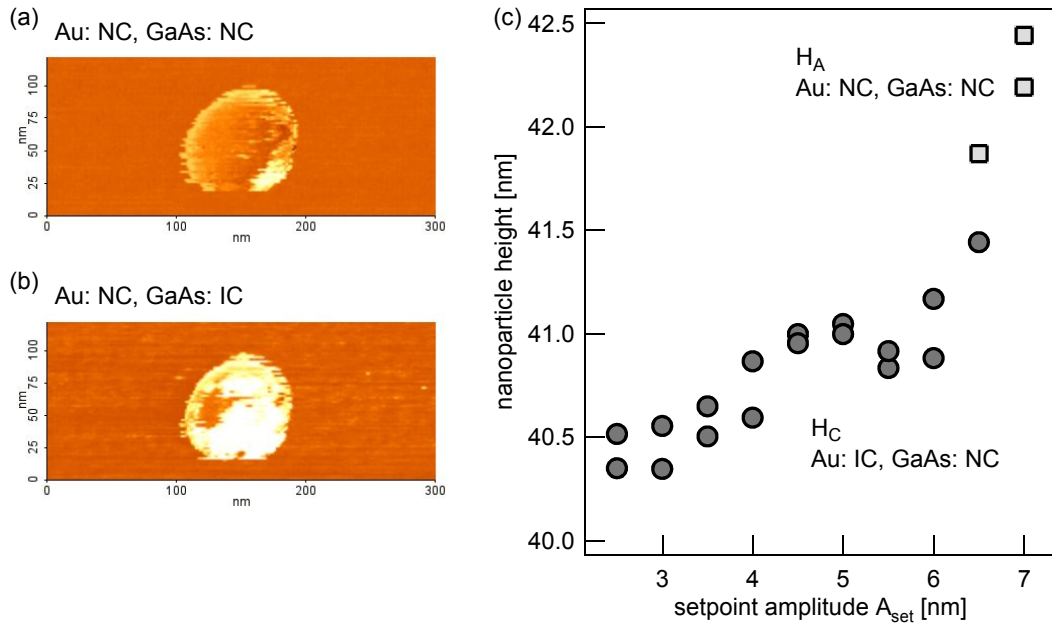


Figure 5.22: The phase images show that the tip-sample system can be in (a) the NC-AFM mode on the gallium arsenide wafer (GaAs) and the gold nanoparticle (Au), (b) NC-AFM on GaAs but the IC-AFM mode on Au, and (c) IC-AFM on both GaAs and Au. (d) The height data are sorted into two groups, using the nomenclature described in Fig. 5.19.

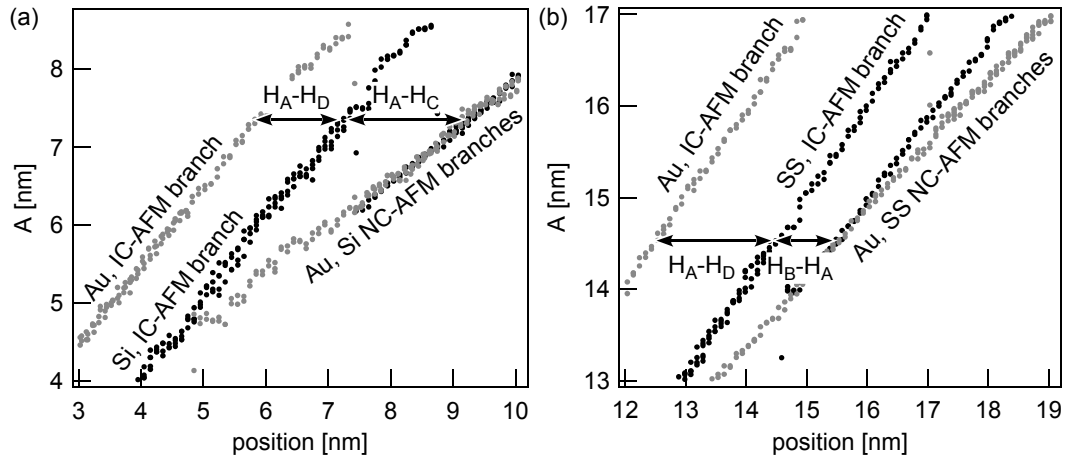


Figure 5.23: When the NC-AFM branches are superposed, the IC-AFM branches on the substrate and the particle show a gap. This gap will cause the height measurement difference $H_A - H_D$. Amplitude-distance curves are shown for (a) a gold nanoparticle (Au) on a silicon wafer (Si), and (b) a gold nanoparticle (Au) on a polished steel substrate (SS).

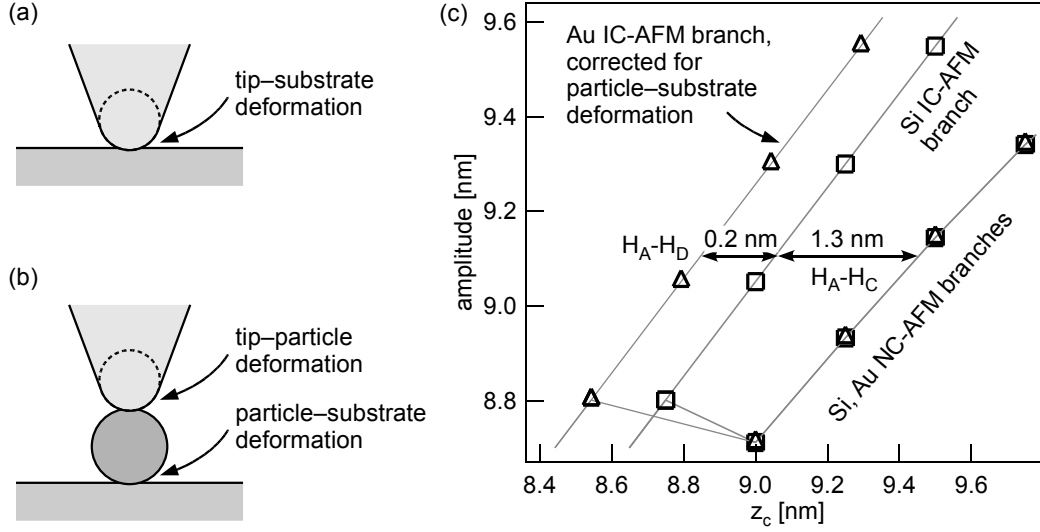


Figure 5.24: (a) With the AFM tip on the substrate, only the tip-substrate deformation needs to be accounted for. (b) On the particle, the deformation at the particle-substrate contact can be as significant as that at the tip-particle contact. (c) When corrected for the tip-particle deformation, we obtain $H_A - H_D$ and $H_A - H_C$ values similar to those observed in Fig. 5.20(b).

the silicon substrate with native oxide ($E_t = 75$ GPa, $\nu_t = 0.30$, and $R_t = 12.0$ nm), no appreciable gap could be found between the tip-on-particle and the tip-on-substrate IC-AFM branches. This was because the deformations at the tip-substrate contact and the tip-particle contact were very similar.

The simulation did not, however, include the deformation at the particle-substrate contact, which may be significant. It was found that for these conditions, which are close to those used to obtain the experimental data [Fig. 5.20(b)], the contact force is approximately 23 nN, which results in a 0.21 nm deformation at the particle-substrate contact. To the first order, we can correct the simulated tip-on-particle IC-AFM branch by shifting it 0.21 nm to the right. The result is shown in Fig. 5.24(c). After the correction, the differences $H_A - H_D$ and $H_A - H_C$ are predicted to be 0.2 nm and 1.3 nm, which fall in the ranges $H_A - H_D = 0.23$ –0.77 nm and $H_A - H_C = 0.53$ –1.50 nm observed in Fig. 5.20(b).

A similar correction could also reproduce the $H_A - H_D$ and $H_B - H_A$ gaps observed in Fig. 5.21(b).

5.5.3 Capillary Force

The capillary force from a water meniscus formed between the tip and the sample can also vary the gap between the NC-AFM and IC-AFM branches. The characteristics of the water meniscus have been rigorously studied by Stifter et al. [148], as shown in Fig. 5.25(a). In this thesis, we followed the simplified model proposed by Zitzler et

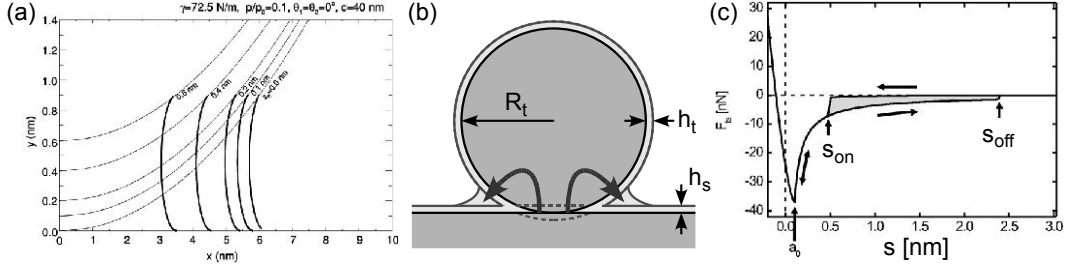


Figure 5.25: (a) The shape of liquid menisci at different conditions, according to Stifter et al. [148] (b) The simplified model and (b) the resulting hysteric capillary force described by Zitzler et al. [149] The water removed from the overlapping volume at contact forms the meniscus.

al. [149].

Water layers are assumed to be present on the tip and the sample surfaces, of thickness h_t and h_s , respectively. Upon the onset of the meniscus (occurring from $s \leq s_{on}$, with $s_{on} = h_t + h_s$), the water that is removed from the overlapping space forms the liquid meniscus [Fig. 5.25(b)]. The maximum volume of water is approximately

$$V_{men} = \frac{\pi h_t^2}{3} (3 R_t + 2 h_t) + \frac{\pi h_s^2}{3} (3 R_t - h_s), \quad (5.29)$$

and this volume determines the separation s_{off} at which the water meniscus breaks.

$$s_{off} = V_{men}^{\frac{1}{3}} - \frac{1}{5 R_t} V_{men}^{\frac{1}{3}}. \quad (5.30)$$

When the meniscus is present, the capillary force is approximated as

$$F_{cap}(s) = -\frac{4\pi \gamma^{water} R_t}{1 + 2[s/(h_t + h_s)]}, \quad (5.31)$$

where γ^{water} is the surface energy of water $(72.5 \text{ mJ/m})^2$. Due to the difference in s_{on} and s_{off} , the capillary force is hysteric.

APD curves were simulated again, with the capillary force included in the model (Fig. 5.26). As the water layers now screen the van der Waals forces, the Hamaker constant was assumed to be 5 zJ [144]. Three important characteristics are apparent. First, the gap between the NC-AFM and the IC-AFM branches depends on the onset separation s_{on} . Secondly, the point at which the amplitude starts to decrease in the NC-AFM branch is well-defined, in agreement with the experimental APD curves (Fig. 5.13. Thirdly, the jump from the NC-AFM branch to the IC-AFM branch occurs at lower z_c values, as observed in experiments.

The sample water layer thickness h_s is determined by the relative humidity as well as the surface hydrophobicity. While the silica surface is hydrophilic, the gold nanoparticle surface may still be covered with a ligand-molecule layer onto which a water layers

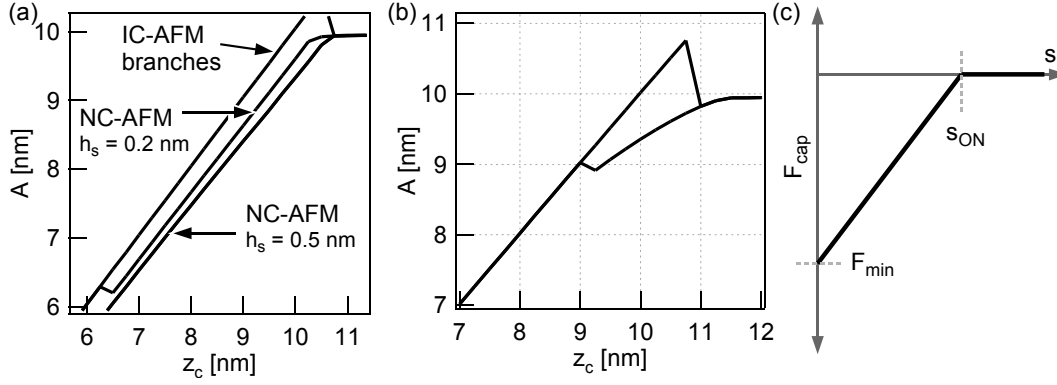


Figure 5.26: Amplitude–distance curves simulated for $h_t = 0.2$ nm and two values (0.2 nm and 0.5 nm) of h_s .

may readily condense. Hence the capillary force can also contribute to the $H_A - H_D$ difference, this time by shifting the NC-AFM branch on the particle to the right.

A qualitative difference between the experimental and simulated amplitude–distance curves still remains. We have observed experimentally that the NC-AFM branches have slopes different from the IC-AFM branches (Fig. 5.23), but the simulated NC-AFM and IC-AFM branches have very similar slopes, even when the capillary force is included. We found that the slope difference can be reproduced [Fig. 5.26(b)] by modeling the capillary force as in Fig. 5.26(c), but the theoretical basis for such modeling is weak, and it is unsure if any other force plays a role.

5.6 Comparison with Other Reported Works

While it has been known since the early years of dynamic AFM that the NC-AFM/IC-AFM bistability can cause “glitches” in AFM images [142], systematic studies on the dynamic AFM metrology are not numerous. However, a few notable works have been reported recently on the dynamic AFM size measurement of surface-bound nanoparticles.

Ebenstein et al. [150] studied the height distribution of cadmium selenide (CdSe) nanocrystals bound on surfaces chemically treated with different ligands. They found significant differences in the height distributions, and discussed that only the surface-dependent capillary force could explain the observed data. However, they offered an explanation in terms of shifting cantilever resonance curves, which is inadequate especially if the imaging was done in IC-AFM as they claimed [142]. We have shown by modeling that capillary forces can indeed cause height measurement anomalies. We believe that in Ebenstein’s case, their AFM was operating in the NC-AFM mode at least on the particles, thus experiencing different capillary forces depending on the nanoparticle capping molecules.

Mechler et al. [151] have observed the dependence of measured height on the initial

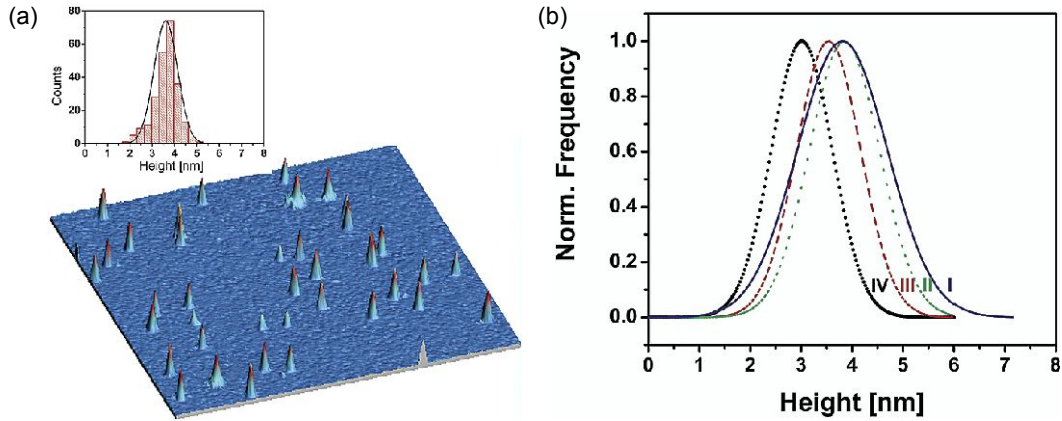


Figure 5.27: (a) Ebenstein et al. [150] carried out a statistical study on the size of surface-bound CdSe nanocrystals. (b) Gaussian fits to the height distribution histograms of nanocrystals with different capping molecules. Trace I: particles capped with mercaptoacetic acid. Trace II: dodecylamine capping. Trace III: trioctylphosphine-oxide capping. Trace IV: pyridine.

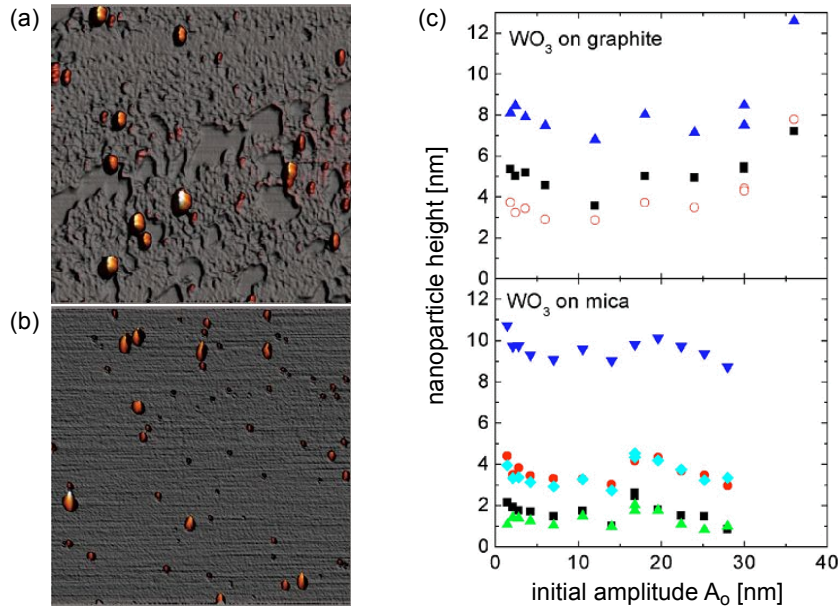


Figure 5.28: Height measurement anomalies of surface-bound WO_3 nanoparticles, as reported by Mechler et al. [151] The nanoparticles prepared on (a) graphite and (b) mica substrates were studied by dynamic AFM. (c) The measured height of nanoparticles shows a complex dependence on the initial amplitude A_0 , for both the graphite (upper graph) and the mica (lower graph) substrates. Different symbols refer to different individual particles of different sizes.

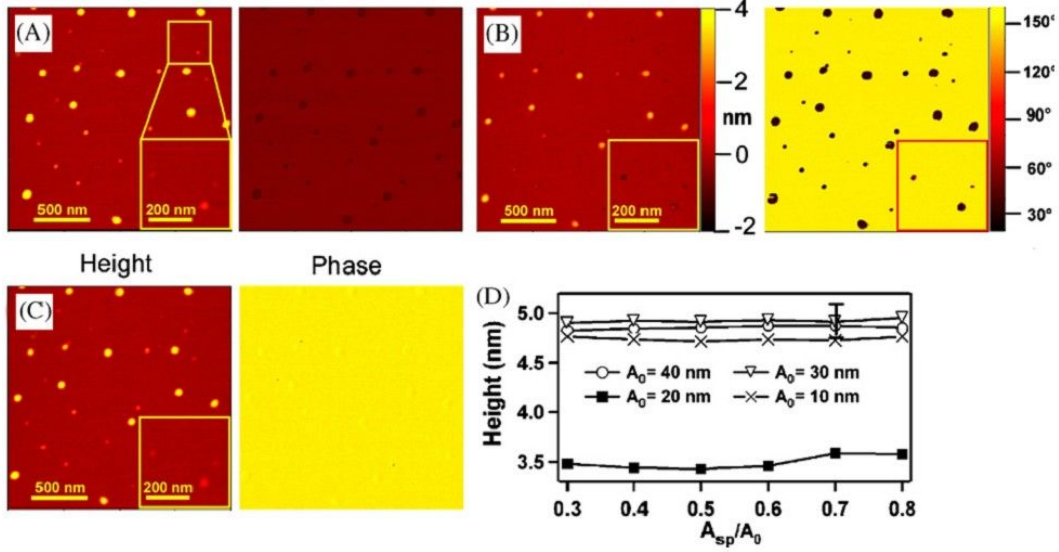


Figure 5.29: Chen et al. [152] identified the problem of NC/IC mode switching. A_o and A_{set} of the images are (A) 30 and 24 nm; (B) 20 and 6 nm; and (C) 10 and 3 nm, respectively. The insets are the zoom-in images of an area at the upper right part of the scan window as shown in (A). Averaged apparent height as a function of free amplitude and set point is plotted in (D), and the graph shows a $H_A - H_C$ value of 1.5 nm.

oscillation amplitude A_o , for tungsten oxide (WO_3) nanoparticles bound on graphite and mica substrates (Fig. 5.28). They also made a theoretical prediction on the dependence on the setpoint amplitude A_{set} . However, they did not include the possibility of NC-AFM, and attempted to explain all the anomalies with only the IC-AFM characteristics.

Very recently, Chen et al. [152] correctly described the effect of NC-AFM/IC-AFM mode switching on the nanoparticle size measurement. They observed height anomalies of gold nanoparticles on mica. They verified the relationship $H_C < H_A, H_D$, measuring a $H_A - H_C$ value of 1.5 nm (Fig. 5.29). However, they did not report any discrepancy between H_A and H_D , an important issue which has been discussed extensively in this chapter.

5.7 Conclusions and Outlook

While the dynamic AFM is a powerful tool for profiling surface-bound nanoparticles, an accurate metrology is difficult because the measured height depends on the operation parameters and the conditions. In this chapter, we have shown our experimental results on surface-bound gold nanoparticles, namely the dependence of their measured height on the initial (A_o) and setpoint (A_{set}) amplitudes on different substrates. Theoretical simulation of the amplitude–phase–distance (APD) curves showed that the largest dis-

crepancy can arise when the AFM mode on the particle is different from the mode on the substrate.

The novelty of our work is that we observed and explained the discrepancy between the all-NC-AFM height H_A and the all-IC-AFM height H_D . Experimental APD curves showed different NC-IC branch gaps on the particle and the substrate, which confirmed the $H_A - H_D$ differences. Different factors—namely the particle–substrate deformation and the capillary force—that can lead to the different NC–IC branch gaps were discussed, and included in subsequent simulations.

While the theoretical model used in this thesis captures many aspects of the dynamic AFM, it cannot, however, explain the full details of the experimental APD curves. Future research will be directed on understanding what factors lead to the IC–NC slope difference in the amplitude–distance curves, as well as finding the optimal conditions that allow accurate nanoparticle sizing.

6 Haptic Interface for the AFM and Nanomanipulation

An alternative to the conventional raster-scan operation of the AFM is the haptic interface. The AFM scanners are operated manually using a pointing device that can feed back the tip-sample force to the human hand. A model-independent haptic interface for AFMs was developed in the course of this thesis. The AFM can be applied for the manipulation of surface-bound nanostructures, but a quantitative understanding of the nanomanipulation process is difficult.

6.1 Haptic Interface

Haptic, from the Greek *haphe*, means “pertaining to the sense of touch”. With a haptic interface for the atomic force microscope (AFM), the operator *feels* the tip-sample interactions through tactile feedback. As the contact AFM (Section 2.5) and the intermittent-contact AFM (Section 2.8.2) use the repulsive contact forces between the tip and the sample, it is logical to investigate if a haptic interface can bring improvements to the user experience.

In addition to the tactile feedback, the haptic interface also requires a manual positioning system for displacing the cantilever or the sample. Hence a haptic positioning device similar to a force-feedback joystick for computer games is invariably involved (Fig. 6.1).

6.1.1 Reported Works

The first haptic interface for the AFM was realized in the University of North Carolina, U.S.A., as a natural continuation of a similar work on the scanning tunneling microscope (STM) (Fig. 6.2) [153, 154]. The user interface involved sophisticated display technologies for 3D visualization. A pen-like haptic device from SensAble Technologies was used for the AFM positioning and tactile feedback, and a Topometrix Observer was employed as the AFM system.

Ning Xi’s group in Michigan State University, U.S.A., reported an augmented-reality haptic interface, where the scanner position is corrected in real time for the effects of cantilever-bending-induced tip position change, and where the force calculation takes the tip-surface geometry into account [155]. To this date this is the most complete

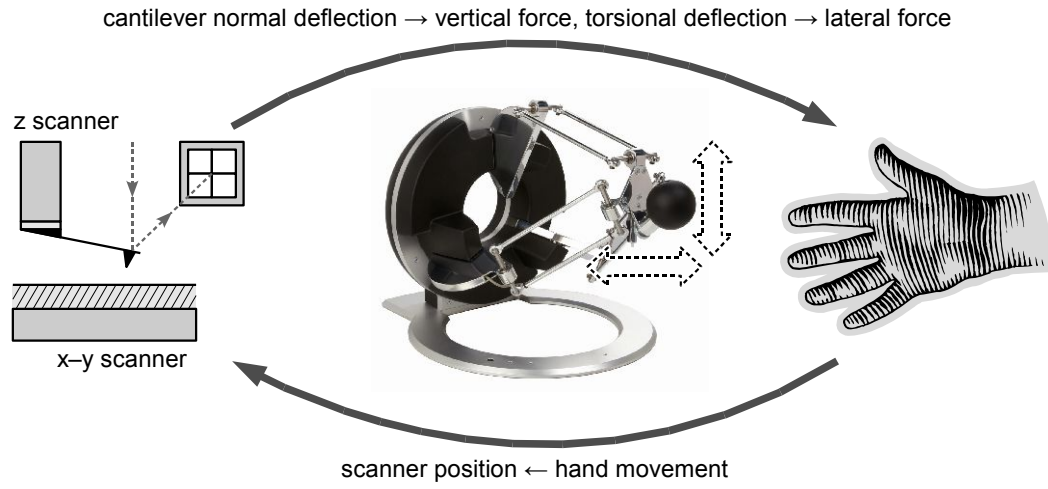


Figure 6.1: A general outline of the AFM haptic interface. The human hand manually controls the AFM x-y-z scanner position with the haptic device. The cantilever deflection signal is amplified to a tactile force by the haptic device. Shown in the figure is the Delta Haptic Device used in this thesis.

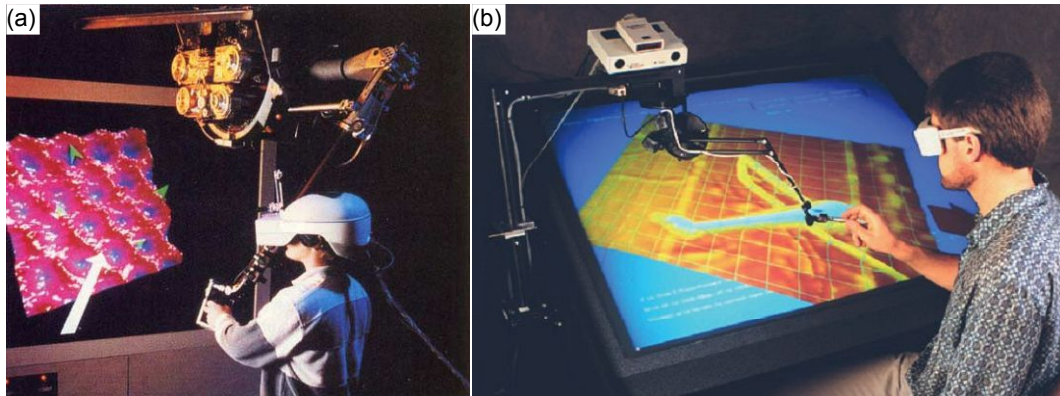


Figure 6.2: (a) The STM [153] and (b) the AFM [154] nanoManipulator systems from University of North Carolina

haptic interface reported in the literature. They also used the SensAble device for the haptic operation.

Our group, in collaboration with the Robotics lab (STI-IMT-LSRO2) at EPFL, developed a new haptic interface for the AFM [156, 157]. The Delta Haptic Device (DHD, Fig. 6.1), developed by Force Dimension, offers much better characteristics than the SensAble device. Also, a conventional computer display was used, making the system relatively cost-efficient. The haptic interface was implemented on a Pacific Nanotechnology Nano-R AFM.

A low-cost system using a force-feedback joystick for computer games has also been reported [158]. But in our experience, gaming joysticks usually cannot provide the high update rate (> 1 kHz) required for a smooth tactile experience.

6.1.2 Model-Independent Haptic Interface

As our Nano-R–DHD haptic interface system involved a heavy modification of the Nano-R control software [Fig. 6.3(a)], it was difficult to port the setup to a different AFM model, even when better systems became available. To realize a haptic interface for the Park Systems XE-100, a simpler approach using PC data acquisition cards was used [Fig. 6.3(b)].

The XE-100 signal access module and the controller electronics were modified to provide external scanner control. To be specific, the data-acquisition-card-generated voltage signals for the x–y position are *subtracted* from the XE-100 x–y detector signals, so that the controller’s x–y position feedback loop displaces the x–y scanner to compensate for the differences. For the z scanner control, the external voltage signal is added to the input stage of the z high voltage amplifier.

A new haptic interface software was written with Borland C++ Builder 6. The “AFM Haptic Interface” software reads the photodiode signals from the analog-to-digital converter card, calculates and writes the corresponding force to the haptic device, reads the haptic device handle position, and finally writes the x–y position signals to the digital-to-analog converter card. The software runs on a separate PC, and the update rates are typically 1–3 kHz sufficient for a smooth tactile feedback.

Admittedly, the new haptic interface is trickier to operate than the previous setup—an orchestration of the AFM control software and the haptic interface software is needed. However, the new setup is less dependent on the specific AFM model. As most commercial AFM systems provide x–y–z modulation functions through signal access modules, or at least the required controller circuit modification is much less difficult than the equivalent control software modification, the new haptic interface software can be reused on different AFM systems with little rework. In addition, the dynamic AFM operation can be readily implemented by feeding the lock-in amplifier outputs—instead of the cantilever dc and torsional deflection signals—to the data acquisition cards.

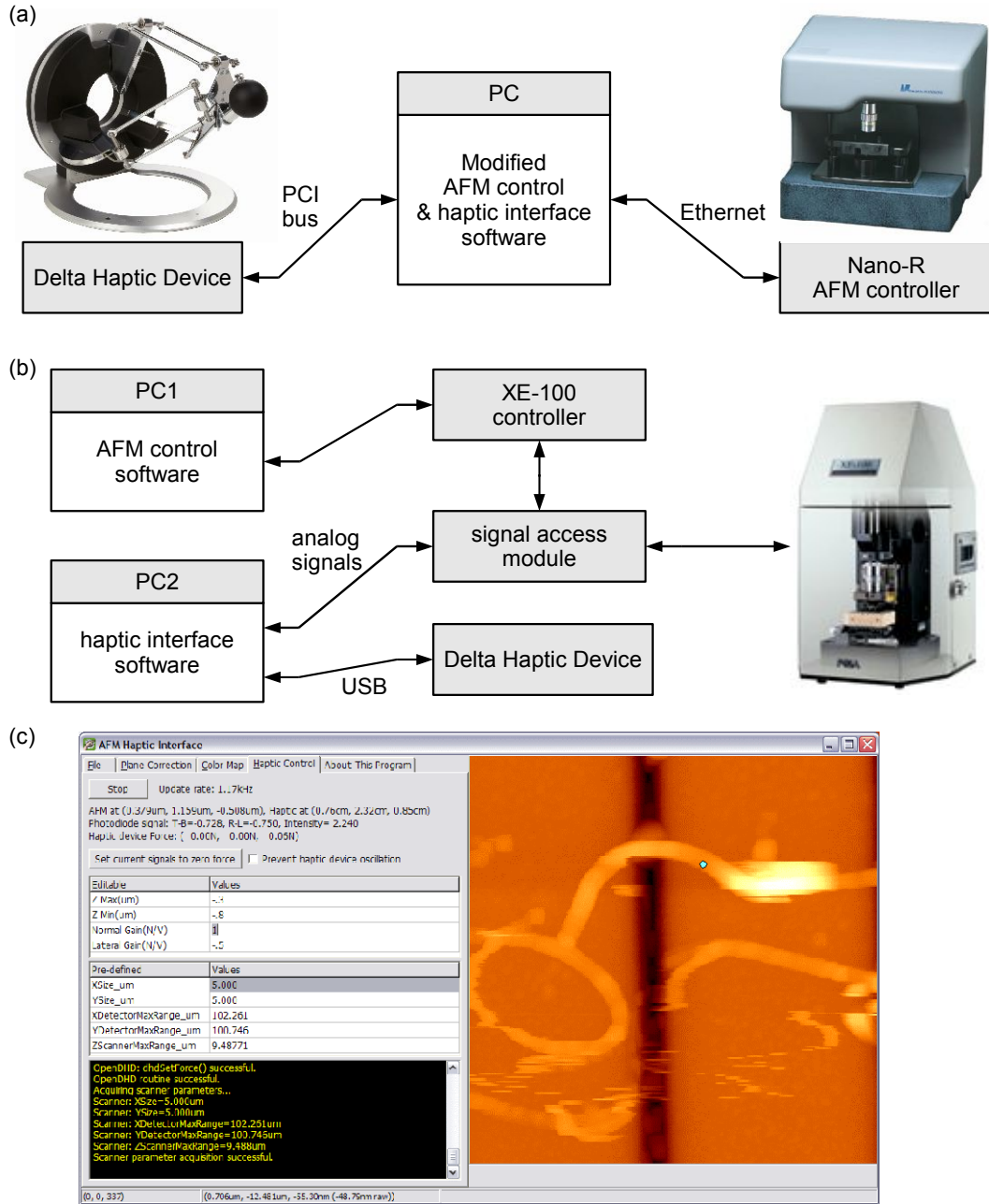


Figure 6.3: (a) The original Nano-R-DHD setup was realized through a heavy modification of the AFM control software. (b) The new XE-100-DHD setup was developed through an analog interface with the AFM, using (c) a separate haptic interface software.

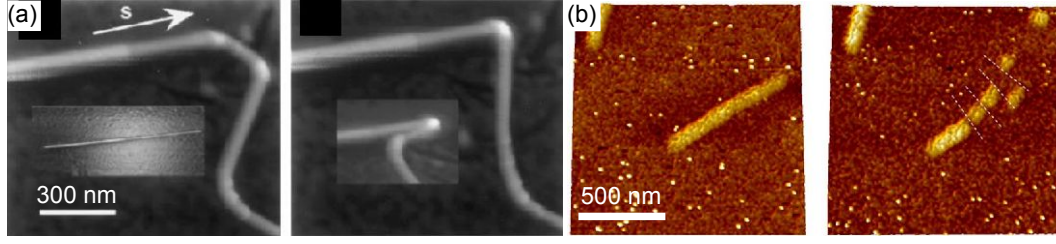


Figure 6.4: (a) The buckling of carbon nanotubes was demonstrated by Falvo et al. [159] (b) We could cut copper nanowires with our Nano-R-DHD setup [157].

6.2 Nanomanipulation

6.2.1 via Haptic Interface

An obvious application of the AFM haptic interface is the manipulation of surface-bound nanostructures. The North Carolina group demonstrated that they could bend, buckle [Fig. 6.4(a)] and roll carbon nanotubes, rupture fibrin fibers, and manipulate viruses [160, 161] with their nanoManipulator. Ning Xi's group demonstrated the manipulation of latex particles and silver nanorods. With our Nano-R-DHD setup, we have shown that we can bend and rotate carbon nanotubes, cut copper nanowires [Fig. 6.4(b)], and displace silica beads [157].

6.2.2 via Programmable Interface

But a haptic interface is not a prerequisite to nanomanipulation. Ritter et al. [162] demonstrated the nanomanipulation in intermittent-contact AFM (IC-AFM), with a programmable interface. They showed that the programmable interface can be just as if not more efficient than the haptic interface.

Furthermore, Ritter et al. [163] found that to move surface-bound latex particles or antimony islands by IC-AFM (operated by AM-AFM) at a fixed setpoint amplitude A_{set} , the driving force F_o (and thus the initial amplitude A_o) has to be raised above a critical value. In practice, we cannot determine the IC-AFM contact force directly from the AFM signals. As shown in Fig. 5.17(b), the cantilever deflection (and thus the photodiode signal) remains largely sinusoidal even when sharp contact forces are present. Hence Ritter took an alternative approach, arguing that the repulsive contact force that does useful work on the antimony islands should be proportional to the tip-sample power dissipation P_{ts} calculated from the equation [164]

$$P_{ts} = \frac{\pi k f}{Q} (A_o A \sin \phi - A^2 \frac{f}{f_R}), \quad (6.1)$$

where k is the cantilever spring constant, f and f_R are the operation and resonance frequencies, respectively, Q is the cantilever quality factor, A_o and A are the initial and

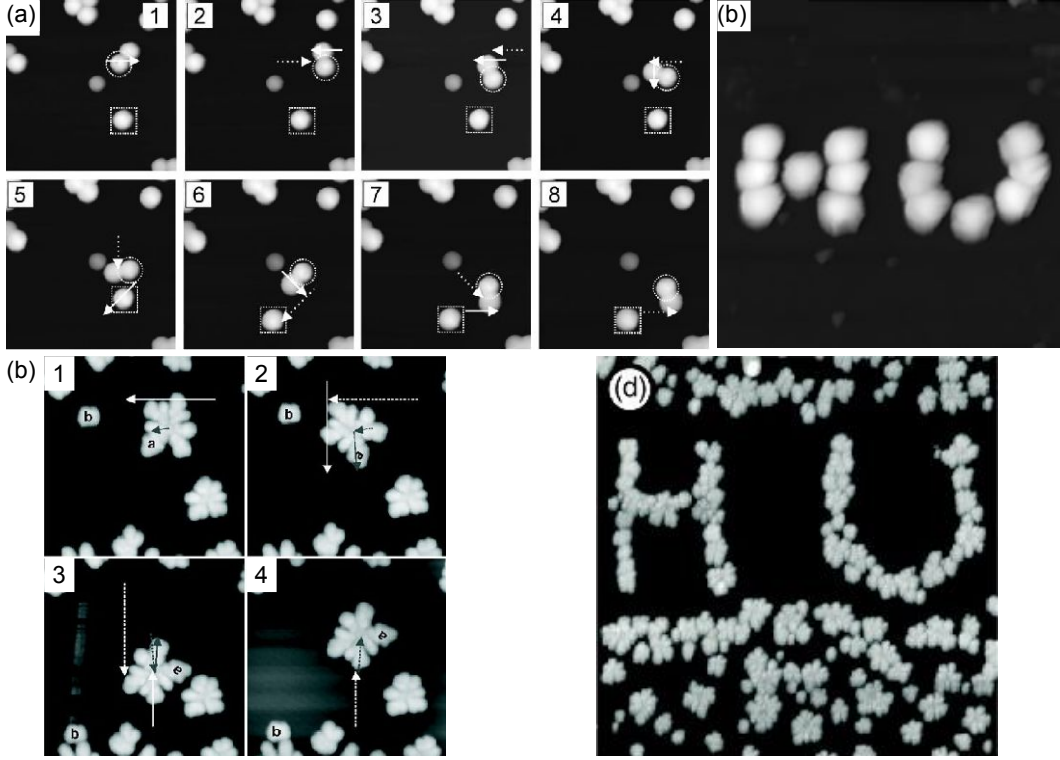


Figure 6.5: IC-AFM manipulation of (a)–(b) latex particles on highly oriented pyrolytic graphite (HOPG) [162], and (c)–(d) antimony (Sb) islands on HOPG [163].

actual amplitudes of cantilever oscillation, respectively, and ϕ is the phase difference between the cantilever oscillation and the driving signals. For $f = f_R$, the equation simplifies to

$$P_{ts} = \frac{\pi k f_R}{Q} (A_o A \sin \phi - A^2). \quad (6.2)$$

It was shown that P_{ts} was proportional to the contact area between the antimony islands and the HOPG substrate (calculated from AFM images), confirming Amonton's law that the friction is proportional to the real contact area.

We have followed Ritter's approach and verified that silicon-wafer-bound gold nanoparticles can be manipulated by the raster-scan operation of AM-AFM (Fig. 6.6). Phase images showed that the nanoparticle displacement was achieved by IC-AFM on the nanoparticle with appropriate parameters. With $f_R = 170.0$ kHz, $f = 170.1$ kHz, $Q = 600$, and $A_o = 5.0$ nm, non-manipulative imaging was possible with $A_{set} = 2.0$ nm and manipulation was possible with $A_{set} = 1.0$ nm. Switching between manipulation and imaging modes was possible by changing A_{set} during an image.

The asymmetry of the nanoparticle displacement is due to the asymmetry of our AFM's x–y raster scan motion [Fig. 6.7(b)]. Typically, the tip first moves from left to right relative to the sample, then repeats the path from right to left, and finally moves up an increment in the slow scan direction. In manipulation conditions, the right-to-left

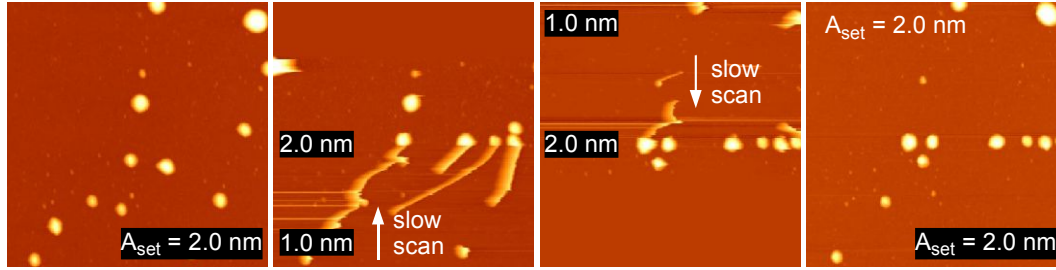


Figure 6.6: Gold nanoparticles bound on silicon could be manipulated with the raster-scan operation of AM-AFM, by varying the setpoint amplitude A_{set} during imaging. Noted in the images are the A_{set} values at different positions.

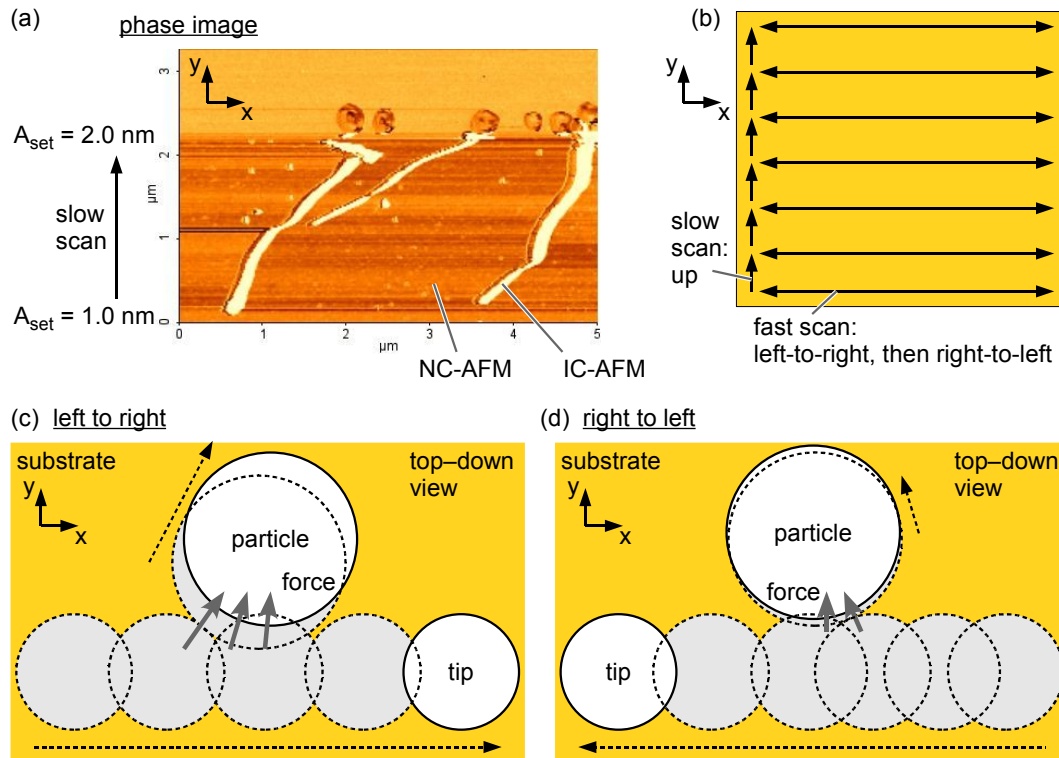


Figure 6.7: (a) The phase image shows that the tip-sample interaction switches to IC-AFM in the manipulation conditions. (b) The x-y scanner motion is asymmetric. The fast-scan line is repeated in two directions, before making an increment in the slow-scan direction. A top-down view of the tip-particle interaction on the sample x-y plane. (c) the left-to-right fast scan does more work on the nanoparticle than the (d) right-to-left fast scan due to the differences in relative positions. The scans do not completely displace the nanoparticle out of the nanoparticle path because of the AM-AFM feedback.

path [Fig. 6.7(c)] will do less work than the preceding left-to-right path [Fig 6.7(d)], because the particle displacement from the left-to-right scan changes the tip–particle contact surface. The tip does not move the particle completely out of its path because of the AM-AFM feedback that acts against manipulation.

The tip–particle contact model presented in Figs. 6.7(c) and (d) suggest that the dynamic AFM raster-scan manipulation can be used to study the friction between a particles and the substrate, since the friction should influence the displacement direction. In practice, the particles changed their directions during the manipulative imaging [Fig. 6.7(a)], possibly due to silica nanoparticles that collect at the particle–substrate interface, or a change in the tip–particle contact geometry due to particle rotation (the gold nanoparticles were not perfectly spherical). Furthermore, the manipulation conditions—such as the critical A_{set} needed to onset manipulation—varied with the AM-AFM feedback loop parameters, making quantitative analysis even more difficult. Furthermore, we could not reproduce the manipulation on gallium arsenide or steel substrates, and hence a comparative study was also not possible.

6.3 Conclusions and Outlook

An AFM-model-independent haptic interface software was developed in the course of this thesis. The use of analog signals makes the interface easier to implement on different AFM models.

Manipulation of silicon-wafer-bound gold nanoparticles was possible by raster scanning at varying AM-AFM setpoints. The results are promising, and the raster-scan approach may in future be used to study the friction of nanoparticles on different surfaces. A home-built AFM would serve as a better platform for the nanomanipulation studies. A close collaboration with an AFM manufacturer is also an option.

7 General Conclusions

It is exciting to see that mechanics and metrology, both disciplines of long history, can still show novel phenomena and disclose interesting secrets at the nanometer length scale.

7.1 Carbon Nanotubes

The Young's modulus of chemical-vapor-deposition (CVD)-grown carbon nanotubes, measured by deflecting suspended structures, showed a strong diameter dependence. The bending of defective nanotubes seemed to occur through the stick-slip motion at structural defects, which in turn implies that smaller catalysts produce nanotubes of better structure. The diameter dependence could be explained by the metastable-catalyst model, where the liquid skin of a partially molten catalyst plays a paramount role in determining the carbon diffusion kinetics and consequently the crystallinity of the produced nanotube.

Our work suggests that perfect multiwall carbon nanotubes can be grown in CVD by using catalysts that hold stable liquid skins at the growth conditions. Research is currently under way to study different catalyst materials that offer this possibility. Also, we believe that the carbon nanotube growth should in fact be divided into two separate stages: nucleation and growth. The conditions should be optimized for each stage. A solid catalyst may be required for the nucleation, while a good liquid skin would provide the ideal defect-free growth.

7.2 Nanoparticle Metrology

The size of catalyst nanoparticles is an important factor in determining the extent of partial melting, and our study showed that multiple values can be measured for the same particle, depending on the dynamic AFM imaging parameters. Through a numerical modeling of the tip-sample interactions in dynamic AFM and the acquisition of experimental amplitude-phase-distance (APD) curves, we could explain and reproduce the observed anomalies.

The results indicate that low-amplitude non-contact AFM at low-humidity conditions can give the most accurate size measurement. A systematic and standardized method for determining the optimum imaging parameters should be possible, by performing

APD curves on the substrate and the particles. The standardization of dynamic AFM would foster the adoption of non-contact AFM by different industries, enlarging the AFM market and the audience.

7.3 Nanomanipulation and Nanotribology

The intermittent-contact AFM instead offers the ability to manipulate surface-bound nanoparticles, and the raster-scan manipulation is a promising strategy for studying the nanoparticle–substrate friction on different surfaces. This strategy would allow a wider range of nanotribological systems to be studied.

7.4 Boil Deposition

We have reported a novel technique for the uniformly dispersed deposition of colloidal nanoparticles and nanowires on different surfaces. Boiling colloid drops on preheated surfaces, a process that can be performed without any sophisticated equipment or preparation, gave excellent results that outperform conventional techniques. The mechanism was explained in terms of microdrops, and a supporting evidence was provided through ink-jet experiments.

A high-speed-camera study of the microdrop dynamics on hot surfaces is currently being planned, as it should be able to determine the validity of our model. Boil deposition can be used with ink-jet printing to achieve lithography, and it is a promising and very cost-efficient method of pre-patterning catalyst nanoparticles for the CVD nanowire growth.

Finally, the author wishes that he has convinced the reader of the scientific and the practical significance of the presented work. A better understanding of the nanometer-scale mechanical and metrological phenomena is essential in the industrial application of nanotechnology.

A Scanner Positioning Errors and Solutions

Non-ideal characteristics of piezoelectric actuators are inevitable even with the flexure-guided scanners. Figure A.1 shows how flexure-guided scanners faithfully amplify the nonlinearity, hysteresis, and creep of the driving piezo element. The correct position values were obtained from detectors built into the scanners. These characteristics manifest themselves in two different aspects of AFM imaging: (1) inaccuracy of the relative tip-sample lateral position, and (2) inaccuracy of the height data.

Lateral Position Error

Nonlinear and hysteretic x-y scanner movement will heavily influence AFM images, as shown in Fig. A.2(a) and (b). In these images of a standard calibration grating, plateaus do not appear equally spaced or sized, and they do not appear square. The image appearance also depends heavily on the fast scan direction, which makes panning and zooming of the scan area difficult during AFM operation.

When position detectors are available, their signals can be used to address these problems. The x-y position detector signals can be fed back into the piezo driving circuitry in real-time to achieve linear motion. Figure A.2(c) shows another AFM image of the same standard sample, obtained with real-time x-y position correction. Length and angle measurements are now precise throughout the image. As the detectors typically suffer much less degradation over time compared to the piezoelectric elements, a single calibration is often sufficient for months or years of operation.

Height Measurement Error

Height measurement error is more difficult to handle. Figure A.3 shows the effect of piezoelectric creep on a typical AFM image. *Overshoot* phenomenon apparent in the z scanner voltage line profile [Fig. A.3(c)] is not present in the detector line profile [Fig. A.3(d)], and thus it is an artifact coming from the piezoelectric creep of the z scanner.

While the z scanner's problems of nonlinearity, hysteresis and creep are more pronounced for samples with tall ($> 0.5\ \mu\text{m}$) features, they can also become important for nanometer height measurements. Figure A.4 shows gold nanoparticles (40–80 nm) prepared on a Si wafer. The z voltage image Fig. A.4(a) suggests that these particles

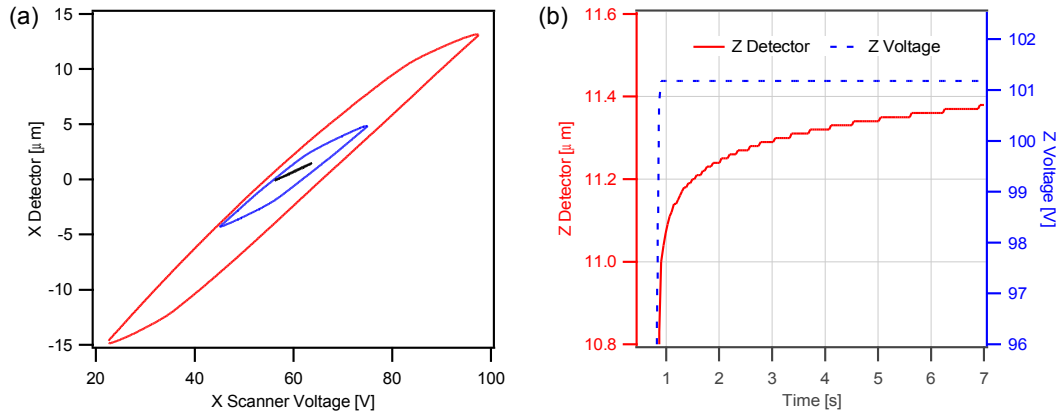


Figure A.1: (a) X scanner, driven over different ranges, show the characteristic hysteresis loops of a piezoelectric actuator. (b) Effects of creep require a few seconds to become negligible. This time scale is orders of magnitude longer than a typical pixel acquisition time of an AFM image.

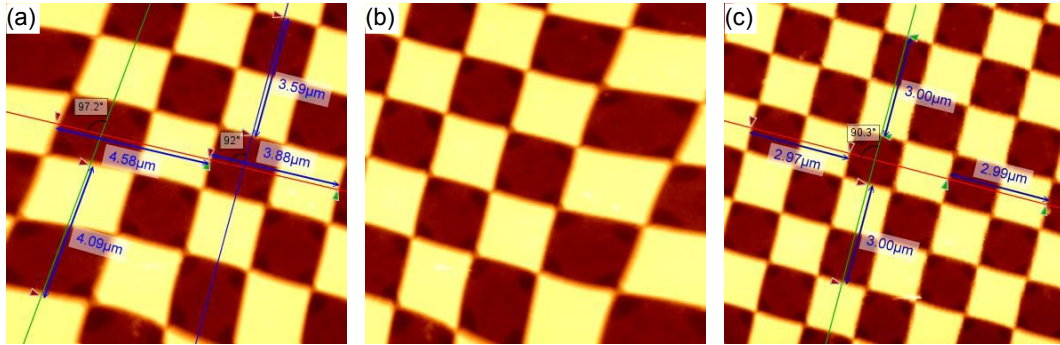


Figure A.2: $10\text{ }\mu\text{m} \times 10\text{ }\mu\text{m}$ AFM images of a MikroMasch TGX01 standard grating. (a) Nonlinear dynamics of the x-y scanner causes length and angle distortions. Fast-scan direction: left-to-right, slow-scan direction: bottom-to-top. (b) Image acquired simultaneously for the opposite fast-scan direction (right-to-left). (c) Image obtained with real-time x-y position correction. Length and angle measurements are now accurate and precise.

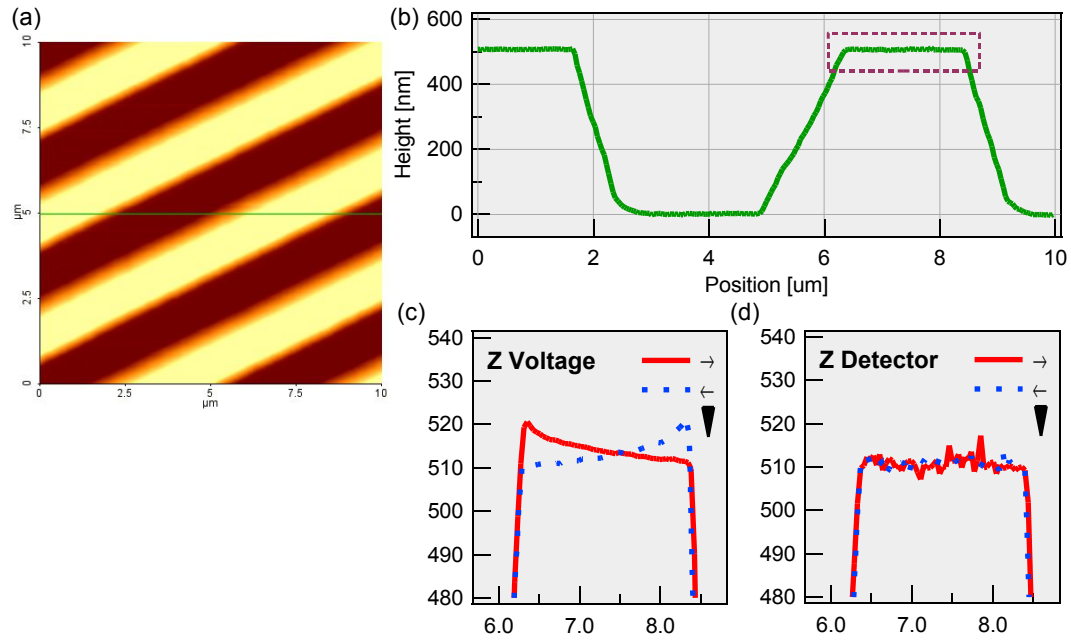


Figure A.3: (a) AFM image of MikroMasch TGZ03 standard grating. (b) Graph of the green line in (a). (c) Z scanner voltage data corresponding to the dotted rectangle display overshoot-like phenomena. (d) Z detector data of the same region line show no dependence on the scan direction.

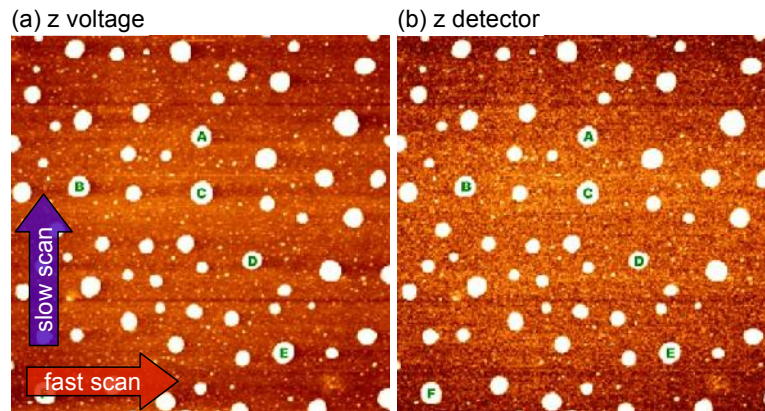


Figure A.4: (a) $5\text{ }\mu\text{m} \times 5\text{ }\mu\text{m}$ AFM topography (z scanner voltage) image of gold nanoparticles (40–80 nm) on Si wafer. Scan directions are noted on the image. Gold nanoparticles appear to have trenches (dark trails) to their right. (b) These trails are absent in the corresponding z detector image. Some of the particles have been labeled to aid comparison.

A Scanner Positioning Errors and Solutions

have trenches (dark trails) to their right, but such features are not present in the corresponding z detector image Fig. A.4(b). The trenches are therefore artifacts arising from the hysteresis and creep of the z scanner. The dimensions of dark trails vary with particle size as well as previous scan lines, because piezoelectric hysteresis is a history-dependent phenomenon.

Z detector signal is often useful in determining whether features in AFM images are real or not. However, the flat part of the graph in Fig. A.3(d) and the appearance of the silicon substrate in Fig. A.4(b) point out that the z detector signal is substantially noisier than that of the corresponding z voltage signal and cannot always serve as a replacement.

Bibliography

- [1] E. Ruska. The development of the electron microscope and of electron microscopy. *Reviews of Modern Physics*, 59:627–638, 1987. 2
- [2] G. Binnig, H. Rohrer, C. Gerber, and E. Weibel. Surface studies by scanning tunneling microscopy. *Physical Review Letters*, 49:57–61, 1982. 2
- [3] G. Binnig, C. F. Quate, and C. Gerber. Atomic force microscope. *Physical Review Letters*, 56:930–933, 1986. 2
- [4] C. Y. Chang and S. M. Sze, editors. *ULSI Technology*. McGraw–Hill, 1996. 2, 37, 41
- [5] H. W. Kroto, A. W. Allaf, and S. P. Balm. C₆₀: buckminsterfullerene. *Chemical Reviews*, 91:1213–1235, 1991. 2
- [6] S. Iijima. Helical microtubules of graphitic carbon. *Nature*, 354:56–58, 1991. 2, 23, 37
- [7] A. Bachtold, P. Hadley, T. Nakanishi, and C. Dekker. Logic circuits with carbon nanotube transistors. *Science*, 294:1317, 2001. 2
- [8] D. L. Klein, R. Roth, A. K. L. Lim, A. P. Alivisatos, and P. L. McEuen. A single-electron transistor made from a cadmium selenide nanocrystal. *Nature*, 389(6652):699, 1997. 2
- [9] J. M. Bennett and J. H. Dancy. Stylus profiling instrument for measuring statistical properties of smooth optical surfaces. *Applied Optics*, 20:1785–1802, 1981. 5
- [10] J. A. J. Steen, J. Hayakawa, T. Harada, Kyumin Lee, F. Calame, G. Boero, A. J. Kulik, and J. Brugger. Electrically conducting probes with full tungsten cantilever and tip for scanning probe applications. *Nanotechnology*, 17:1464–1469, 2006. 6
- [11] C. P. Green, H. Lioe, J. P. Cleveland, R. Proksch, P. Mulvaney, and J. E. Sader. Normal and torsional spring constants of atomic force microscope cantilevers. *Review of Scientific Instruments*, 75:1988, 2004. 7

Bibliography

- [12] J. L. Hutter and J. Bechhoefer. Calibration of atomic-force microscope tips. *Review of Scientific Instruments*, 64:1868, 1993. 7
- [13] P. J. Cumpson, J. Hedley, and P. Zhdan. Accurate force measurement in the atomic force microscope: a microfabricated array of reference springs for easy cantilever calibration. *Nanotechnology*, 14:918–924, 2003. 7
- [14] P. J. Cumpson, C. A. Clifford, and J. Hedley. Quantitative analytical atomic force microscopy: a cantilever reference device for easy and accurate afm spring-constant calibration. *Measurement Science and Technology*, 15:1337–1346, 2004. 7
- [15] P. J. Cumpson, J. Hedley, and C. A. Clifford. Microelectromechanical device for lateral force calibration in the atomic force microscope: lateral electrical nanobalance. *Journal of Vacuum Science & Technology B: Microelectronics and Nanometer Structures*, 23:1992, 2005. 7, 46
- [16] J. E. Sader. Susceptibility of atomic force microscope cantilevers to lateral forces. *Review of Scientific Instruments*, 74:2438, 2003. 7, 46
- [17] J. E. Sader and R. C. Sader. Susceptibility of atomic force microscope cantilevers to lateral forces: experimental verification. *Applied Physics Letters*, 83:3195, 2003. 7
- [18] J. Kwon, J. Hong, Y.-S. Kim, D.Y. Lee, K. Lee, S.-M. Lee, and S.-I. Park. Atomic force microscope with improved scan accuracy, scan speed, and optical vision. *Review of Scientific Instruments*, 74:4378, 2003. 9, 20
- [19] S. Hong and C. A. Mirkin. A nanoplotter with both parallel and serial writing capabilities. *Science*, 288:1808–1811, 2000. 10
- [20] H. J. Butt, B. Cappella, and M. Kappl. Force measurements with the atomic force microscope: technique, interpretation and applications. *Surface Science Reports*, 59:1–152, 2005. 11, 13
- [21] E. Meyer, R. Overney, D. Brodbeck, L. Howald, R. Lüthi, J. Frommer, and H. J. Güntherodt. Friction and wear of Langmuir-Blodgett films observed by friction force microscopy. *Physical Review Letters*, 69(12):1777–1780, 1992. 11
- [22] B. Cappella and G. Dietler. Force-distance curves by atomic force microscopy. *Surface Science Reports*, 34:5–104, 1999. 11, 19
- [23] P. Pittet, Kyumin Lee, A. J. Kulik, J.-J. Meister, and Hinz B. Fibrogenic fibroblasts increase intercellular adhesion strength by reinforcing individual ob-cadherin bonds. *Journal of Cell Science*, 121:877–886, 2008. 12, 13

- [24] Y. Martin, C. C. Williams, and H. K. Wickramasinghe. Atomic force microscope—force mapping and profiling on a sub 100-Å scale. *Journal of Applied Physics*, 61:4723, 1987. 16
- [25] T. R. Albrecht, P. Grütter, D. Horne, and D. Rugar. Frequency modulation detection using high-Q cantilevers for enhanced force microscope sensitivity. *Journal of Applied Physics*, 69:668, 1991. 17
- [26] Q. Zhong, D. Inniss, K. Kjoller, and V. B. Elings. Fractured polymer/silica fiber surface studied by tapping mode atomic force microscopy. *Surface Science*, 290:L688–L692, 1993. 18
- [27] C. A. J. Putman, K. O. Van der Werf, B. G. De Grooth, N. F. Van Hulst, and J. Greve. Tapping mode atomic force microscopy in liquid. *Applied Physics Letters*, 64:2454, 1994. 18
- [28] N. A. Burnham, O. P. Behrend, F. Oulevey, G. Gremaud, P. J. Gallo, D. Gourdon, E. Dupas, A. J. Kulik, H. M. Pollock, and G. A. D. Briggs. How does a tip tap. *Nanotechnology*, 8(2):67–75, 1997. 18
- [29] G. Bar, Y. Thomann, R. Brandsch, H. J. Cantow, and M.-H. Whangbo. Factors affecting the height and phase images in tapping mode atomic force microscopy. study of phase-separated polymer blends of poly (ethene-co-styrene) and poly (2, 6-dimethyl-1, 4-phenylene oxide). *Langmuir*, 13:3807–3812, 1997. 18
- [30] P. Gleyzes, P. K. Kuo, and A. C. Boccaro. Bistable behavior of a vibrating tip near a solid surface. *Applied Physics Letters*, 58:2989, 1991. 18
- [31] J. P. Cleveland, B. Anczykowski, A. E. Schmid, and V. B. Elings. Energy dissipation in tapping-mode atomic force microscopy. *Applied Physics Letters*, 72:2613–2615, 1998. 18
- [32] R. García and A. San Paulo. Attractive and repulsive tip-sample interaction regimes in tapping-mode atomic force microscopy. *Physical Review B*, 60:4961–4967, 1999. 18
- [33] Kyumin Lee, M. Duchamp, G. Kulik, A. Magrez, J. W. Seo, S. Jeney, A. J. Kulik, L. Forro, R. S. Sundaram, and J. Brugger. Uniformly dispersed deposition of colloidal nanoparticles and nanowires by boiling. *Applied Physics Letters*, 91:173112, 2007. 21, 29
- [34] G. Schmid. Metal nanoparticles, synthesis of. In *Encyclopedia of inorganic chemistry*. John Wiley & Sons, Ltd., 2006. 21, 22

Bibliography

- [35] T. de los Arcos, M. G. Garnier, J. W. Seo, P. Oelhafen, V. Thommen, and D. Mathys. The influence of catalyst chemical state and morphology on carbon nanotube growth. *Journal of Physical Chemistry B*, 108:7728–7734, 2004. 21
- [36] K. Okuyama and L. I. Wuled. Preparation of nanoparticles via spray route. *Chemical Engineering Science*, 58:537–547, 2003. 21
- [37] J. H. Kim, T. A. Germer, G. W. Mulholland, and S. H. Ehrman. Size-monodisperse metal nanoparticles via hydrogen-free spray pyrolysis. *Journal of Applied Physics*, 36:L714, 1997. 21
- [38] H. Kim, J. Kim, H. Yang, J. Suh, T. Kim, B. Han, S. Kim, D. S. Kim, P. V. Pikhitsa, and M. Choi. Parallel patterning of nanoparticles via electrodynamic focusing of charged aerosols. *Nature*, 1:117–121, 2006. 22
- [39] Y. Sun and Y. Xia. Shape-controlled synthesis of gold and silver nanoparticles. *Science*, 298:2176–2179, 2002. 22
- [40] Y. Yin, R. M. Rioux, C. K. Erdonmez, S. Hughes, G. A. Somorjai, and A. P. Alivisatos. Formation of hollow nanocrystals through the nanoscale Kirkendall effect. *Science*, 304:711–714, 2004. 22
- [41] J. Turkevich, P. C. Stevenson, and J. Hillier. A study of the nucleation and growth processes in the synthesis of colloidal gold. *Discussions of the Faraday Society*, 11:55–75, 1951. 22
- [42] M. C. Daniel and D. Astruc. Gold nanoparticles: assembly, supramolecular chemistry, quantum-size-related properties, and applications toward biology, catalysis, and nanotechnology. *Chemical Reviews*, 104:293–346, 2004. 22
- [43] T. Yonezawa and T. Kunitake. Practical preparation of anionic mercapto ligand-stabilized gold nanoparticles and their immobilization. *Colloids and Surfaces A: Physicochemical and Engineering Aspects*, 149:193–199, 1999. 22
- [44] A. Thess, R. Lee, P. Nikolaev, H. Dai, P. Petit, J. Robert, C. Xu, Y. H. Lee, S. G. Kim, A.G. Rinzler, D. T. Colbert, G. E. Scuseria, D. Tomanek, J. E. Fischer, and R. E. Smalley. Crystalline ropes of metallic carbon nanotubes. *Science*, 273:483, 1996. 23
- [45] Y. Feldman, E. Wasserman, D. J. Srolovitz, and R. Tenne. High-rate, gas-phase growth of MoS₂ nested inorganic fullerenes and nanotubes. *Science*, 267:222–225, 1995. 23
- [46] R. Tenne, L. Margulis, M. Genut, and G. Hodes. Polyhedral and cylindrical structures of WS₂. *Nature*, 360:444–445, 1992. 23

- [47] M. Law, J. Goldberger, and P. Yang. Semiconductor nanowires and nanotubes. *Annual Review of Materials Research*, 34:83–122, 2004. 23, 25
- [48] L. Forró and C. Schönenberger. Physical properties of multi-wall nanotubes. In M. S. Dresselhaus, G. Dresselhaus, and Ph. Avouris, editors, *Carbon nanotubes: synthesis, structure, properties, and applications*, pages 29–54. Springer, 2001. 24, 67
- [49] E. Couteau, K. Hernadi, J. W. Seo, L. Thiên-Nga, Cs. Mikó, R. Gaál, and L. Forró. CVD synthesis of high-purity multiwalled carbon nanotubes using CaCO_3 catalyst support for large-scale production. *Chemical Physics Letters*, 378:9–17, 2003. 24
- [50] Y.-L. Li, I. A. Kinloch, and A. H. Windle. Direct spinning of carbon nanotube fibers from chemical vapor deposition synthesis. *Science*, 304:276–278, 2004. 24
- [51] A. Magrez, J. W. Seo, V. Kuznetsov, and L. Forró. Evidence of an equimolar $\text{C}_2\text{H}_2\text{-CO}_2$ reaction in the synthesis of carbon nanotubes. *Angewante Chemie International Edition*, 46:441–444, 2007. 24
- [52] H. Dai. Nanotube growth and characterization. In M. S. Dresselhaus, G. Dresselhaus, and Ph. Avouris, editors, *Carbon nanotubes: synthesis, structure, properties, and applications*, pages 29–54. Springer, 2001. 24, 53
- [53] A.-C. Dupuis. The catalyst in the CCVD of carbon nanotubes—a review. *Progress in Materials Science*, 50:929–961, 2005. 25, 60, 62
- [54] M. H. Huang, Y. Wu, H. Feick, N. Tran, E. Weber, and P. Yang. Catalytic growth of zinc oxide nanowires by vapor transport. *Advanced Materials*, 13:113–116, 2001. 25, 29
- [55] M. Niederberger, H. J. Muhr, F. Krumeich, F. Bieri, D. Gunther, and R. Nesper. Low-cost synthesis of vanadium oxide nanotubes via two novel non-alkoxide routes. *Chemistry of Materials*, 12:1995–2000, 2000. 25, 29
- [56] L. Vayssieres. Growth of arrayed nanorods and nanowires of ZnO from aqueous solutions. *Advanced Materials*, 15:464–466, 2003. 26
- [57] A. Sugunan, H. C. Warad, M. Boman, and J. Dutta. Zinc oxide nanowires in chemical bath on seeded substrates: Role of hexamine. *Journal of Sol-Gel Science and Technology*, 39:49–56, 2006. 26
- [58] B. D. Yuhas, D. O. Zitoun, P. J. Pauzauskie, R. He, and P. Yang. Transition-metal doped zinc oxide nanowires. *Angewante Chemie International Edition*, 45:420–423, 2006. 26

- [59] R. D. Deegan, O. Bakajin, T. F. Dupont, G. Huber, S. R. Nagel, and T. A. Witten. Capillary flow as the cause of ring stains from dried liquid drops. *Nature*, 389:827–829, 1997. 26
- [60] N. D. Denkov, O. D. Velev, P. A. Kralchevsky, I. B. Ivanov, H. Yoshimura, and K. Nagayama. Mechanism of formation of two-dimensional crystals from latex particles on substrates. *Langmuir*, 8:3183–3190, 1992. 26
- [61] A. N. Shipway, E. Katz, and I. Willner. Nanoparticle arrays on surfaces for electronic, optical, and sensor applications. *ChemPhysChem*, 1:18–52, 2000. 27, 35
- [62] T. Sato, D. G. Hasko, and H. Ahmed. Nanoscale colloidal particles: monolayer organization and patterning. *Journal of Vacuum Science and Technology B*, 15:45–48, 1997. 27
- [63] Y.-K. Hong, H. Kim, G. Lee, W. Kim, J.-I. Park, J. Cheon, and J.-Y. Koo. Controlled two-dimensional distribution of nanoparticles by spin-coating method. *Applied Physics Letters*, 80:844, 2002. 27
- [64] K.-S. Chou, K.-C. Huang, and H.-H. Lee. Fabrication and sintering effect on the morphologies and conductivity of nano-ag particle films by the spin coating method. *Nanotechnology*, 16:779–784, 2005. 27
- [65] Y. Huh, J. Y. Lee, J. Cheon, Y. K. Hong, J. Y. Koo, T. J. Lee, and C. J. Lee. Controlled growth of carbon nanotubes over cobalt nanoparticles by thermal chemical vapor deposition. *Journal of Materials Chemistry*, 13:2297–2300, 2003. 27
- [66] J. P. Spatz, A. Roescher, and M. Möller. Gold nanoparticles in micellar poly(styrene)-b-poly(ethylene oxide) films—size and interparticle distance control in monoparticulate films. *Advanced Materials*, 8:337–340, 1996. 28
- [67] J. P. Spatz, V. Z.-H. Chan, S. Mössmer, F.-M. Kamm, A. Plettl, P. Ziemann, and M. Möller. A combined top-down/bottom-up approach to the microscopic localization of metallic nanodots. *Advanced Materials*, 14:1827–1832, 2002. 28
- [68] Y. Cui, M. T. Björk, J. A. Liddle, C. Sönnichsen, B. Boussert, and A. P. Alivisatos. Integration of colloidal nanocrystals into lithographically patterned devices. *Nano Letters*, 4:1093–1098, 2004. 28
- [69] J.-P. Salvetat, J.-M. Bonard, N. H. Thomson, A. J. Kulik, L. Forró, W. Benoit, and L. Zuppiroli. Mechanical properties of carbon nanotubes. *Applied Physics A: Materials Science & Processing*, 69:255–260, 1999. 28

- [70] K. Yamamoto, S. Akita, and Y. Nakayama. Orientation and purification of carbon nanotubes using ac electrophoresis. *Journal of Physics D*, 31:L34–L36, 1998. 29
- [71] A. Magrez, E. Vasco, J. W. Seo, C. Dieker, N. Setter, and L. Forró. Growth of single-crystalline KNbO_3 nanostructures. *Journal of Physical Chemistry B*, 110:58–61, 2006. 29
- [72] J.-M. Bonard, T. Stora, J.-P. Salvetat, F. Maier, T. Stöckli, C. Duschl, L. Forró, W. A. de Heer, and A. Châtelain. Purification and size-selection of carbon nanotubes. *Advanced Materials*, 9:827–831, 1997. 29
- [73] P. Tartarini, G. Lorenzini, and M. R Randi. Experimental study of water droplet boiling on hot, non-porous surfaces. *Heat and Mass Transfer*, 34:437–447, 1999. 34, 35
- [74] H.-Y. Kim, S.-Y. Park, and K. Min. Imaging the high-speed impact of microdrop on solid surface. *Review of Scientific Instruments*, 74:4930–4937, 2003. 34, 36
- [75] A. L. Biance, C. Clanet, and D. Quéré. Leidenfrost drops. *Physics of Fluids*, 15:1632–1637, 2003. 34
- [76] J. Park and J. Moon. Control of colloidal particle deposit patterns within picoliter droplets ejected by ink-jet printing. *Langmuir*, 22:3506–3513, 2006. 34
- [77] R. D. Deegan. Pattern formation in drying drops. *Physical Review E*, 61:475–485, 2000. 35
- [78] Kyumin Lee, B. Lukić, A. Magrez, J. W. Seo, G. A. D. Briggs, A. J. Kulik, and L. Forró. Diameter-dependent elastic modulus supports the metastable-catalyst growth of carbon nanotubes. *Nano Letters*, 7:1598–1602, 2007. 37, 49
- [79] J. W. G. Wildöer, L. C. Venema, A. G. Rinzler, R. E. Smalley, and C. Dekker. Electronic structure of atomically resolved carbon nanotubes. *Nature*, 391:59–62, 1998. 37
- [80] R. H. Baughman, A. A. Zakhidov, and W. A. de Heer. Carbon nanotubes—the route toward applications. *Science*, 297:787–792, 2002. 37, 40
- [81] S. E. Thompson and S. Parthasarathy. Moore’s law: the future of Si microelectronics. *Materials Today*, 9:20–25, 2006. 39, 40
- [82] M. Bohr, K. Mistry, and S. Smith. Presentation: Intel demonstrates high-k + metal gate transistor breakthrough on 45 nm microprocessors. http://download.intel.com/pressroom/kits/45nm/Press45nm107_FINAL.pdf, 2007. 39
- [83] K. N. Tu. Recent advances on electromigration in very-large-scale-integration of interconnects. *Journal of Applied Physics*, 94:5451, 2003. 39

- [84] Y. Awano, S. Sato, D. Kondo, M. Ohfuti, A. Kawabata, M. Nihei, and N. Yokoyama. Carbon nanotube via interconnect technologies: size-classified catalyst nanoparticles and low-resistance ohmic contact formation. *physica status solidi (a)*, 203:3611–3616, 2006. 39, 40
- [85] M. Nihei, T. Hyakushima, S. Sato, T. Nozue, M. Norimatsu, M. Mishima, T. Murakami, D. Kondo, A. Kawabata, M. Ohfuti, and Y. Awano. Electrical properties of carbon nanotube via interconnects fabricated by novel damascene process. In *IEEE 2007 International Interconnect Technology Conference*, 2007. 39, 40
- [86] M. Nihei, M. Horibe, A. Kawabata, Y. Awano, F. Ltd, and J. Atsugi. Carbon nanotube vias for future LSI interconnects. In *Proceedings of the IEEE 2004 International Interconnect Technology Conference*, 2004. 39
- [87] M. Horibe, M. Nihei, D. Kondo, A. Kawabata, and Y. Awano. Mechanical polishing technique for carbon nanotube interconnects in ULSIs. *Japanese Journal of Applied Physics*, 43:6499–6502, 2004. 39, 41
- [88] H.-S. P. Wong. Beyond the conventional transistor. *IBM Journal of Research and Development*, 46:133–168, 2002. 40
- [89] F. Chen, B. Wang, Y. Chen, and L. J. Li. Toward the extraction of single species of single-walled carbon nanotubes using fluorene-based polymers. *Nano Letters*, 7:3013–3017, 2007. 40
- [90] X. H. Liu, Z. Suo, Q. Ma, and H. Fujimoto. Developing design rules to avert cracking and debonding in integrated circuit structures. *Engineering Fracture Mechanics*, 66:387–402, 2000. 40
- [91] J. M. Gere and S. P. Timoshenko. *Mechanics of Materials*. Brooks/Cole Publishing Company, 5th edition, 2001. 42, 47
- [92] B. G. Demczyk, Y. M. Wang, J. Cumings, M. Hetman, W. Han, A. Zettl, and R. O. Ritchie. Direct mechanical measurement of the tensile strength and elastic modulus of multiwalled carbon nanotubes. *Materials Science & Engineering A*, 334:173–178, 2002. 42
- [93] M. F. Yu, O. Lourie, M. J. Dyer, K. Moloni, T. F. Kelly, and R. S. Ruoff. Strength and breaking mechanism of multiwalled carbon nanotubes under tensile load. *Science*, 287:637–640, 2000. 42
- [94] M. M. J. Treacy, T. W. Ebbesen, and J. M. Gibson. Exceptionally high Young’s modulus observed for individual carbon nanotubes. *Nature*, 381:678–680, 1996. 42, 43, 51

- [95] P. Poncharal, Z. L. Wang, D. Ugarte, and W. A. de Heer. Electrostatic deflections and electromechanical resonances of carbon nanotubes. *Science*, 283:1513–6, 1999. 43, 44, 51, 58
- [96] S. T. Purcell, P. Vincent, C. Journet, and V. T. Binh. Tuning of nanotube mechanical resonances by electric field pulling. *Physical Review Letters*, 89:276103, 2002. 43, 45
- [97] E. W. Wong, P. E. Sheehan, and C. M. Lieber. Nanobeam mechanics—elasticity, strength, and toughness of nanorods and nanotubes. *Science*, 277:1971–1975, 1997. 45, 51
- [98] J. P. Salvetat, A. J. Kulik, J. M. Bonard, G. A. D. Briggs, T. Stockli, K. Metenier, S. Bonnamy, F. Beguin, N. A. Burnham, and L. Forro. Elastic modulus of ordered and disordered multiwalled carbon nanotubes. *Advanced Materials*, 11:161–165, 1999. 46, 51, 53, 55, 56, 57, 58
- [99] G. T. Kim, G. Gu, U. Waizmann, and S. Roth. Simple method to prepare individual suspended nanofibers. *Applied Physics Letters*, 80:1815, 2002. 48
- [100] R. J. Cannara, M. J. Brukman, and R. W. Carpick. Cantilever tilt compensation for variable-load atomic force microscopy. *Review of Scientific Instruments*, 76:053706, 2005. 50
- [101] A. Krishnan, E. Dujardin, T. W. Ebbesen, P. N. Yianilos, and M. M. J. Treacy. Young’s modulus of single-walled nanotubes. *Physical Review B*, 58:14013–14019, 1998. 51
- [102] J. P. Lu. Elastic properties of carbon nanotubes and nanoropes. *Physical Review Letters*, 79:1297–1300, 1997. 51
- [103] J.-P. Salvetat, G. A. D. Briggs, J.-M. Bonard, R. R. Bacsá, A. J. Kulik, T. Stöckli, N. A. Burnham, and L. Forró. Elastic and shear moduli of single-walled carbon nanotube ropes. *Physical Review Letters*, 82:944–947, 1999. 51, 52, 53, 55, 56, 57, 59
- [104] B. Lukic, J. W. Seo, R. R. Bacsá, S. Delpeux, F. Beguin, G. Bister, A. Fonseca, J. B. Nagy, A. Kis, S. Jeney, A. J. Kulik, and L. Forro. Catalytically grown carbon nanotubes of small diameter have a high young’s modulus. *Nano Letters*, 5:2074–2077, 2005. 51, 53, 54, 55, 56
- [105] J. D. Renton. *Elastic Beams and Frames*. Horwood Publishing, 2002. 52
- [106] A. Kis, G. Csanyi, J.-P. Salvetat, T. N. Lee, E. Couteau, A. J. Kulik, W. Benoit, J. Brugger, and L. Forro. Reinforcement of single-walled carbon nanotube bundles by intertube bridging. *Nature Materials*, 3:153–157, 2004. 53

- [107] J. Gaillard, M. Skove, and A. M. Rao. Mechanical properties of chemical vapor deposition-grown multiwalled carbon nanotubes. *Applied Physics Letters*, 86:233109, 2005. 53
- [108] B. Lukic, J. W. Seo, E. Couteau, Kyumin Lee, S. Gradecak, R. Berkecz, K. Hernadi, S. Delpeux, T. Cacciaguerra, F. Béguin, A. Fonseca, J. B. Nagy, G Csanyi, A. Kis, A. J. Kulik, and L. Forro. Elastic modulus of multi-walled carbon nanotubes produced by catalytic chemical vapour deposition. *Applied Physics A*, 80:695–700, 2005. 53, 54
- [109] M. Endo, Y. A. Kim, T. Hayashi, T. Yanagisawa, H. Muramatsu, M. Ezaka, H. Terrones, M. Terrones, and M. S. Dresselhaus. Microstructural changes induced in “stacked cup” carbon nanofibers by heat treatment. *Carbon*, 41:1941–1947, 2003. 54, 55
- [110] K. Hernadi, A. Fonseca, J. B. Nagy, D. Bernaerts, A. Fudala, and A. A. Lucas. Catalytic synthesis of carbon nanotubes using zeolite support. *Zeolites*, 17:416–423, 1996. 54
- [111] I. Palaci, S. Fedrigo, H. Brune, C. Klinke, M. Chen, and E. Riedo. Radial elasticity of multiwalled carbon nanotubes. *Physical Review Letters*, 94:175502, 2005. 58
- [112] T. Chang and H. Gao. Size-dependent elastic properties of a single-walled carbon nanotube via a molecular mechanics model. *Journal of the Mechanics and Physics of Solids*, 51:1059–1074, 2003. 58
- [113] L. Wang, Q. Zheng, J. Z. Liu, and Q. Jiang. Size dependence of the thin-shell model for carbon nanotubes. *Physical Review Letters*, 95:105501, 2005. 58
- [114] M. Arroyo and T. Belytschko. Nonlinear mechanical response and rippling of thick multiwalled carbon nanotubes. *Physical Review Letters*, 91:215505, 2003. 58
- [115] S. Akita, S. Sawaya, and Y. Nakayama. Energy loss of carbon nanotube cantilevers for mechanical vibration. *Japanese Journal of Applied Physics*, 46:6295–6298, 2007. 58
- [116] R. M. Overney, H. Takano, M. Fujihira, W. Paulus, and H. Ringsdorf. Anisotropy in friction and molecular stick–slip motion. *Physical Review Letters*, 72:3546–3549, 1994. 60
- [117] R. S. Wagner and W. C. Ellis. Vapor–liquid mechanism of single crystal growth. *Applied Physics Letters*, 4:89–90, 1964. 60, 61
- [118] R. T. K. Baker. Catalytic growth of carbon filaments. *Carbon*, 27:315–323, 1989. 60

- [119] J. R. Rostrup-Nielsen and D. L. Trimm. Mechanisms of carbon formation on nickel-containing catalysts. *Journal of Catalysis*, 48:155–165, 1977. 60
- [120] H. Kanzow, A. Schmalz, and A. Ding. Laser-assisted production of multi-walled carbon nanotubes from acetylene. *Chemical Physics Letters*, 295:525–530, 1998. 60, 62
- [121] Y. Homma, Y. Kobayashi, T. Ogino, D. Takagi, R. Ito, Y. J. Jung, and P. M. Ajayan. Role of transition metal catalysts in single-walled carbon nanotube growth in chemical vapor deposition. *Journal of Physical Chemistry B*, 107:12161–12164, 2003. 61, 62, 65
- [122] S. L. Lai, J. Y. Guo, V. Petrova, G. Ramanath, and L. H. Allen. Size-dependent melting properties of small tin particles: nanocalorimetric measurements. *Physical Review Letters*, 77:99–102, 1996. 61, 62
- [123] P. Letellier, A. Mayaffre, and M. Turmine. Melting point depression of nanosolids: nonextensive thermodynamics approach. *Physical Review B*, 76:45428, 2007. 62
- [124] P. Buffat and J.-P. Borel. Size effect on the melting temperature of gold particles. *Physical Review A*, 13:2287–2298, 1976. 62
- [125] F. Ding, K. Bolton, and A. Rosén. Iron-carbide cluster thermal dynamics for catalyzed carbon nanotube growth. *Journal of Vacuum Science & Technology A: Vacuum, Surfaces, and Films*, 22:1471, 2004. 62
- [126] A. R. Harutyunyan, T. Tokune, and E. Mora. Liquid as a required catalyst phase for carbon single-walled nanotube growth. *Applied Physics Letters*, 87:051919, 2005. 62
- [127] E. F. Kukovitsky, S. G. L’vov, and N. A. Sainov. VLS-growth of carbon nanotubes from the vapor. *Chemical Physics Letters*, 317:65–70, 2000. 62, 63
- [128] L. T. Chadderton and Y. Chen. A model for the growth of bamboo and skeletal nanotubes: catalytic capillarity. *Journal of Crystal Growth*, 240:164–169, 2002. 62
- [129] K. K. Nanda, S. N. Sahu, and S. N. Behera. Liquid-drop model for the size-dependent melting of low-dimensional systems. *Physical Review A*, 66:13208, 2002. 62
- [130] F. Ding, A. Rosén, S. Curtarolo, and K. Bolton. Modeling the melting of supported clusters. *Applied Physics Letters*, 88:133110, 2006. 62
- [131] T. Bachelis, H.J. Güntherodt, and R. Schäfer. Melting of isolated tin nanoparticles. *Physical Review Letters*, 85:1250–1253, 2000. 62

Bibliography

- [132] R. R. Vanfleet and J. M. Mochel. Thermodynamics of melting and freezing in small particles. *Surface Science*, 341:40–50, 1995. 62
- [133] K. Bartsch and A. Leonhardt. An approach to the structural diversity of aligned grown multi-walled carbon nanotubes on catalyst layers. *Carbon*, 42:1731–1736, 2004. 63, 64
- [134] E. F. Kukovitsky, S. G. L’vov, N. A. Sainov, V. A. Shustov, and L. A. Chernozatonskii. Correlation between metal catalyst particle size and carbon nanotube growth. *Chemical Physics Letters*, 355:497–503, 2002. 63
- [135] K. Bartsch, K. Biedermann, T. Gemming, and A. Leonhardt. On the diffusion-controlled growth of multiwalled carbon nanotubes. *Journal of Applied Physics*, 97:114301, 2005. 63
- [136] T. I. Kamins, X. Li, R. S. Williams, and X. Liu. Growth and structure of chemically vapor deposited Ge nanowires on Si substrates. *Nano Letters*, 4:503–506, 2004. 68
- [137] P. Yang, H. Yan, S. Mao, R. Russo, J. Johnson, R. Saykally, N. Morris, J. Pham, R. He, and H. J. Choi. Controlled growth of ZnO nanowires and their optical properties. *Advanced Functional Materials*, 12:323–331, 2002. 68
- [138] J. Westwater, D. P. Gosain, S. Tomiya, S. Usui, and H. Ruda. Growth of silicon nanowires via gold/silane vapor–liquid–solid reaction. *Journal of Vacuum Science & Technology B: Microelectronics and Nanometer Structures*, 15:554, 1997. 68
- [139] G. H. Jeong, S. Suzuki, Y. Kobayashi, A. Yamazaki, H. Yoshimura, and Y. Homma. Effect of nanoparticle density on narrow diameter distribution of carbon nanotubes and particle evolution during chemical vapor deposition growth. *Journal of Applied Physics*, 98:124311, 2005. 67, 68
- [140] L. M. Liz-Marzán. Nanometals formation and color. *Materials Today*, 7:26–31, 2004. 67
- [141] J. J. Mock, M. Barbic, D. R. Smith, D. A. Schultz, and S. Schultz. Shape effects in plasmon resonance of individual colloidal silver nanoparticles. *Journal of Chemical Physics*, 116:6755–6759, 2002. 69
- [142] R. García and R. Pérez. Dynamic atomic force microscopy methods. *Surface Science Reports*, 47:197–301, 2002. 77, 81, 86, 91
- [143] C. Argento and R. H. French. Parametric tip model and force–distance relation for Hamaker constant determination from atomic force microscopy. *Journal of Applied Physics*, 80:6081, 1996. 80

- [144] J. N. Israelachvili. *Intermolecular & Surface Forces*. Academic Press, 2nd edition, 1991. 80, 90
- [145] F. London. The general theory of molecular forces. *Transactions of the Faraday Society*, 33:8–26, 1937. 80
- [146] H. C. Hamaker. The London–van der Waals attraction between spherical particles. *Physica*, 4:1058–1072, 1937. 80
- [147] P. D. Ritger and N. J. Rose. *Differential Equations with Applications*. Courier Dover Publications, 2000. 82
- [148] T. Stifter, O. Marti, and B. Bhushan. Theoretical investigation of the distance dependence of capillary and van der Waals forces in scanning force microscopy. *Physical Review B*, 62:13667–13673, 2000. 89, 90
- [149] L. Zitzler, S. Herminghaus, and F. Mugele. Capillary forces in tapping mode atomic force microscopy. *Physical Review B*, 66:155436, 2002. 90
- [150] Y. Ebenstein, E. Nahum, and U. Banin. Tapping mode atomic force microscopy for nanoparticle sizing: tip–sample interaction effects. *Nano Letters*, 2:945–950, 2002. 91, 92
- [151] Á. Mechler, J. Kopniczky, J. Kokavecz, A. Hoel, C.G. Granqvist, and P. Heszler. Anomalies in nanostructure size measurements by AFM. *Physical Review B*, 72:125407, 2005. 91, 92
- [152] L. Chen, X. Yu, and D. Wang. Cantilever dynamics and quality factor control in AC mode AFM height measurements. *Ultramicroscopy*, 107:275–280, 2007. 93
- [153] R. M. Taylor, W. Robinett, V. L. Chi, F. P. Brooks Jr, W. V. Wright, R. S. Williams, and E .J. Snyder. *The nanomanipulator: a virtual-reality interface to a scanning tunneling microscope*. PhD thesis, The University of North Carolina at Chapel Hill, 1994. 95, 96
- [154] M. Finch, V. L. Chi, R. M. Taylor II, M. Falvo, S. Washburn, and R. Superfine. Surface modification tools in a virtual environment interface to a scanning probe microscope. In *Proceedings of the 1995 symposium on Interactive 3D graphics*, 1995. 95, 96
- [155] G. Li, N. Xi, M. Yu, and W. K. Fung. Development of augmented reality system for AFM-based nanomanipulation. *Mechatronics, IEEE/ASME Transactions on*, 9:358–365, 2004. 95
- [156] S. Grange, F. Conti, P. Helmer, P. Rouiller, and C. Baur. Delta Haptic Device as a nanomanipulator. *Proceedings of SPIE*, 4568:100, 2003. 97

Bibliography

- [157] M. Jobin, R. Foschia, S. Grange, C. Baur, G. Gremaud, Kyumin Lee, L. Forró, and A. J. Kulik. Versatile force-feedback manipulator for nanotechnology applications. *Review of Scientific Instruments*, 76:053701, 2005. 97, 99
- [158] F. J. Rubio-Sierra, R. W. Stark, S. Thalhammer, and W. M. Heckl. Force-feedback joystick as a low-cost haptic interface for an atomic-force-microscopy nanomanipulator. *Applied Physics A: Materials Science & Processing*, 76:903–906, 2003. 97
- [159] M. R. Falvo, G. J. Clary, R. M. Taylor II, V. Chi, F. P. Brooks Jr, S. Washburn, and R. Superfine. Bending and buckling of carbon nanotubes under large strain. *Nature*, 389:582, 1997. 99
- [160] M. Guthold, M. R. Falvo, W. G. Matthews, S. Paulson, S. Washburn, D. Erie, R. Superfine, F. P. Brooks, and R. M. Taylor II. Controlled manipulation of molecular samples with the nanoManipulator. *IEEE/ASME Transactions on Mechatronics*, 5:189–198, 2000. 99
- [161] M. R. Falvo, J. Steele, R. M. Taylor, and R. Superfine. Gearlike rolling motion mediated by commensurate contact: carbon nanotubes on HOPG. *Physical Review B*, 62:10665–10667, 2000. 99
- [162] C. Ritter, M. Heyde, U. D. Schwarz, and K. Rademann. Controlled translational manipulation of small latex spheres by dynamic force microscopy. *Langmuir*, 18:7798–7803, 2002. 99, 100
- [163] C. Ritter, M. Heyde, B. Stegemann, K. Rademann, and U. D. Schwarz. Contact-area dependence of frictional forces: moving adsorbed antimony nanoparticles. *Physical Review B*, 71:85405, 2005. 99, 100
- [164] B. Anczykowski, B. Gotsmann, H. Fuchs, J. P. Cleveland, and V. B. Elings. How to measure energy dissipation in dynamic mode atomic force microscopy. *Applied Surface Science*, 140:376–382, 1999. 99

Acknowledgments

The last four and half years in Switzerland have been pivotal in my growth as a physicist and a person. And I have so many people to thank for it. First of all, I thank my wife Jisun Park, without the support and the motivation of whom this thesis would have been impossible. I thank our families for their love and support. I especially thank Jisun's parents for financial support and the periodic shipments of Korean foodstuff.

I thank my professor, László Forró, for his leadership and patience. I also thank his wife, Livia Horváth, for the wonderful Christmas parties.

I'm indebted to my manager, Andrzej J. Kulik, for his trust, wisdom and generosity. I'm also grateful to his wife, Gerit Kulik, for the countless dinner invitations.

I thank Monique Bettinger, the secretary of IPMC, for her kindness and support.

I thank the old and new members of the NN Group for their friendship, help, and scientific inspiration: Ana Akrap, Barbara Korbély, Neven Barisic, Elena Bertseva, Markus Bonda, Luka Ćirić, Christel Dieker, Martial Duchamp, Titusz Feher, Raphael Föschia, Richard Gaal, Thomas Geiges, Camilo Guzmán, Daniel Gutierrez, Stefan Hensberger, Sylvia Jeney, Marc Jobin, Yankı Keleş, Andras Kis, Gerit Kulik, Anna Kusmartseva, Branimir Lukić, Arnaud Magrez, Pierre Marcoux, Zlatko Mickovic, Csilla Mikó, Mirko Milas, Marijana Mionic, Bálint Náfrádi, Katarzyna Pierzchala, Jin Won Seo, Andrzej Sienkiewicz, Balász Sipos, and Bertrand Vilenó. I also thank the regular visitors Malgorzata Lekka and Janusz Lekki.

I must acknowledge Arnaud Magrez for our fruitful discussions on the synthesis and characterization of nanostructures. I hope that he succeeds in growing perfect multiwall carbon nanotubes by CVD one day (really!). Also, I must mention that many electron microscopy images appearing in this thesis are the works of Martial Duchamp and Christel Dieker.

The support from the IPMC technicians, especially Gérald Beney, Guillaume Camarda, and Alessandro Ichino, have been invaluable in realizing this thesis, and I thank them for their enthusiasm.

I thank the *lunch crew* (old and new members): Duncan Alexander, Katharina Buss, Emiliano Campitelli, Thomas Geiges, Camilo Guzmán, John Hennig, Claudia Ionascu, Patrick Mayor, Alessandro Sellerio, Iva Tkalec, Lyubomira Veleva, and Jian Yang. Our conversations over lunch and coffee offered daily entertainment and were often sources of inspiration.

Numerous collaborators must also be mentioned: Prof. Juergen Brügger of IMT and

Acknowledgments

Ravi Shankar Sundaram (ink-jet deposition work in Chapter 3), Prof. G. Andrew D. Briggs of Oxford University (discussions on how to model a CVD-grown nanotube, Chapter 4), Philippe Pittet and Boris Hinz of LCB (cell-cell adhesion experiments), Jeroen Steen of IMT (tungsten cantilevers), Dr. Peter J. Cumpson of the British National Physics Laboratory (cantilever calibration device), and Daniela Silvano of ISIC (plasma cleaning). I acknowledge the people at Park Systems for their punctual and generous technical support: Dr. Sang-il Park, Yong Seok Kim, Sang-min Lee, Bongwoo Kang, and In-Sung Choi.

I'm grateful to the National Center of Competence in Research (NCCR) "Nanoscale Science" of the Swiss National Science Foundation for funding my research.

I thank the members of the jury: Prof. Georges Meylan of IPEP, Prof. Harald Brune of IPN, Prof. Ernst Meyer of University of Basel, and Prof. Othmar Marti of Ulm University.

Finally, I thank the friends outside work who made Switzerland a warmer and happier place for Jisun and me: Patrice and Jill Jatton, Jeong-Eung Park, Sung-jin Kim, Sanghoon Chin, Hanne Frenkel, and Florence Mayor.

Curriculum Vitae

Kyumin Lee

Born on the 27th of October, 1976
Seoul, South Korea

Education

- 1990–1994** Jakarta International School, Indonesia
High school diploma and full International Baccalaureate (IB) diploma
- 1995–1999** Seoul National University, South Korea
Bachelor of Science in physics
- 2003–2008** Ecole Polytechnique Fédérale de Lausanne, Switzerland
Ph.D. in physics

Work Experience

- 1999–2003** Park Systems (formerly PSIA), Suwon, South Korea
Electrical engineer and team leader
- 2003–2008** Ecole Polytechnique Fédérale de Lausanne, Switzerland
Research assistant
- 2008–** Synova SA, Ecublens, Switzerland
R&D engineer

Teaching

- 2004–2005** Assistant for the course “Travaux pratiques de physiques (destiné aux étudiants en sciences et technologies du vivant)” (2 consecutive years). **Award for Teaching Excellence** with the work in summer, 2005
- 2004** Assistant for the course “Introduction à la métrologie”
- 2005–2007** Assistant for the course “Travaux pratique de physique 2ème année” (2 consecutive years)

Peer-Reviewed Publications

1. **Kyumin Lee**, M. Duchamp, G. Kulik, A. Magrez, Jin Won Seo, S. Jeney, A. J. Kulik, L. Forro, R. S. Sundaram, and J. Brugger. Uniformly dispersed deposition of colloidal nanoparticles and nanowires by boiling. *Applied Physics Letters*, 91:173112, 2007. DOI: 10.1063/1.2803320
2. **Kyumin Lee**, B. Lukic, A. Magrez, J. W. Seo, G. A. D. Briggs, A. J. Kulik, and L. Forro. Diameter-dependent elastic modulus supports the metastable-catalyst growth of carbon nanotubes. *Nano Letters*, 7:1598–1602, 2007. DOI: 10.1021/nl070502b
3. P. Pittet, **Kyumin Lee**, A. J. Kulik, J.-J. Meister, and Boris Hinz. Fibrogenic fibroblasts increase intercellular adhesion strength by reinforcing individual OB-cadherin bonds. *Journal of Cell Science*, 121:877–886, 2008. DOI: 10.1242/jcs.024877
4. Y. Zhiyong, E. Mielczarski, J. Mielczarski, D. Laub, P. Buffat, U. Klehm, P. Albers, **Kyumin Lee**, A. Kulik, L. Kiwi-Minsker, A. Renken, and J. Kiwi. Preparation, stabilization and characterization of TiO₂ on thin polyethylene films(LDPE). *Water Research*, 41:862–874, 2007. DOI: 10.1016/j.watres.2006.11.020
5. J. A. J. Steen, J. Hayakawa, T. Harada, **Kyumin Lee**, F. Calame, G. Boero, A. J. Kulik, and J. Brugger. Electrically conducting probes with full tungsten cantilever and tip for scanning probe applications. *Nanotechnology*, 17:1464–1469, 2006. DOI: 10.1088/0957-4484/17/5/050
6. B. Lukic, J. W. Seo, E. Couteau, **Kyumin Lee**, S. Gradecak, B. Berkecz, R. Hernadi, S. Delpeux, T. Cacciaguerra, F. Beguin, A. Fonseca, J. B. Nagy, G. Csanyi, A. Kis, A. J. Kulik, and L. Forro. Elastic modulus of multi-walled carbon nanotubes produced by catalytic chemical vapour deposition. *Applied Physics A*, 80:695–700, 2005. DOI: 10.1007/s00339-004-3100-5
7. M. Jobin, R. Foschia, S. Grange, C. Baur, G. Gremaud, **Kyumin Lee**, L. Forro, and A. J. Kulik. Versatile force-feedback manipulator for nanotechnology applications. *Review of Scientific Instruments*, 76:053701, 2005. DOI: 10.1063/1.1891346
8. Joonhyung Kwon, Jaewan Hong, Yong-Seok Kim, Dong-Youn Lee, **Kyumin Lee**, Sang-min Lee, and Sang-il Park. Atomic force microscope with improved scan accuracy, scan speed, and optical vision. *Review of Scientific Instruments*, 74:4378–4383, 2003. DOI: 10.1063/1.1610782

Review Articles and Book Chapters

1. J. W. Seo, A. Magrez, M. Milas, **Kyumin Lee**, V. Lukovac, and L. Forro. Catalytically grown carbon nanotubes: from synthesis to toxicity. *Journal of Physics D: Applied Physics*, 40:R109–R120, 2007. DOI: 10.1088/0022-3727/40/6/R01
2. A. J. Kulik, A. Kis, B. Lukic, **Kyumin Lee**, and L. Forro. Mechanical properties of carbon nanotubes. In E. Gnecco and E. Meyer, editors, *Fundamentals of Friction and Wear on the Nanoscale*, pages 583–600. Springer, 2007. ISBN 978-3-540-36806-9

Oral Presentations

1. Uniformly dispersed deposition of colloidal nanoparticles and nanowires by boiling. 6th ESF Nanotribology Workshop, May 2007. Santa Margherita di Pula, Sardinia, Italy.
2. Using atomic force microscope to study friction at the nanometer scale. Nanozoom conference, Micronora Trade Fair, September 2006. Besançon, France.
3. Diameter dependence of the bending modulus of CCVD-grown multi-walled carbon nanotubes. International Conference on Nanoscience and Technology (ICN+T), August 2006. Basel, Switzerland.

Miscellaneous Research Projects

1. Nanoscale characterization and lithography using atomic force microscopy. Project at Park Systems, funded by the Ministry of Science and Technology (MOST) of Korea, 2001–2005. Topics: accurate and precise quantitative CD measurements, contact-hole patterns, STI patterns, and phase-shift patterns on photomask; automated nanoscale lithography using CAD design files.
2. Application of atomic force microscopy in semiconductor fabrication process. Project at Park Systems, funded by the Ministry of Commerce, Industry and Energy of Korea, 1998–2001. Topics: automated AFM systems for 200mm and 300mm wafers; blank wafer defect review; BPSG reflow angle measurements; flatness measurements.
3. Segregation phenomena in a granular heap. Bachelor of Science thesis project at Prof. Insuk Yu’s lab in Seoul National University. Poster presentation at Korean Physical Society fall meeting in 1998.